SSCL-590

SSCL-590

Superconducting Super Collider Laboratory

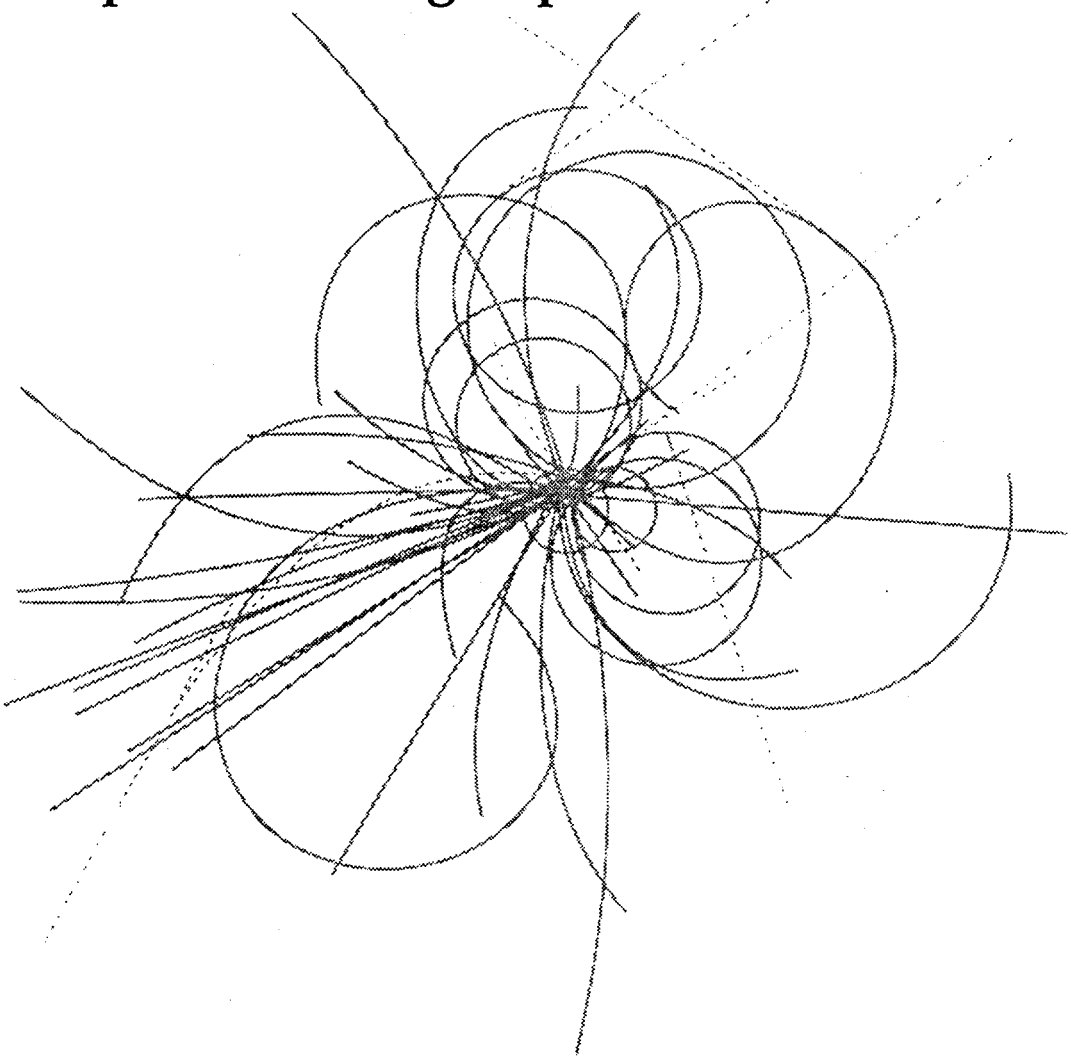

Beam-Beam Interaction Effects on Particle Dynamics

J. Koga

August 1992

SSCL-590

Beam-Beam Interaction Effects on Particle Dynamics*

J. Koga

Superconducting Super Collider Laboratory
2550 Beckleymeade Avenue
Dallas, TX 75237

August 1992

* Presented to the Faculty of the Graduate School of The University of Texas at Austin in partial fulfillment of the requirements for the degree of Doctor of Philosophy. Research supported in part by the Superconducting Super Collider Laboratory, which is operated by the Universities Research Association, Inc., for the U.S. Department of Energy under Contract No. DE-AC35-89ER40486.

SSCL-590

Beam-Beam Interaction Effects on Particle Dynamics

J. Koga

Abstract

The effects of the beam-beam interaction on particle dynamics in a synchrotron collider are investigated. The main highlight of this work is the investigation of collective effects of the beam-beam interaction in a self-consistent approach that naturally incorporates the correct single-particle dynamics. The most important target of this simulation is to understand and predict the long-time (10^8–10^9 rotations) behavior of the beam luminosity and lifetime.

For this task a series of computer codes in one spatial dimension has been developed in increasing order of sophistication. They are: the single-particle dynamics tracking code, the strong-strong particle-in-cell (PIC) code, and the particle code based on the δf algorithm. The latter two include the single-particle dynamics of the first. The third approach is used to understand beam lifetime by trying to improve the numerical noise problem in the second.

Scans in tune ν_0 and tune shift $\Delta\nu_0$ show regions of stability and instability that correspond to the regions predicted by a linear theory. Strong resonance beam blowup is observed just above $\nu_0 = 1/2$ and $\nu_0 = 1/4$, where the rate of beam blowup drops with the order of the resonance.

In both the strong-strong code and δf code using the reference parameters of the Superconducting Super Collider, oscillations in the tune shift, $\Delta\nu$, are observed. The odd moments of the beam are increasing in oscillation amplitude with rotation number, while the amplitudes of the even moments either decrease or remain constant. The

"flip-flop" effect is observed in the strong-strong code simulations and is found to be sensitive to the initial conditions.

In studying slow particle diffusion in the phase space of the beams away from resonances, the tracking code shows no diffusion of particles from the beam-beam interaction after 10^5 rotations. The δf code shows all particles diffusive after 10^5 rotations. The diffusion coefficient is an exponential function of the action. An attempt to understand the diffusion process based on the spontaneously generated beam offset model has brought an agreement between analytic theory and the tracking code with random beam offsets. The exponential behavior found in the self-consistent δf code, however, remains unexplained, although the order of magnitude as well as the behavior at large tune shift are in agreement with the theoretical model. A possible cause of this discrepancy might be the presence of KAM surfaces in low tune shift regimes.

CONTENTS

FIGURES vii
TABLES xii
1.0 INTRODUCTION 1
2.0 BASIC ACCELERATOR PHYSICS 3
2.1 Transverse Particle Motion 4
2.2 Transverse Focussing 5
3.0 THE BEAM-BEAM INTERACTION 7
3.1 Dynamic Beta 10
3.2 Steady State Distribution 13
3.3 Dynamics About the Steady State 14
3.4 Vlasov Approach 17
3.5 Diffusion from Beam Offset 19
4.0 FILAMENTATION INSTABILITY 20
5.0 PREVIOUS BEAM-BEAM SIMULATION RESULTS 21
6.0 SIMULATION MODELS 25
6.1 Tracking Code 26
6.2 Vlasov Code 27
6.2.1 Boundary Conditions 30
6.2.2 Square Geometry 31
6.3 Particle-in-Cell Codes 33
6.3.1 Accelerator Model 34
6.3.2 Electromagnetic Code 34
6.3.3 Strong-Strong Code 35
6.3.4 Noisy Model 45
6.4 δf Algorithm 45
6.4.1 Finite Particle Representation 48
6.4.2 Symplectic Mapping 50
6.4.3 Time Advance 52
6.5 Diagnostic Quantities 53
6.5.1 Emittance 53
6.5.2 Tune Shift 54
6.5.3 Determination of Beam Moments 56
6.5.4 Determination of Diffusion 57
7.0 SIMULATION RESULTS 58
7.1 Filamentation Instability 59
7.1.1 Electromagnetic Code Results 59
7.1.2 Vlasov Code Results 61
7.2 Collective Beam-Beam Effects 64
7.2.1 Reference Parameters 64
7.2.2 $\nu_0 - \Delta\nu_0$ Stability 87

7.3 Particle Diffusion 92
7.3.1 Tracking Code Results 92
7.3.2 Strong-Strong Simulation Results 96
7.3.3 δf Simulation Results 102
7.3.4 Beam Offset Effects 111
8.0 CONCLUSIONS 119
8.1 Summary of Results 120
8.1.1 Filamentation Instability 120
8.1.2 Collective Beam-Beam Effects 120
8.1.3 Stability in the Tune Versus Tune Shift Space 121
8.1.4 Particle Diffusion 122
8.1.5 Beam Offset Effects 123
8.2 Future Improvements 124
ACKNOWLEDGEMENTS 127
REFERENCES 129

FIGURES

2.1 Modern Accelerator Configuration. 3
2.2 Fields of a Quadrupole Magnet. 6
3.1 Geometry of the Beam-Beam Interaction for a Test Charge. 7
3.2 Stability of a Uniform Cylindrical Beam to Beam-Beam Perturbations, Where ξ is Plotted Versus ν_0. 12
3.3 Stability Diagrams for the Case of Two Bunches per Beam and Maximum Modes of $m = 2, 4, 6$, and 8. 19
5.1 Simulation of the Vertical Beam Profile. The histogram is the result of binning each test particle over 1000 turns. The solid curve is the original Gaussian profile of the beam. 24
5.2 Poincare Map of a Test Particle, Where $\nu_x = 25.2$ and $\nu_y = 23.32$ After 10,348 Turns. 25
6.1 Communication Path for North, South, East, and West Communication in the Square Geometry. 31
6.2 The Two Components Used to Model the Collider. 34
6.3 A Gaussian Distribution of Particles Produced from a Random Number Generator. 40
6.4 Distribution Integrated over p_x with Random Number-Generated Phase Space Positions. 41
6.5 Uniform Distribution of 10,000 Particles in x, p_x Phase Space. 42
6.6 Distribution Integrated over p_x with Uniform Distribution and Nonuniform Charge Assignment. 43
6.7 A Nonuniform Distribution of 10,000 Particles with Equal Charge. 44
6.8 The Profile in x of a Nonuniform Distribution of Particles. 44
6.9 Uniform Distribution of 1000 Particles in x, p_x Phase Space. 50
7.1 (x, p_x) Phase Space Plots for $\omega_b T = 50, 100$, and 150 at the Top, Middle, and Bottom of the Figure, Respectively, with $\gamma = 100$. 59
7.2 Growth Rate of Filamentation Instability Γ_{max}/ω_n, Where $\omega_n = \omega_b/\gamma^{1/2}$, for Three Values of γ. 60
7.3 Maximum Growth Rate Γ_{max}/ω_n With and Without the Electrostatic Field Calculation, Where $\omega_n = \omega_b/\gamma^{1/2}$, Versus the Ratio of Beam Radius ω_b to Collisionless Skin Depth $\lambda_n = c\gamma^{1/2}/\omega_b$. 60
7.4 Comparison Between the Intel Hypercube, the Connection Machine, and the Cray YMP on a Test Problem. The growth in field energy as a function of time $(\omega_{pe}t)$ is shown. 61
7.5 Integrated Distribution Function $f(x, z)$ at 0 and 400 Time Steps from the Top to the Bottom. 62
7.6 Integrated Distribution Function $f(z, p_z)$ at 0 and 400 Time Steps from the Top to the Bottom. 63
7.7 Tune Shift of Interacting Beams. 66
7.8 Initial (Top) and After 1000 Rotations (Bottom) $(x/\sigma_x, p_x/\sigma_p)$ Phase Space Particle Positions. 66
7.9 Distribution of 10^4 Simulation Particles in $(x/\sigma_x, p_x/\sigma_p)$ Space After 10,240 Rotations, with $\nu_0 = 0.285$ and $\Delta\nu_0 = 2.1 \times 10^{-3}$. 68

7.10 Distribution of 10^4 Simulation Particles in x After 10,240 Rotations, with $\nu_0 = 0.285$ and $\Delta\nu_0 = 2.1 \times 10^{-3}$. 68
7.11 Tune Shift $\Delta\nu$ from a Least-Squares-Fit to Small-Amplitude Particles $x < 0.1\sigma_x$ (Top) and All Particles (Bottom) for $M = 10,240$ Rotations. 69
7.12 Position of an Initially Small-Amplitude Particle $x_0 = 0.1\sigma_x$ in $(x/\sigma_x, p_x/\sigma_p)$ Space for $M = 10,240$ Rotations (Top) and Power Spectrum of x Position of the Particle Versus ν (Bottom). 71
7.13 Position of an Initially Large-Amplitude Particle $x_0 = 0.9\sigma_x$ in $(x/\sigma_x, p_x/\sigma_p)$ Space for $M = 10,240$ Rotations (Top) and Power Spectrum of x Position of the Particle Versus ν (Bottom). 71
7.14 Beam Moments $< x >$ and $< (x- < x >)^3 >$ for $M = 10,240$ Rotations at the Top and Bottom of the Figure, Respectively. 72
7.15 Beam Moments $< (x- < x >)^2 >$ and $< (x- < x >)^4 >$ for $M = 10,240$ Rotations at the Top and Bottom of the Figure, Respectively. 72
7.16 Beam Moment $< x >$ and Power Spectrum $S(\nu)$ for $M = 10,240$ Rotations at the Top and Bottom of the Figure, Respectively. 73
7.17 Beam Moment $< (x- < x >)^2 >$ and Power Spectrum $S(\nu)$ for $M = 10,240$ Rotations at the Top and Bottom of the Figure, Respectively. 73
7.18 The Emittance ϵ of Both Beams for 10,240 Rotations. One beam is at the top and the other beam is at the bottom of the figure. 75
7.19 The Emittance ϵ of Both Beams for 10,240 Rotations with a Slightly Different Initialization. One beam is at the top and the other beam is at the bottom of the figure. 75
7.20 Distribution of 10^4 Simulation Particles in $(x/\sigma_x, p_x/\sigma_p)$ Space After 10,240 Rotations with $\nu_0 = 0.285$ and $\Delta\nu_0 = 2.1 \times 10^{-3}$. 76
7.21 Distribution of 10^4 Simulation Particles in x After 10,240 Rotations with $\nu_0 = 0.285$ and $\Delta\nu_0 = 2.1 \times 10^{-3}$. 76
7.22 Tune Shift $\Delta\nu$ Measured from a Least-Squares-Fit to Small-Amplitude Particles $x < 0.1\sigma_x$ for $M = 10,240$ Rotations. 77
7.23 The Emittance ϵ of Both Beams for 10,240 Rotations. One beam is at the top and the other beam is at the bottom of the figure. 77
7.24 The Minimum and Maximum Perturbation Values $\delta f/f_0$ for $M = 10,240$ Rotations, $\nu_0 = 0.285$, and $\Delta\nu_0 = 2.1 \times 10^{-3}$. 79
7.25 Distribution of 10^3 Simulation Particles in $(x/\sigma_x, p_x/\sigma_p)$ Space After 10^5 Rotations with $\nu_0 = 0.285$ and $\Delta\nu_0 = 2.1 \times 10^{-3}$. 79
7.26 Gaussian Steady-State Distribution. 80
7.27 Distribution of 10^3 δf Simulation Particles Including the Particle Weights in x After 10^5 Rotations with $\nu_0 = 0.285$ and $\Delta\nu_0 = 2.1 \times 10^{-3}$. 80
7.28 Tune Shift $\Delta\nu$ Measured from a Least-Squares-Fit to Small-Amplitude Particles $x < 0.1\sigma_x$ (Top) and All Particles (Bottom) for $M = 10,240$ Rotations. 83
7.29 The Tune Shift $\Delta\nu$ Measured from the Shift in the Power Spectral Peaks of the x Positions of 100 Sample Particles After $M = 10^5$ Rotations. 83
7.30 Beam Moment $< x >$ and $S(\nu)$ for $M = 10^5$ Rotations at the Top and Bottom of the Figure, Respectively. 84

7.31 Beam Moment $< (x- < x >)^2 >$ and $S(\nu)$ for $M = 10^5$ Rotations at the Top and Bottom of the Figure, Respectively. 84
7.32 Beam Moment $< (x- < x >)^3 >$ and $S(\nu)$ for $M = 10^5$ Rotations at the Top and Bottom of the Figure, Respectively. 85
7.33 Beam Moment $< (x- < x >)^4 >$ and $S(\nu)$ for $M = 10^5$ Rotations at the Top and Bottom of the Figure, Respectively. 85
7.34 Odd Modes $m = 1, 3, 5$ Down the Figure of the Distribution of Particles for $M = 10^5$ Rotations. 86
7.35 Even Modes $m = 2, 4, 6$ Down the Figure of the Distribution of Particles for $M = 10^5$ Rotations. 86
7.36 The Emittance ϵ of Both Beams for 10^5 Rotations. One beam is at the top and the other beam is at the bottom of the figure. 87
7.37 $\nu_0 - \Delta\nu_0$ Stability Diagram. 88
7.38 $(x/\beta^*, x')$ Distribution of Particles for $\nu_0 = 1/2 + \Delta\nu_0$ (Top) and $\nu_0 = 1/2 - \Delta\nu_0$ (Bottom), Where $\Delta\nu_0 = 2.1 \times 10^{-3}$. 89
7.39 $(x/\beta^*, x')$ Distribution of Particles for $\nu_0 = 1/4 + \Delta\nu_0$ (Top) and $\nu_0 = 1/4 - \Delta\nu_0$ (Bottom), Where $\Delta\nu_0 = 2.1 \times 10^{-3}$. 90
7.40 Emittance as a Function of Rotations for ν_0 Just Above 1/3. 91
7.41 $(x/\beta^*, x')$ Distribution of Particles for $\nu_0 = 1/3 + \Delta\nu_0$, Where $\Delta\nu_0 = 2.1 \times 10^{-3}$. 91
7.42 Initial Particle Positions for 100 Tracking Code Particles in $(x/\sigma_x, p_x/p)$ Phase Space. 92
7.43 Poincare Section in $(x/\sigma_x, p_x/\sigma_p)$ Space of Small- and Large-Amplitude Tracking Code Particles After $M = 10^5$ Rotations. 93
7.44 D_x from the Tracking Code with $\Delta\nu_0 = 2.1 \times 10^{-3}$ and $\nu = 0.285$ for $M = 10,240$ Rotations. df1 and df2 have time scales of $\Delta N_1 = 102$ and $\Delta N_2 = 1024$ rotations, respectively. 94
7.45 D_x from the Tracking Code with $\Delta\nu_0 = 2.1 \times 10^{-3}$ and $\nu = 0.285$ for $M = 40,960$ Rotations. df1 and df2 have time scales of $\Delta N_1 = 409$ and $\Delta N_2 = 4096$ rotations, respectively. 95
7.46 D_x from the Tracking Code of the Beam with $\Delta\nu_0 = 2.1 \times 10^{-3}$ and $\nu = 0.285$ for $M = 10^5$ Rotations. df1 and df2 have time scales of $\Delta N_1 = 1000$ and $\Delta N_2 = 10,000$ rotations, respectively. 95
7.47 D_x from the Strong-Strong Code with $\Delta\nu_0 = 2.1 \times 10^{-3}$ and $\nu = 0.285$ for $M = 10,240$ Rotations. df1 and df2 have time scales of $\Delta N_1 = 102$ and $\Delta N_2 = 1024$ rotations, respectively. 97
7.48 Poincare Section in $(x/\sigma_x, p_x/\sigma_p)$ Space of Small- and Large-Amplitude Strong-Strong Code Particles after $M = 10,240$ Rotations. 97
7.49 D_x Versus Particle Number for a Sample Particle at $r/\sigma = 0.1$ for $M = 1000$ Rotations. df1 and df2 have time scales of $\Delta N_1 = 10$ and $\Delta N_2 = 100$ rotations, respectively. 98
7.50 D_x Versus Particle Number for a Sample Particle at $r/\sigma = 0.9$ for $M = 1000$ Rotations. df1 and df2 have time scales of $\Delta N_1 = 10$ and $\Delta N_2 = 100$ rotations, respectively. 98
7.51 Initial Particle Positions for 100 Strong-Strong Sample Particles in $(x/\sigma_x, p_x/p)$ Phase Space. 100

7.52 Poincare Section in $(x/\sigma_x, p_x/\sigma_p)$ Space of Small- and Large-Amplitude Strong-Strong Code Particles with Uniform Charge After $M = 10,240$ Rotations. 100
7.53 D_x from the Strong-Strong Code with the Variable Charge and Uniform Charge Particle Initialization for $M = 10,240$ Rotations. df1 and df2 have time scales of $\Delta N_1 = 102$ and $\Delta N_2 = 1024$ rotations, respectively. 101
7.54 D_x from Tracking Code and the Strong-Strong Code with Uniform Charge Particle Initialization for $M = 10,240$ Rotations. df1 and df2 have time scales of $\Delta N_1 = 102$ and $\Delta N_2 = 1024$ rotations, respectively. 101
7.55 D_x from Noisy Tracking Code and PIC Code for $M = 10,240$ Rotations at $r/\sigma = 0.1$ and 0.9. df1 and df2 have time scales of $\Delta N_1 = 102$ and $\Delta N_2 = 1024$ rotations, respectively. 102
7.56 Poincare Section in $(x/\sigma_x, p_x/\sigma_p)$ Space of Small- and Large-Amplitude δf Code Particles After $M = 10,240$ Rotations. 103
7.57 Initial Distribution in (x, p_x) Phase Space of 100 Sample Particles. 103
7.58 D_x from the δf Code with 1000 Simulation Particles and the Tracking Code for $M = 10,240$ Rotations. df1 and df2 have time scales of $\Delta N_1 = 102$ and $\Delta N_2 = 1024$ rotations, respectively. 104
7.59 Variation of the Diffusion Coefficients with Particle Number N for $M = 10,240$ Rotations. 104
7.60 D_x from the δf Code with 1000 Simulation Particles for $M = 40,960$ Rotations. df1 and df2 have time scales of $\Delta N_1 = 409$ and $\Delta N_2 = 4096$ rotations, respectively. 106
7.61 Variation of the Diffusion Coefficients with Particle Number N for $M = 40,960$ Rotations. 106
7.62 D_x from Tracking Code and the δf Code for $M = 40,960$ Rotations. df1 and df2 have time scales of $\Delta N_1 = 409$ and $\Delta N_2 = 4096$ rotations, respectively. 107
7.63 D_x from Noisy Tracking Code for $M = 40,960$ Rotations. df1 and df2 have time scales of $\Delta N_1 = 409$ and $\Delta N_2 = 4096$ rotations, respectively. 107
7.64 D_x from the δf Code for $M = 10^5$ Rotations. df1 and df2 have time scales of $\Delta N_1 = 1000$ and $\Delta N_2 = 10,000$ rotations, respectively. 108
7.65 D_x from Tracking Code and the δf Code for $M = 10^5$ Rotations. df1 and df2 have time scales of $\Delta N_1 = 1000$ and $\Delta N_2 = 10,000$ rotations, respectively. 109
7.66 Variation of the Diffusion Coefficients with Particle Number N for $M = 10^5$ Rotations. 110
7.67 A $(x/\sigma_x, p_x/\sigma_p)$ Space Plot with Contour, Surface, and Grey-Scale Plots from the Top to the Bottom of the Figure. 110
7.68 $< x > /\sigma_x$ Versus M from δf Simulation, with $\nu_0 = 0.285$ and $\Delta\nu_0 = 0.0021$. 112
7.69 Total Change in the Action ΔJ_M Versus the Action J for Three Values of the Beam Offset ζ. 112
7.70 Tracking Code Results Showing the Change in $< (\Delta J_M)^2 > /2$ Per Turn Versus the Action J for Three Values of the Beam Offset ζ. The time scales over which df1 and df2 are calculated are 10^3 and 10^4 rotations, respectively. .. 113
7.71 Positions in $(x/\beta^*, x')$ Space of 100 Sample Particles. 113

7.72 δf Code Results Showing the Change in the Action ΔJ_M Per Turn Versus the Action J for Zero Initial Beam Offset. The time scales over which df1 and df2 are calculated are 10^3 and 10^4 rotations, respectively. 114
7.73 A Comparison of $k = 0$ with Terms $k = 1$ and $k = 2$. 115
7.74 A Comparison of Tracking Code with Input $< x >$ and Theory. 115
7.75 A Comparison of Tracking Code with Input $< x >$ and δf Results. 116
7.76 The Function Dependence of the Change in the Action with Argument J Rather Than $J/2$. 116
7.77 The Average Beam Offset $< x > /\Delta$ for Small, Medium, and Large r/σ Particles Down the Figure. 117
7.78 $< x >$ of the Beam with $\Delta\nu_0 = 8.4 \times 10^{-3}$. 118
7.79 D_x of the Beam with $\Delta\nu_0 = 2.1 \times 10^{-3}$ and $\Delta\nu_0 = 8.4 \times 10^{-3}$ for $M = 40,960$ Rotations. The time scales of df1 and df2 are 409 and 4096 rotations, respectively. 118
7.80 D_x from PIC and δf Codes of the Beam with $\Delta\nu_0 = 2.1 \times 10^{-3}$ for $M = 10,240$ Rotations. The time scales of df1 and df2 are 102 and 1024 rotations, respectively. 119

TABLES

3.1 Cases That Have Been Studied in Coherent Beam-Beam Dynamics in Increasing Complexity. 15
3.2 Beam Modes and Associated Resonances. 17
6.1 Steps for Advance of δf Algorithm. 52
7.1 SSC Parameters. 65

1.0 INTRODUCTION

The key goal of high-energy particle accelerators in addition to achieving high energies is achieving a high number of collision events from high-energy colliding beams. In circular accelerators or synchrotrons, this is accomplished by colliding two focussed beams that are travelling in opposite directions. The beams can be either of the same or opposite charge sign. The number of collision events depends on the interaction rate, R:[1]

$$R = L\sigma_{int}\,, \tag{1.1}$$

where L is the beam luminosity and σ_{int} is the interaction cross section of the particles in the beam. The luminosity of the colliding beams is defined as

$$L = f\frac{N^2}{4\pi\sigma^2}\,, \tag{1.2}$$

where N is the number of particles, σ is the rms beam size, and f is the frequency of collisions. To achieve a large interaction rate, it is necessary that the luminosity be as high as possible. High luminosity is achieved by high collision frequencies, a large number of particles per beam, and small beam sizes. However, higher N increases collective effects, higher f results in multi-bunch instabilities, and lower σ places more demands on focussing systems and beam sources. Typically the luminosity L is a number between 10^{30} and 10^{33} cm^{-2}sec^{-1} for contemporary high-energy accelerators. At high energies the interaction cross section σ_{int} tends to be small, on the order of 10^{-32} to 10^{-33} cm^2, as it is inversely proportional to the square of the beam energy. A large number of collisions is necessary to achieve a statistically significant amount of data. For example, in the Superconducting Super Collider (SSC) the projected storage time in the main ring is 24 hours. In this amount of time the bunched beams will undergo approximately 10^8 rotations and collisions. Therefore, the beams need to remain coherent for a long period of time. The major concern with circular colliders is long-term beam stability. Beam instabilities can lead to beam spreading, which reduces beam luminosity and beam lifetimes. Beam instability is caused by many factors:

- longitudinal and transverse momentum spread of the beam
- noise in the system
- magnetic field gradient errors
- resonances
- steering errors
- focussing errors
- beam-beam interaction.

One of the principal limitations on beam intensity is due to the beam-beam interaction via their collective electromagnetic fields.[2,3] For the hadron colliders the beam-beam interaction is expected to be even more crucial, since there is no synchrotron radiation damping to stop beam blow-up as in electron storage rings.[3]

In this paper we will concentrate on the beam-beam interaction with emphasis on the beam-beam kick and beam-beam plasma collective effects. In the beam-beam interaction, each beam imparts an impulse on the other beam at the interaction point where the beams cross. This impulse may be treated as a kick, as the interaction time is much shorter than the beam particle dislocation time due to collisions. The kick can include both the impulse acting on whole beams and impulses acting on individual particles within each beam. Beam-beam plasma collective effects include plasma instabilities or "soft" collisions. These instabilities modify the beam profile and can contribute to increasing beam size. Collective instabilities have the most effect in the interaction region, where the beam densities are highest in the accelerator. One of the fastest growing collective instabilities that can occur in a plasma is the filamentation instability. However, in typical high-energy heavy particle colliders the beam-beam interaction times are very short relative to the filamentation instability growth rate. In the SSC the interaction time is about 2% of the maximum growth rate time. The relative importance of collective effects in plasmas is determined from the plasma parameter g:

$$g = 1/(n\lambda_D^3)\,, \tag{1.3}$$

where n is the density and λ_D is the Debye length. If $g \ll 1$, collective effects play an important role. For SSC-type parameters, $g = 2.66$. So collective effects are not dominant for a single beam-beam interaction. However, the effects of a large number of successive interactions have yet to be determined.

The objective of this study is to determine beam-beam interaction effects on particle dynamics using a collective plasma model at the interaction point. A one-dimensional model is employed at the interaction point so that oscillations in only one transverse direction due to the counterstreaming beams are studied. The rest of the machine is treated by simple harmonic transport (betatron oscillations). By employing a fully self-consistent model at the interaction point, an assessment of the relative importance of collisions as a whole and individual "soft" collisions (collective effects) can be determined. Specifically, we will examine the contribution of self-consistent effects on beam blowup and particle diffusion after a large number of interactions.

2.0 BASIC ACCELERATOR PHYSICS

In this section we describe the basic equations and terminology of particle motion in modern circular accelerators or synchrotrons. The simplest configuration of a typical modern accelerator is shown in Figure 2.1. The basic components are:[4]

- a charged particle source
- main storage ring
- accelerating system
- interaction regions.

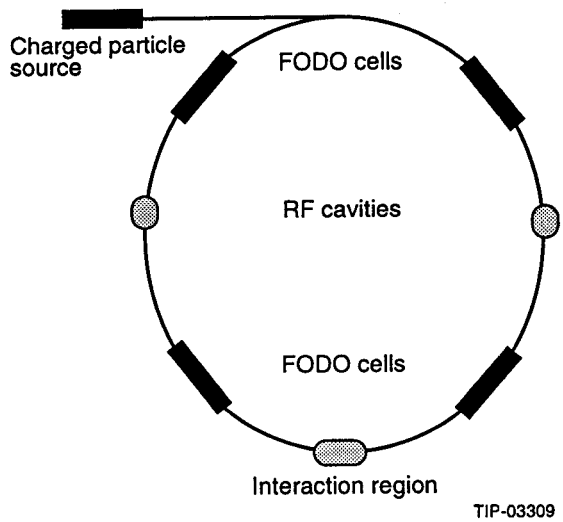

Figure 2.1. Modern Accelerator Configuration.

The charged particle source consists of a small volume of ionized hydrogen gas from which charged nuclei (protons) are accelerated. These charged particles are accelerated by an electric field before entering the main ring. A kicker makes these particles enter the main ring.

In the main ring the particles are confined by magnetic fields. The confinement system consists of two parts: (1) the steering magnets and (2) the FODO cells. The steering magnets are the dipole magnets that keep the particles bent in the plane perpendicular to the magnetic field so as to keep the beam within a nearly circular path. The FODO (focus-drift-defocus-drift) cells consist of a sequence of quadrupole magnets and drift regions (no magnets). The FODO cells cause net focussing of the beams and will be described in Section 2.2. Radio frequency (rf) cavities are used to accelerate the particles to high energies. The generated electromagnetic fields are resonant with the particles.

In the following sections we concentrate on the basic equations describing the motion of particles perpendicular to the accelerator path (transverse motion) and the net transverse focussing of particles. The longitudinal motion will be omitted from this basic discussion.

2.1 Transverse Particle Motion

An equation of motion for the transverse motion of particles travelling around a collider ring is obtained from the Lorentz force equation:

$$\frac{d\vec{p}}{dt} = q\vec{v} \times \vec{B}/c. \tag{2.1}$$

The following assumptions can be made:[1]

1. The design trajectory of the machine is a straight line or a single planar closed curve.
2. The field of the magnet is assumed to be two-dimensional. That is, the components of the magnetic field along the particle trajectory can be ignored.
3. Transverse velocities are assumed to be much smaller than longitudinal velocities. This is known as the "paraxial" approximation, with $v \approx v_s$, where v_s is the velocity of the particle along the particle trajectory and v is the total velocity. The "paraxial" approximation is used in most if not all particle acceleration designs.
4. The fields of the magnet are restricted to be linearly dependent on transverse displacement of the particles.
5. In a planar accelerator there is no radial component to the magnetic field.
6. Derivatives of transverse field components in the directions of the components are assumed to be zero, allowing one to neglect coupling between the two transverse motions.

The equation describing the transverse linear motion of particles travelling in the static magnetic field of the collider is, then, of the form:

$$x'' + K(s)x = 0\,, \tag{2.2}$$

where $x'' = d^2x/ds^2$, x is either direction perpendicular to the particle motion, s is the direction along the accelerator path, and $K(s)$ is similar to a spring constant in harmonic motion, which is a function of s. This equation is known as Hill's equation and was studied in the 19th century. In circular accelerators the function $K(s)$ is periodic—that is, $K(s + C) = K(s)$, where C is the circumference of the accelerator. A general solution to Eq. (2.2) can be obtained of the form:

$$x = A\beta^{1/2}(s)\cos[\Psi(s) + \delta]\,, \tag{2.3}$$

where $\Psi(s)$ is the phase advance of the particle as a function of distance along the collider s:

$$\Psi(s) = \int_0^s \frac{ds}{\beta(s)}\,. \tag{2.4}$$

$\beta(s)$ can be interpreted as the local wavelength of the oscillation divided by 2π, or the betatron oscillation length. A storage ring normally is designed and operated with $l < \beta$,

where l is the beam bunch length. The betatron oscillation length $\beta(s)$ and $K(s)$ are related through the differential equation:[1]

$$2\beta\beta'' - \beta'^2 + 4\beta^2 K = 4\,, \tag{2.5}$$

where $\beta' = d\beta/ds$ and $\beta'' = d^2\beta/ds^2$.

The phase advance of the particle per turn around the collider is called the "tune" ν and is defined as:

$$\nu = \frac{1}{2\pi}\oint \frac{ds}{\beta(s)}\,. \tag{2.6}$$

The tune ν can be thought of as the rotation in phase space due to betatron oscillations.

One can construct a transfer map from the entrance to the exit of the magnet section by writing the equations of motion in the form of a transfer matrix:[5]

$$\begin{pmatrix} x \\ x' \end{pmatrix}_{n+1} = \begin{pmatrix} \cos(2\pi\nu) + \alpha\sin(2\pi\nu) & \beta\sin(2\pi\nu) \\ -\frac{(1+(\alpha)^2)}{\beta}\sin(2\pi\nu) & \cos(2\pi\nu) - \alpha\sin(2\pi\nu) \end{pmatrix} \begin{pmatrix} x \\ x' \end{pmatrix}_n\,, \tag{2.7}$$

where $\alpha = -\beta'/2$ and $\beta' = d\beta/ds$, and the indices n and $n+1$ refer to the turn number. One can define another parameter:

$$\gamma = \frac{1+\alpha^2}{\beta}\,, \tag{2.8}$$

and then the transfer matrix can be written in the form:

$$M = I\cos(2\pi\nu) + J\sin(2\pi\nu)\,, \tag{2.9}$$

where

$$J = \begin{pmatrix} \alpha & \beta \\ -\gamma & -\alpha \end{pmatrix} \tag{2.10}$$

and I is the identity matrix. The quantities α, β, and γ are called the Courant-Synder parameters.[5]

2.2 Transverse Focussing

The existence of radial electric fields from the accelerating fields of the rf cavities, space charge forces between individual particles, and forces on the particles due to image charges in the vacuum chamber contribute to the transverse expansion of beam particles. Due to these effects, transverse focussing is necessary. Net focussing in the transverse plane is accomplished with quadrupole magnets. In quadrupole magnets the Lorentz force acts

to focus in one coordinate and to defocus in the other (Figure 2.2). The effect of the quadrupole magnet in the focussing direction can be represented by a matrix of the form:

$$\begin{pmatrix} x \\ x' \end{pmatrix}_{n+1} = \begin{pmatrix} 1 & 0 \\ -\frac{1}{f} & 1 \end{pmatrix} \begin{pmatrix} x \\ x' \end{pmatrix}_n , \tag{2.11}$$

where f is the focal length of the magnet. The paraxial and thin lens approximation has been made.[6] In the defocussing coordinate the focal length is of the opposite sign. A linear focussing design is possible using transfer matrices for the field-free drift regions and the magnetic impulse sections. A drift region is represented by a matrix of the form:

$$\begin{pmatrix} x \\ x' \end{pmatrix}_{n+1} = \begin{pmatrix} 1 & L \\ 0 & 1 \end{pmatrix} \begin{pmatrix} x \\ x' \end{pmatrix}_n , \tag{2.12}$$

where L is the length of the drift region. Net focussing is achieved by creating a lattice consisting of a focussing lens, a drift region, and a defocussing lens. The transfer matrix of this lattice is of the form:

$$M = \begin{pmatrix} 1 - \frac{L}{f} - (\frac{L}{f})^2 & 2L + \frac{L^2}{f} \\ -\frac{L}{f^2} & 1 + \frac{L}{f} \end{pmatrix} , \tag{2.13}$$

where stability is achieved when $L/2f$ is less than unity. Thus net focussing is achieved when the focal length f is greater than half the lens spacing L.

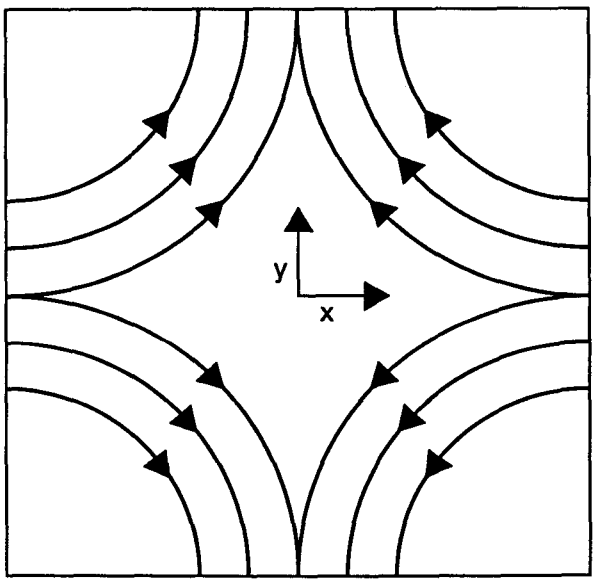

TIP-03310

Figure 2.2. Fields of a Quadrupole Magnet.

3.0 THE BEAM-BEAM INTERACTION

In this section we will review the basic concepts of the beam-beam interaction. The beam-beam interaction is an important factor in beam dynamics. It puts practical limits on the yield of the storage ring and prevents many existing storage rings from achieving design parameters.[7] Substantial use of the review article by Chao[8] is made in this section.

When two oppositely directed beams in a synchrotron meet at the interaction point of the collider, they give each other a kick. Consider an idealized collision event where cylindrical beams with radius a, length l, and N particles collide head-on. Figure 3.1 shows the geometry of the beam-beam interaction where a test particle at radius r of one beam is passing through the other beam. We neglect space charge forces, since the force

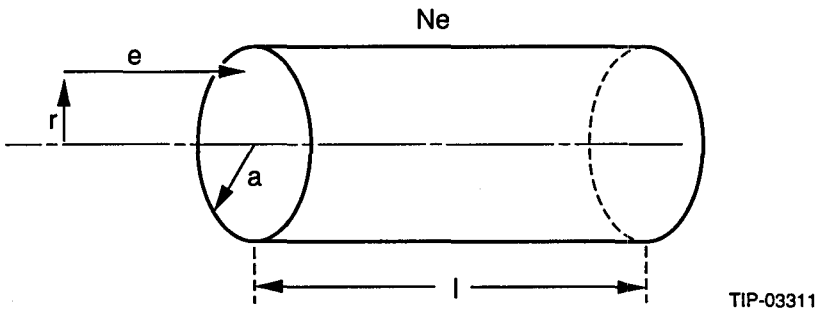

Figure 3.1. Geometry of the Beam-Beam Interaction for a Test Charge.

that a particle sees from an oncoming beam is $\approx 2\gamma^2$ times larger than the force from the other particles in the same beam, where γ is the relativistic factor. So for ultrarelativistic machines the space charge effect is relatively small. With a uniform cylinder of charge there is a radial electric field E_r of the form:

$$E_r = 2\frac{Ner}{a^2 l}, \tag{3.1}$$

where N is the number of particles in the beam, r is the distance from the center of the beam, a is the beam radius, and l is the length of the beam. In the relativistic limit $v \approx c$, where v is the beam velocity, the magnetic field B_θ produced by the beam is of the form:

$$B_\theta = E_r = 2\frac{Ner}{a^2 l}. \tag{3.2}$$

These combined fields produce a net force F_r on the test charge:

$$F_r = e(E_r + B_\theta) \tag{3.3}$$

$$= \frac{4Ne^2 r}{a^2 l}. \tag{3.4}$$

The impulse received by the test charge upon passing through the beam is

$$\Delta r' = \frac{F_r \Delta t}{\gamma m c} = \frac{2 N r_0}{\gamma a^2} r \,, \tag{3.5}$$

where $\Delta t = \frac{l}{2c}$ and $r_0 = \frac{e^2}{mc^2}$, the classical radius of the particle with mass m. Note that Eq. (3.5) is independent of the beam length l and can be rewritten in the form:

$$\Delta r' = -\frac{r}{f} \tag{3.6}$$

$$\frac{1}{f} = -\frac{2N}{\gamma a^2} r_0 \,. \tag{3.7}$$

The form of Eq. (3.6) makes the impulse look like a quadrupole error where f is the focal length. Keeping this in mind, one can define a beam strength parameter ξ due to the beam-beam interaction:

$$\xi = \frac{1}{4\pi} \frac{\beta^*}{f} \,, \tag{3.8}$$

where β^* is the betatron oscillation length at the beam-beam collision point. Using Eq. (3.7), the beam strength parameter can be written in the form:

$$\xi = \frac{N r_0 \beta^*}{2\pi \gamma a^2} \,. \tag{3.9}$$

Typically in proton-antiproton colliders, $\xi = 0.005$, and in an electron-positron collider, ξ is as large as 0.05.[9] The beam strength parameter ξ is related to the tune shift $\Delta\nu$, as we shall describe below. The tune shift $\Delta\nu$ indicates how much the tune ν is shifted by the beam-beam interaction.

In realistic cases the beams are not uniform cylinders of charge. In general the beam-beam force is nonlinear in x and y. Most often with large numbers of particles the beams are Bigaussian, where the widths in x and y direction are characterized by σ_x and σ_y. The kicks that particles get from such a beam may be expressed in the form:[8]

$$\Delta x' = -\frac{\partial U(x,y)}{\partial x} \tag{3.10}$$

$$\Delta y' = -\frac{\partial U(x,y)}{\partial y} \,, \tag{3.11}$$

where

$$U(x,y) = -\frac{N r_0}{\gamma} \int_0^\infty dt \frac{\exp\left[-\frac{x^2}{2(\sigma_x^2+t)} - \frac{y^2}{2(\sigma_y^2+t)}\right] - 1}{\sqrt{(\sigma_x^2+t)(\sigma_y^2+t)}} \,. \tag{3.12}$$

The equations representing the kicks are both nonlinear and are coupled. For small values of $y/\sigma_y \ll 1$ and $x/\sigma_x \ll 1$ the force is linear and the two motions are decoupled:

$$\Delta x' = \frac{x}{f_x} \tag{3.13}$$

$$\Delta y' = \frac{y}{f_y}, \tag{3.14}$$

where

$$\frac{1}{f_x} = \frac{2Nr_0}{\gamma\sigma_x(\sigma_x + \sigma_y)} \tag{3.15}$$

$$\frac{1}{f_y} = \frac{2Nr_0}{\gamma\sigma_y(\sigma_x + \sigma_y)}. \tag{3.16}$$

This holds for only a small number of particles in the beam. For values of $x/\sigma_x \approx 1$ and $y/\sigma_y \approx 1$, the forces are highly nonlinear. It is found that the optimum design occurs when $\xi_x = \xi_y$. Equivalently this can be expressed as

$$\frac{\beta_x^*}{f_x} = \frac{\beta_y^*}{f_y}, \tag{3.17}$$

where β_x^* and β_y^* refer to the betatron oscillation lengths in x and y, respectively, at the interaction point.

Two models are used to study the beam-beam interaction: the weak-strong and strong-strong models. Both models are important. For the weak-strong model the internal structure of the so-called strong beam is unperturbed. This type of model involves a rigid nonlinear lens at the interaction point (IP) and becomes a problem of a nonlinear map. Particles in the weak beam are perturbed by this map. For the strong-strong model both beams are perturbed.

The procedure in principle for solving the beam-beam problem is:

- Let the unperturbed distribution Ψ_0 be, for example, a Gaussian. With the strong-strong perturbation, Ψ_0 must be solved self-consistently. The perturbed beam steady-state distribution Ψ_0 is not Gaussian.
- Given the perturbed distribution Ψ_0, let

$$\Psi_1 = \Psi_0 + \Delta\Psi_1 \tag{3.18}$$

$$\Psi_2 = \Psi_0 + \Delta\Psi_2. \tag{3.19}$$

Are the infinitesimal perturbations $\Delta\Psi_{1,2}$ stable under mutual interactions?

Neither of these steps is easy. So far only bits and pieces have been done. Simple schemes have been developed to solve the beam-beam problem.

3.1 Dynamic Beta

A simple model that has been developed to study the stability of the beam to an idealized beam-beam perturbation is the dynamic beta model.[10] The main assumption of this model is that the beam-beam force is linear. So the model is valid for uniform cylindrical beams or for small values of x and y in nonuniform beams. The dynamic beta model is the simplest weak-strong or strong-strong model. The steady state distribution Ψ_0 is still Gaussian after the perturbation. Except that the tune, ν_0, goes to ν, the betatron oscillation length at the interaction point, β_0^*, goes to β^*, and the rms beam sizes, σ_{x0} and σ_{y0}, go to σ_x and σ_y. The variables with the zero subscripts are the unperturbed quantities. The motion of small amplitude particles is analyzed by using matrix techniques. We start with the Courant-Synder matrix in Eq. (2.7), which gives:

$$\begin{pmatrix} x \\ x' \end{pmatrix}_{n+1} = \begin{pmatrix} \cos(2\pi\nu) & \beta^* \sin(2\pi\nu) \\ -\frac{1}{\beta^*}\sin(2\pi\nu) & \cos(2\pi\nu) \end{pmatrix} \begin{pmatrix} x \\ x' \end{pmatrix}_n , \tag{3.20}$$

where $x' = dx'/ds$, s is the coordinate along the collider, the indices n and $n+1$ refer to the turn number, and for simplicity we have taken $\alpha = 0$. A similar matrix can be written for the y direction. The matrix in Eq. (3.20) representing the perturbed matrix can be expressed in terms of perturbed and unperturbed quantities:

$$\begin{pmatrix} \cos(\mu) & \beta^* \sin(\mu) \\ -\frac{1}{\beta^*}\sin(\mu) & \cos(\mu) \end{pmatrix} = B \begin{pmatrix} \cos(\mu_0) & \beta_0^* \sin(\mu_0) \\ -\frac{1}{\beta_0^*}\sin(\mu_0) & \cos(\mu_0) \end{pmatrix} B, \tag{3.21}$$

where

$$B = \begin{pmatrix} 1 & 0 \\ -\frac{2\pi\xi_x}{\beta_0^*} & 1 \end{pmatrix}, \tag{3.22}$$

$\mu = 2\pi\nu$, $\mu_0 = 2\pi\nu_0$, and ξ_x is the beam strength parameter:

$$\xi_x = N r_0 \beta_0^* / 2\pi\gamma\sigma_x(\sigma_x + \sigma_y) . \tag{3.23}$$

The matrix B represents beam-beam kick through half of the interaction point. There is a similar expression for y transfer matrix. From these transfer matrices the following relations can be derived:

$$\cos\mu = \cos\mu_0 - 2\pi\xi_x \sin\mu_0 \tag{3.24}$$

$$\beta_0^*/\beta^* = \sin\mu / \sin\mu_0 . \tag{3.25}$$

Note that for $\xi \ll 1$ Eq. (3.24) reduces to

$$\mu \approx \mu_0 + 2\pi\xi\,, \tag{3.26}$$

which can be rewritten as

$$\nu \approx \nu_0 + \xi\,, \tag{3.27}$$

where ξ is equal to the beam-beam tune shift parameter $\Delta\nu = \nu - \nu_0$. In the weak-strong case Eqs. (3.24) and (3.25) are the same. However, since the strong beam, which kicks the weak beam, is unperturbed, ξ_x is defined in terms of unperturbed quantities:

$$\xi_x = N r_0 \beta_0^* / 2\pi\gamma\sigma_{x0}(\sigma_{x0} + \sigma_{y0})\,. \tag{3.28}$$

Stability of the particle motion is achieved, when $|\cos\mu| \leq 1$ in Eq. (3.24). The stability conditions are

$$\xi < \cot(\mu_0/2)/2\pi \tag{3.29}$$

$$\xi_0 < \cot(\mu_0/2)/2\pi\,, \tag{3.30}$$

where the first equation is for the strong-strong (coherent) case and the second equation is for the weak-strong (incoherent) case. The stability diagram from these equations is shown in Figure 3.2, which shows the stable and unstable regions in $\xi - \nu$ space.[8] In the weak-strong case ξ would be replaced by ξ_0 in the figure. Note that resonances occur at

$$\frac{\mu}{2\pi} = \nu \approx \frac{n}{2}, \tag{3.31}$$

where n is an integer. The beam strength parameter ξ and the tune shift $\Delta\nu$ are related by

$$\xi(\Delta\nu) = \frac{\cos(2\pi\nu) - \cos\left(2\pi(\nu + \Delta\nu)\right)}{2\pi\sin(2\pi\nu)}. \tag{3.32}$$

When $|\xi| \ll 1$, then $\Delta\nu \approx \xi$.

In the strong-strong case the perturbed quantities are interdependent—that is, σ_x is proportional to $\sqrt{\beta^*}$ and not $\sqrt{\beta_0^*}$. The perturbed betatron oscillation length β^* depends on ξ, which in turn depends on σ_x. This implies that σ_x, β^*, μ, ξ, and L (luminosity) need to be found self-consistently for a given N.

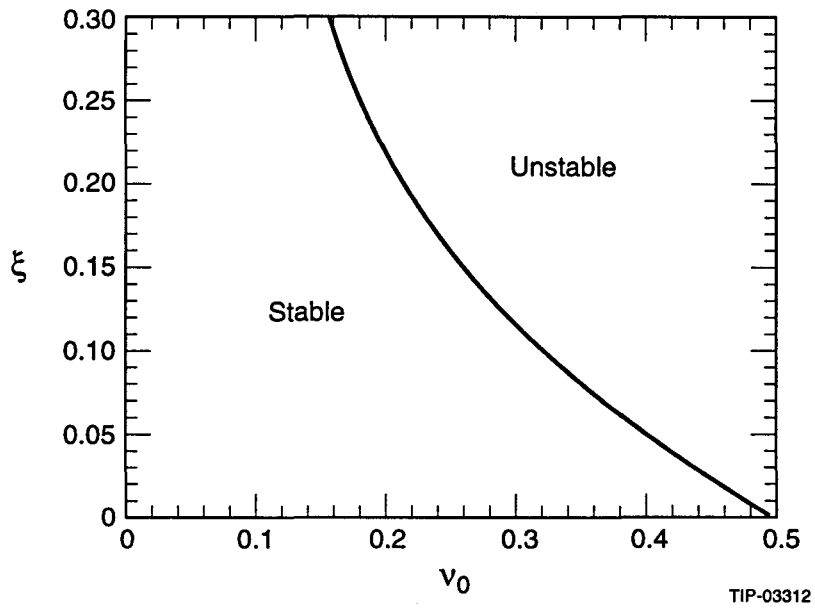

Figure 3.2. Stability of a Uniform Cylindrical Beam to Beam-Beam Perturbations, Where ξ is Plotted Versus ν_0.

For example, for a round beam $\sigma_x = \sigma_y$ and $\mu_{x0} = \mu_{y0} = \mu_0$. Defining $\rho_0 = 2\pi\xi_0$, we get from Eqs. (3.25) and (3.24):

$$\left(\frac{\beta_0^*}{\beta^*}\right)^2 = 1 + 2\rho_0 \cot\mu_0 \frac{\beta_0^*}{\beta^*} - \rho_0^2 \left(\frac{\beta_0^*}{\beta^*}\right)^2 . \tag{3.33}$$

From Eq. (3.33), we get an equation for the perturbed betatron oscillation length β^* in terms of unperturbed quantities:

$$\frac{\beta^*}{\beta_0^*} = (1 + [\rho_0/\sin\mu_0]^2)^{1/2} - \rho_0 \cot\mu_0 . \tag{3.34}$$

Also, all other perturbed quantities can be calculated based on the fact that

$$\xi/\xi_0 = \sigma_0^2/\sigma^2 = \beta_0^*/\beta^* = L/L_0 , \tag{3.35}$$

where quantities with subscript 0 are the unperturbed quantities. We have assumed that the beam-beam interaction does not change the phase space area occupied by the beam particles.

The dynamic beta model can be generalized by allowing the two beams to behave differently:

$$\left(\frac{\beta_0^*}{\beta_+^*}\right)^2 = 1 + 2\rho_0 \cot\mu_0 \frac{\beta_0^*}{\beta_-^*} - \rho_0^2 \left(\frac{\beta_0^*}{\beta_-^*}\right)^2 \tag{3.36}$$

$$\left(\frac{\beta_0^*}{\beta_-^*}\right)^2 = 1 + 2\rho_0 \cot\mu_0 \frac{\beta_0^*}{\beta_+^*} - \rho_0^2 \left(\frac{\beta_0^*}{\beta_+^*}\right)^2 , \tag{3.37}$$

where

$$\beta_0^*/\beta_\pm^* = \sigma_0^2/\sigma_\pm^2 . \tag{3.38}$$

One solution is $\beta_+^* = \beta_-^*$. There is another set of solutions with $\beta_+^* \neq \beta_-^*$:

$$\frac{\beta_\pm^*}{\beta_0^*} = \frac{1}{\rho_0^2 - 1}\rho_0 \cot \mu_0 \pm \sqrt{\frac{\rho_0^2 \cot^2 \mu_0(\rho_0^2 - 3) + (\rho_0^2 - 1)^2}{\rho_0^2 + 1}} . \tag{3.39}$$

The two different solutions for β^* imply that one beam is statically blown up (β_+^*), and the other pinches (β_-^*). This solution with different β^* is a model for "flip-flop."[7]

3.2 Steady State Distribution

The dynamic beta model is good only when the beam-beam force is linear in x and y. A linearized beam-beam force is inconsistent with a Gaussian distribution where the force is nonlinear for large amplitude in x or y. There may be two ways to proceed:

- Include nonlinear beam-beam force in x and y for Gaussian beams, but consider only the second moment. This approximation is still not self-consistent.[11]
- Restart with the Vlasov equation and take into account self-consistency.

The two beam distributions are coupled (assuming flat beams) through:

$$\frac{\partial \Psi_1}{\partial s} + y' \frac{\partial \Psi_1}{\partial y} - F_2(y,s)\frac{\partial \Psi_1}{\partial y'} = 0 \tag{3.40}$$

$$\frac{\partial \Psi_2}{\partial s} + y' \frac{\partial \Psi_2}{\partial y} - F_1(y,s)\frac{\partial \Psi_2}{\partial y'} = 0 , \tag{3.41}$$

where

$$F_j(y,s) = K(s)y + F_b \tag{3.42}$$

$$F_b = \frac{2\pi N r_0}{L_x \gamma}\delta_p(s) \int_{-\infty}^{\infty} d\bar{y} H(y - \bar{y}) \rho_j(\bar{y}) \tag{3.43}$$

$$= \frac{2\pi N r_0}{L_x \gamma}\delta_p(s) \int_{-\infty}^{\infty} d\bar{y} H(y - \bar{y}) \int_{-\infty}^{\infty} d\bar{y}' \Psi_j(\bar{y}, \bar{y}', s) , \tag{3.44}$$

with $H(x) = 1$ if $x > 0$, and $H(x) = -1$ if $x < 0$, and $\delta_p(s)$ a periodic δ-function with period $s = L$. The equal-beam steady state self-consistent distribution satisfies

$$\frac{\partial \Psi_0}{\partial s} + y' \frac{\partial \Psi_0}{\partial y} - F_0(y,s)\frac{\partial \Psi_0}{\partial y'} = 0 , \tag{3.45}$$

where

$$F_0(y,s) = K(s)y + F_b \tag{3.46}$$

$$F_b = \frac{2\pi N r_0}{L_x \gamma} \delta_p(s) \int_{-\infty}^{\infty} d\bar{y} H(y - \bar{y}) \rho_j(\bar{y}) \tag{3.47}$$

$$= \frac{2\pi N r_0}{L_x \gamma} \delta_p(s) \int_{-\infty}^{\infty} d\bar{y} H(y - \bar{y}) \int_{-\infty}^{\infty} d\bar{y}' \Psi_0(\bar{y}, \bar{y}', s) . \tag{3.48}$$

There are a few solvable cases. One solution is obtained when the beam-beam force is proportional to $\delta_p(s)y$ and is similar to the dynamic beta model. The solution does not give the assumed beam-beam force. It is also not self-consistent except for uniform distributions. Another solvable case is for two oppositely-charged, unbunched (continuous), round beams self-pinching with line density λ_0. The beam-beam force is independent of s. There is no resonance structure. Then

$$\Psi_0 = \frac{e\lambda_0 \exp\left(-\frac{x'^2+y'^2}{2\sigma'^2}\right)}{2\pi^2 \sigma'^2 A^2 (1 + \frac{x^2+y^2}{A^2})^2} , \tag{3.49}$$

where

$$\sigma'^2 = \lambda_0 r_0 / \gamma \tag{3.50}$$

and A is an arbitrary constant.[8,12]

These solvable cases have limitations. The linearized $\delta_p(s)$ beam-beam force sees only $\nu_0 = 1/2$ resonances. The smoothed beam-beam force sees no resonances.

In general, Ψ_0 is "transverse potential well distorted"[8] and is difficult to solve. Note that unlike the longitudinal potential well distortion due to wake fields, this potential well excites resonances $\nu_0 = p/q$, where p and q are integers. The periodic delta function, $\delta_p(s)$, is not in the longitudinal potential well distortion.

3.3 Dynamics About the Steady State

The key is to determine whether the motion is stable against small perturbations from the steady state. Table 3.1 shows the steps that have been taken to study the beam-beam interaction problem.[8] The cases are listed in decreasing order of confidence. Case 1 represents the simplest coherent beam-beam model that includes dynamics.[13–15]

Table 3.1. Cases That Have Been Studied in Coherent Beam-Beam Dynamics in Increasing Complexity.

Case	steady state	perturbation
1	unperturbed	rigid center-of-mass
2	unperturbed	perturbation on rms beam sizes
3	dynamic beta	perturbation on rms beam sizes
4	unperturbed	higher order modes
5	dynamic beta	higher order moments
6	potential well distorted distribution	repeat cases 1–5
7	potential well distorted and flip-flop	repeat cases 1–5

For case 1 we assume rigid round beams. Let the unperturbed distribution be $\Psi(r)$ and the center-of-mass coordinate be Y. The center-of-masses exert beam-beam kicks on each other for small Y's:[11,16]

$$\Delta Y_1' = -\frac{G}{f}(Y_1 - Y_2) \tag{3.51}$$

$$\Delta Y_2' = -\frac{G}{f}(Y_2 - Y_1)\,, \tag{3.52}$$

where f is the focal length for incoherent motion, for example, $\Delta y' = -y'/f$, and $1/f = 4\pi\xi_0/\beta_0^*$. The beam-beam kick is averaged over $\Psi(r)$, where G is the form factor:

$$G = \frac{\int_0^\infty dr\ r\ \Psi^2(r)}{\Psi(0)\int_0^\infty dr\ r\ \Psi(r)}\,. \tag{3.53}$$

$G = 1/2$ for a round Gaussian beam and 1 for a round uniform disk. Considering one bunch per beam the transformation for $[Y_1, Y_1', Y_2, Y_2']$ from interaction point to interaction point is

$$\begin{bmatrix} 1 & 0 & 0 & 0 \\ -G/f & 1 & G/f & 0 \\ 0 & 0 & 1 & 0 \\ G/f & 0 & -G/f & 1 \end{bmatrix} \times R\,, \tag{3.54}$$

where

$$R = \begin{bmatrix} \cos\mu_0 & \beta_0^*\sin\mu_0 & 0 & 0 \\ -\frac{1}{\beta_0^*}\sin\mu_0 & \cos\mu_0 & 0 & 0 \\ 0 & 0 & \cos\mu_0 & \beta_0^*\sin\mu_0 \\ 0 & 0 & -\frac{1}{\beta_0^*}\sin\mu_0 & \cos\mu_0 \end{bmatrix}. \tag{3.55}$$

By performing eigenmode analysis it can be shown that there are two modes: the O-mode and the π-mode. With the O-mode the two bunches move up and down together (or left and right). There is no coherent beam-beam force, and $\mu = \mu_0$ the tune maintains the unperturbed value. This mode is always stable. For the π-mode the two bunches are out of phase. The effective separation is $2G$ larger than the incoherent case (G is the form factor and the 2 is due to both beams moving). The mode frequency μ satisfies Eq. (3.24) with $\xi \to 2G\xi_0$. The motion is stable if $\pi-$mode is stable. For example,

$$\xi_0 < \cot(\mu_0/2)/4\pi G. \tag{3.56}$$

Resonance occurs when $\mu_0 = \pi$, or $\nu_0 = 1/2$, which is just like the incoherent and dynamic beta cases. The O-mode and the π-mode have been observed experimentally.[17]

When the beams are not rigid, the beam motion is determined by the sum of all beam modes (Table 3.2). Consider one bunch per beam. The bunches collide head-on, but each executes coherent quadrupole oscillation. Define[8]

$$\Sigma = \begin{vmatrix} \langle x^2 \rangle & \langle xx' \rangle & 0 & 0 \\ \langle xx' \rangle & \langle x^2 \rangle & 0 & 0 \\ 0 & 0 & \langle y^2 \rangle & \langle yy' \rangle \\ 0 & 0 & \langle yy' \rangle & \langle y^2 \rangle \end{vmatrix}, \tag{3.57}$$

where there is one of these arrays for each bunch. Consider small perturbations around a steady state:

$$\Sigma_- = \Sigma_0 + \Delta\Sigma_- \tag{3.58}$$

$$\Sigma_+ = \Sigma_0 + \Delta\Sigma_+ . \tag{3.59}$$

The transformations for the Σ matrices are in the arcs (round beams):

$$(\Delta\Sigma_\pm)_{out} = R(\Delta\Sigma_\pm)_{in}\tilde{R}. \tag{3.60}$$

At the interaction point,

$$(\Delta\Sigma_+)_{out} = T_{BB-}(\Delta\Sigma_+)_{in}\tilde{T}_{BB-} \tag{3.61}$$

$$(\Delta\Sigma_-)_{out} = T_{BB+}(\Delta\Sigma_-)_{in}\tilde{T}_{BB+}, \tag{3.62}$$

where $T_{BB\pm}$ is the perturbed beam-beam matrix (linearized):

$$T_{BB\pm} = \begin{bmatrix} 1 & 0 & 0 & 0 \\ -\frac{1}{f_\pm} & 1 & 0 & 0 \\ 0 & 0 & 1 & 0 \\ 0 & 0 & -\frac{1}{f_\pm} & 1 \end{bmatrix}. \tag{3.63}$$

This matrix determines the effect on one beam at the interaction point due to the oscillating beam size of the other beam.

Table 3.2. Beam Modes and Associated Resonances.

mode	resonances
rigid dipole	total tune $\nu = n$
quadrupole	$\nu = n/2$
sextupole	$\nu = n/3$
etc.	

Linearize this with respect to the elements in $\Delta\Sigma_{\pm}$ for small perturbations. This will result in 12×12 transformation matrices that can be eigen-analyzed for six modes. Two of the six modes give constants of the motion. The remaining four dynamic modes give

$$\cos\mu = \cos 2\bar{\mu} + \begin{bmatrix} 2 \\ 1 \\ -1 \\ -2 \end{bmatrix} \rho_0 \sin\mu_0 \cos\bar{\mu} \tag{3.64}$$

$$\cos\bar{\mu} = \cos\mu_0 - \rho_0 \sin\mu_0 \,. \tag{3.65}$$

One can obtain a stability diagram from these equations. A similar analysis can be performed for M bunches per beam. From this one gets $4M$ dynamic modes.

The dynamic beta analysis gives a steady-state second moment. The dynamics of the second moment is given by transformation matrices for $\Delta\Sigma_{\pm}$. This formulation was based on a linear beam-beam force that is inconsistent with a Gaussian beam. With a nonlinear beam-beam force, higher moments are excited, the distribution is non-Gaussian, and the beam-beam force is modified. A self-consistent (Vlasov) treatment is needed.

3.4 Vlasov Approach

A general approach to the analysis of the beam-beam interaction is to use the Vlasov equation.[18–21] Let

$$\Psi_{1,2} = \Psi_0 + \Delta\Psi_{1,2} \,, \tag{3.66}$$

where Ψ_0 is the steady-state distribution and $\Delta\Psi_{1,2}$ are the perturbations. Chao and Ruth[18] linearized the Vlasov equation in $\Delta\Psi$, transformed to action-angle variables (J, ϕ), and assumed a waterbag model:[8,18]

$$\Psi_0 = (1/\pi\epsilon) H(\epsilon/2 - J) \,, \tag{3.67}$$

where ϵ is the unperturbed beam emittance, J is the action, and

$$H(x) = \begin{matrix} 1 & \text{for} & x > 0 \\ 0 & \text{for} & x < 0 \end{matrix} . \tag{3.68}$$

The waterbag model is simple but inconsistent with the steady-state condition.

The coherent beam-beam instability is pronounced near

$$\nu = 2\nu_0 \approx p/q . \tag{3.69}$$

The q-th mode is the most perturbed where

$$\Delta\Psi \sim \exp(iq\phi) , \tag{3.70}$$

and the mode frequency is[18]

$$\cos\mu = \cos(2\pi q\nu) \pm \frac{8q}{4q^2 - 1}\xi \sin(2\pi q\nu) . \tag{3.71}$$

The stopband width around a resonance is

$$\delta\nu_q = \frac{\xi}{2\pi}\frac{16}{4q^2 - 1} . \tag{3.72}$$

The stopband is a region around a resonance in which the beams are unstable. Figure 3.3 shows the stability diagrams for two bunches per beam, where the beams are of opposite charge.[18] As the number of modes is increased, higher and higher resonances can be excited. When the maximum number of modes is n, the highest resonances are excited near $\nu = m/n$.

Beams blow up in the unstable regions, but only by so much that stability sets in, for example, just under the sawtooth curve. This stabilization is analogous with bunch-lengthening observed in electron storage rings and has already been hinted by dynamic β analysis where the beam blows up but stays below the instability.

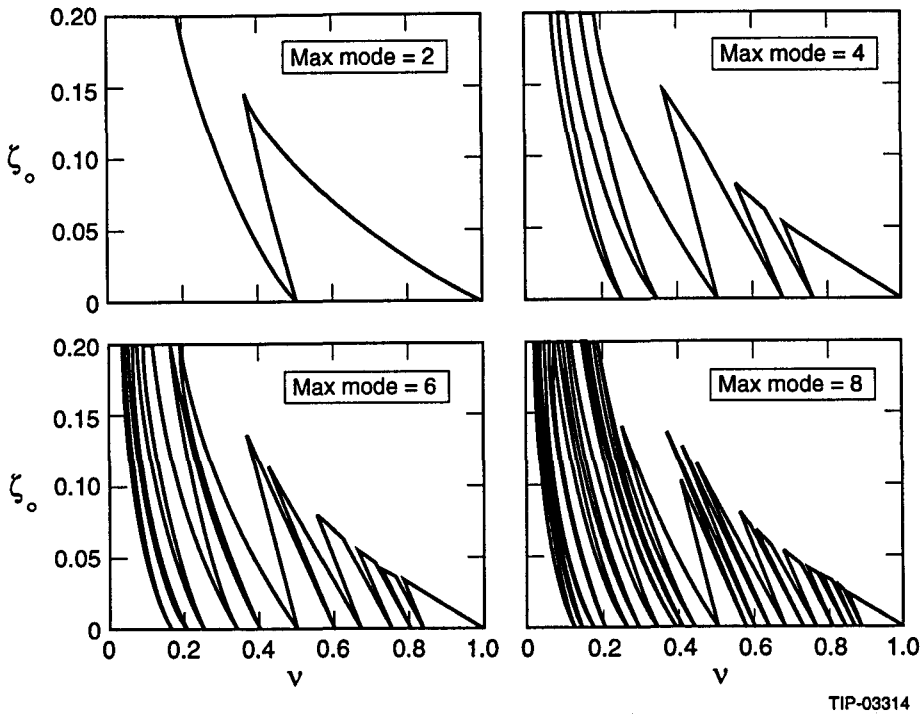

Figure 3.3. Stability Diagrams for the Case of Two Bunches per Beam and Maximum Modes of $m = 2, 4, 6,$ and 8.

3.5 Diffusion from Beam Offset

Another contribution of the beam-beam interaction is the enhancement of particle diffusion. It is anticipated that at each collision the pair of colliding beams suffer collisions with the centers of the beams offset, instead of head-on, resulting in diffusion of the beam particles, as they experience stochastic kicks. According to analytic theory on beam offset,[22] a Fokker-Planck equation can be derived for the averaged perturbation of the distribution function $\Delta F = F - F_0$:

$$< \Delta F >= \frac{1}{2}\frac{\partial}{\partial J} < (\Delta J_M)^2 > \frac{\partial F_0}{\partial J}, \tag{3.73}$$

where F_0 is the initial unperturbed distribution function of the beam, J is the action, and $< (\Delta J_M)^2 >$ is the averaged change in the action due to beam offsets. $< (\Delta J_M)^2 > /2$ can be thought of as the diffusion coefficient. An expression for $< (\Delta J_M)^2 >$ has been derived using the "weak-strong" approximation for the beam-beam interaction and the assumption that the strong beam is Gaussian:[22]

$$< (\Delta J_M)^2 >= 16\pi^2\xi^2 J_0 \exp(-J_0) M \sum_{k=0}^{\infty} \left[I_k\left(\frac{J_0}{2}\right) + I_{k+1}\left(\frac{J_0}{2}\right)\right]^2 R_k, \tag{3.74}$$

where ξ is the beam strength parameter, J_0 is the unperturbed action, I_k is the modified Bessel function of order k, and R_k is

$$R_k \equiv \sum_{n=-\infty}^{\infty} K(n) \cos\left(2\pi\nu n(2k+1)\right), \tag{3.75}$$

where $K(n)$ is the auto-correlation function $< \zeta_m \zeta_{m+n} >$, ζ_m is the beam offset for turn m, and ν is the tune.

Equation (3.74) can be simplified with the assumption that the beam offsets ζ are uncorrelated on a turn-by-turn basis. Then, $K(0)$ is the only non-zero term in the calculation of R_k (the Markov process assumption). Also noting that the Bessel functions fall off with k, Eq. (3.74) can be written in the form:[22]

$$< (\Delta J_M)^2 >= 16\pi^2\xi^2 J_0 \exp(-J_0) M \left[I_0\left(\frac{J_0}{2}\right) + I_1\left(\frac{J_0}{2}\right)\right]^2 R_0 . \tag{3.76}$$

After integrating over J_0, an approximate value for the diffusion coefficient can be obtained from the change in the luminosity of the beam:[22]

$$\frac{\Delta L}{L_0} = -6.25\xi^2 M \frac{\delta x^2}{\Delta\nu}, \tag{3.77}$$

where ΔL is the change in luminosity, L_0 is the initial luminosity, ξ is the beam strength parameter, δx is the beam displacement normalized to σ_x, M is the number of turns, and $\Delta\nu$ is the distance of the tune ν from the nearest integer. The diffusion coefficient may be defined as

$$D = \frac{d(\frac{\Delta L}{L_0})}{dM}. \tag{3.78}$$

Thus, D can be expressed in the form:

$$D = -6.25\xi^2 \frac{\delta x^2}{\Delta\nu}. \tag{3.79}$$

4.0 FILAMENTATION INSTABILITY

When collective effects are taken into account between two counterstreaming beams, one of the most important instabilities is the filamentation instability.[23] The filamentation instability is one of the fastest growing collective effects that can occur in a plasma. From linear theory the maximum growth rate for counterstreaming electron and positron beams is[23]

$$\Gamma_{max} = \frac{1}{2}\frac{\omega_b}{\sqrt{\gamma}}, \tag{4.1}$$

where $\gamma = \frac{1}{\sqrt{1-\beta^2}}$, $\beta = \frac{v}{c}$, $\omega_b^2 = 4\pi e n_b/m_e$, n_b is the beam density, and m_e is the electron or positron mass. The filamentation instability generates a mode that propagates nearly

perpendicular to the beam direction. The onset of this instability can lead to beam filamentation and heating. Lee and Lampe[24] have studied a relativistic electron beam in a plasma via simulations. They found that as a result of the filamentation instability the electron beam splits into filaments, each of which self-pinches.

There are two factors that may determine the effect of the filamentation instability on collective motion of counterstreaming beams in circular accelerators. They are the time scale of the interaction and the transverse size of the beam. The time scale of the interaction τ_{int} is determined by the length of the beam bunches L_b, where $\tau_{int} = L_b/2c$. The maximum growth rate of the filamentation instability for large beams is $\Gamma_{max} = \omega_b/2$ for $p - \bar{p}$ collisions and for $p - p$ collisions, where $\omega_b = \sqrt{4\pi e^2 n_b/\gamma m}$ is the beam plasma frequency, n_b is the beam density, γ is the relativistic factor, and m is the proton mass.[23] The factor $\Gamma_{max}\tau_{int}$ determines the fraction of the growth rate time the beams interact. The fraction of the growth rate varies between different types of colliders. In the SSC the beams interact for a small fraction of the growth time of the instability ($\Gamma_{max}\tau_{int} \approx 0.035$). Therefore, the only way the filamentation instability may be of some importance to the beam dynamics is by repeated interactions over many turns. Since the typical beam life is $\approx 10^8$ revolutions, the effects of the filamentation instability may be important. In electron synchrotrons the fraction of the growth rate is higher because the growth rate increases with the decrease in mass. So the filamentation instability could be more significant over a smaller number of rotations.

The transverse size of the beam may be another factor limiting the effects of the filamentation instability. The typical scale of the filamentation instability is the collisionless skin depth $\lambda_c = c/\omega_b$. It has been found that the filamentation instability is suppressed when the beam width w_b is small compared to λ_c.[25] For the SSC the ratio of w_b to λ_c is $\approx 2 \times 10^{-5}$, so both the fraction of the interaction time and the width of the beam are small.

5.0 PREVIOUS BEAM-BEAM SIMULATION RESULTS

Since a complete analytical treatment of beam-beam interaction does not yet exist,[8] study of the problem has relied heavily on various types of computer codes. In this section a review of previous simulation results is presented. Substantial use is made of the review article by Siemann[26] on electron-positron storage rings.

Two main types of computer codes have been used to study the beam-beam interaction: weak-strong codes[27] and strong-strong codes.[28,29] Typically the 10^{10}–10^{11} beam particles are simulated with 10^3–10^4 simulation particles. In the strong-strong simulations both beams are tracked, and the evolution of their phase space distributions is followed. The

purpose of these programs is to measure the effects of storage ring parameters on the beam core. In the weak-strong simulations one beam (weak beam) is tracked and the other beam (strong beam) is kept stationary. The weak beam is perturbed by the strong beam's scattering potential. Weak-strong simulations cannot be used to study the beam core. However, they are mainly used to study the dynamics of particles in the tails of the beam distribution. The goal of tracking is to directly simulate single-particle motion in circular accelerators and to determine regions of phase space that are stable.[30]

The simulation particles are tracked for many turns. For each turn the particles pass through each other at the interaction point (IP) and are then transported through the rest of the storage ring via matrices representing the various magnetic transport components.

At the IP the usual approximations are made that the beams are Gaussian in the transverse directions, x and y, and can be treated as thin elements along the collider in s. By treating the beams as thin elements the kick approximation can be made.[31] In this approximation the fields are determined by the rms width in x and y of the opposing beam. The approximation of the kick for the beam-beam interaction is valid so long as the betatron oscillation length at the IP β^* is not comparable to the longitudinal length of the beam σ_l. When σ_l is comparable to β^*, it is necessary to treat the beam-beam interaction as a thick element. In the weak-strong simulation the rms values are fixed. In the strong-strong simulations the rms widths are varying for each beam.

In the strong-strong simulations the particles are initialized in the simulation with Gaussian distributions and the required variances.[28,29] The particles are tracked through a sector—an accelerating cavity, a beam-beam interaction, and a normal machine arc (lattice)—and particles exceeding the aperture limits are removed from the simulation. The aperture limits in the transverse direction are determined by machine acceptance, and in the longitudinal phase plane they are determined by acceptance of the rf accelerating "bucket."

After each turn new beam parameters are computed; for example, beam size and intensity are computed and used to recalculate the beam-beam force parameters. The beam size is calculated from the rms value of the displacements of the superparticles. This value is used as the sigma of the assumed Gaussian distribution. The beam-beam kick is evaluated by linear interpolation of tabulated values of the complex error function:[28,29]

$$\Delta z' = \frac{N r_e}{\gamma}\sqrt{\frac{2\pi}{a^2-b^2}}Re\left[w\left(\frac{x+iz}{\sqrt{2(a^2-b^2)}}\right) - \exp\left(-\frac{x^2}{2a^2}-\frac{z^2}{2b^2}\right)w\left(\frac{x\frac{b}{a}+iz\frac{a}{b}}{\sqrt{2(a^2-b^2)}}\right)\right], \tag{5.1}$$

where $\Delta z'$ is the kick in the vertical kick, a and b are the standard deviations in the x and z directions, Ne is the total charge in the bunch, γ is the relativistic parameter, and $w(A+iB)$ is the complex error function.

Typically the simulations uses about 100 particles, and beam size reaches steady-state value in less than one-half of a transverse-damping time. Simulations are run to one damping time after the steady-state equilibrium has been reached. Statistical fluctuations associated with each bunch are rather large due to the limitations on the number of superparticles that can be used. So it is difficult to obtain reliable information about the form of the distribution function or about the tails of the distribution function. Once an apparent steady state distribution has been reached in the presence of beam-beam forces, the statistical fluctuations may be reduced. Binning the particles into histograms after traversal of each machine sector over many turns accomplishes this reduction.[28,29] This binning of particles has been applied to the computation of distributions in the betatron and synchrotron tune and in betatron and synchrotron displacement.[29] This method of binning also allows the calculation of the average tune shift and the tune spread for one or all beam-beam crossings.

In the absence of the beam-beam interaction the beams would remain Gaussian. However, because of the beam-beam interaction the strong-strong beams do not remain Gaussian, as shown in Figure 5.1 from Siemann.[26] The beam profile is non-Gaussian in both the core and the tails. Beam-beam resonances are modifying the distribution. The deviation of the beams from the Gaussian profile is the main problem with these types of simulations. The fields are calculated based on a Gaussian, which is inconsistent with the actual distribution of the particles. Therefore, the beams may be prevented from reaching a distribution that is self-consistent with the fields.

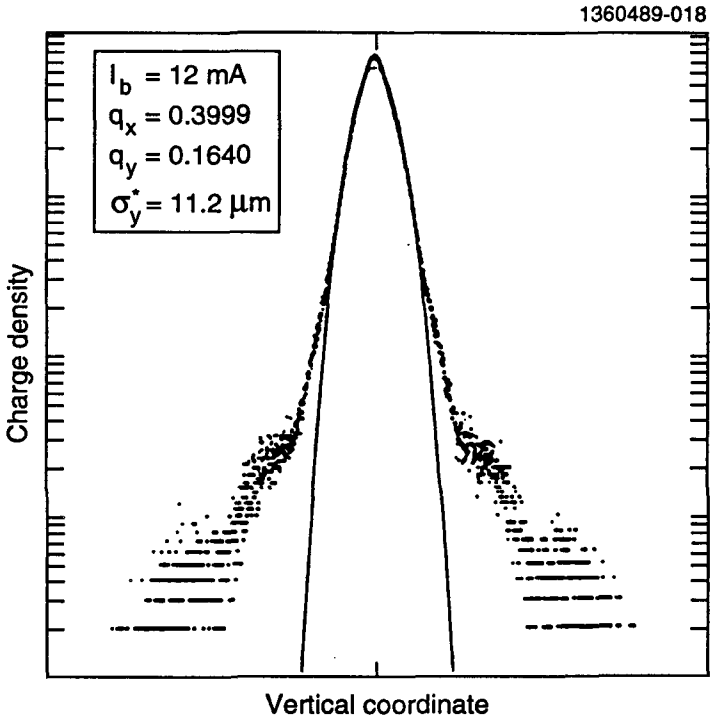

Figure 5.1. Simulation of the Vertical Beam Profile. The histogram is the result of binning each test particle over 1000 turns. The solid curve is the original Gaussian profile of the beam.

Both qualitative and quantitative comparisons between simulations and storage ring experiments have been made. Piwinski reported qualitative agreement between simulations and the operating point characteristics for PETRA.[32] Simulations show that the beam-beam interaction is dominated by resonances, as shown in Figure 5.2, where a Poincare map of the motion of a single test particle near the 1/3 resonance is plotted.[32] At the beginning of the simulation the particle is near the origin. After about 8000 turns, the particle is moved quickly out to the resonance islands from quantum fluctuations and the nonlinear beam-beam force. Myers has found in the Large Electron-Positron Collider (LEP) storage ring simulations[29] that:

- beam-beam limit decreases slightly with the number of bunches
- beam-beam limit decreases rapidly when the value of β^* approaches around twice the bunch length (σ_s)
- beam-beam limit is strongly dependent on the transverse damping
- transverse tune modulation caused by residual chromaticity produces no significant reduction in the beam-beam limit.
- machine "errors" can produce significant reduction in the beam-beam limit.

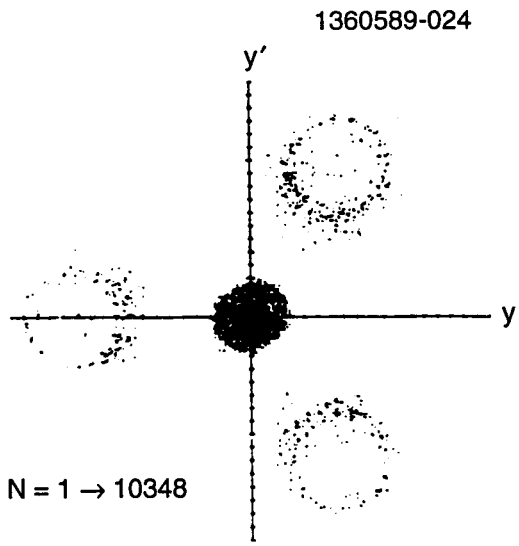

Figure 5.2. Poincare Map of a Test Particle, Where $\nu_x = 25.2$ and $\nu_y = 23.32$ After 10,348 Turns.

Hutton[33] compared the Positron-Electron Project (PEP) luminosity at two machine operating points with the strong-strong simulation of Myers.[29] Agreement was found between the absolute luminosity and the current dependence. Jackson and Siemann have found similar agreement with the Cornell Electron Storage Ring (CESR).[28] They also compared simulation results with CESR results away from operating points. Good agreement was found in some regions around the operating point for the luminosity versus the tune. Qualitative agreement was found in other regions. Substantial disagreement was found from low vertical tune values.[28] Weak-strong simulations of CESR show good agreement for beam blow-up by resonances and particle distributions in the tails.[34]

Recently, non-Gaussian simulations have been performed.[35] The simulations show that it is critical to use general field calculations in the study of coherent beam-beam phenomena. Higher-order coherent resonances were a direct consequence of the general field calculation.

6.0 SIMULATION MODELS

In the course of our investigation, various simulation models have been developed to study the beam-beam interaction. These models are presented in increasing order of sophistication and inclusion of physical effects.

Numerical simulation of accelerator beam dynamics has a relatively short history. As accelerators become increasingly more costly and complex, computers and computational techniques become increasingly more developed. Computer simulation has recently become an accepted standard method of investigation of accelerators. It certainly is this way for the Tevatron at Fermi National Accelerator Laboratory. For the SSC one may even say that computer simulation has become one of the central design techniques. An obvious

reason for developing computer models is the cost. It is much less expensive to run a simulation than to build a device. Also, simulations allow the study of a problem under very controlled conditions with accuracy limited only by the precision of the computer. This is not the case with experimental setups. Analytical methods provide a means to study the problem in the linear regime. However, nonlinear aspects are not easily accessible. Numerical methods allow the study of this regime with fewer approximations than analytic methods. Simulation schemes such as the Particle-in-Cell (PIC) methods[36,37] represent a common ground between the two-particle picture of the beam-beam interaction and the full statistical picture representing all particles in the beams.

In the following sections the various numerical codes used to study the beam-beam interaction will be described. They are the tracking code, Vlasov code, PIC codes, and the δf algorithm.

6.1 Tracking Code

The basic principle of tracking codes is to follow the dynamics of single particles around the machine.[27] In the beam-beam interaction the tracking code consists of two components: a target beam and a projectile beam. The target beam is treated as a rigid, smooth, Gaussian distribution of a large number of particles. It remains unchanged from interaction to interaction. The projectile beam is considered to be a collection of mutually noninteracting particles that are perturbed by the target beam. This is the so-called "weak-strong" approximation as described in Section 3.0. In tracking-code simulations in the "weak-strong" approximation, transport about one-turn is simulated as the product of two matrices, one for the one-turn Courant-Synder map,[5] and the other for the impulsive application of the beam-beam interaction discussed above:[27]

$$\begin{bmatrix} x \\ x' \end{bmatrix}_{final} = M \begin{bmatrix} x \\ x' \end{bmatrix}_{initial}, \tag{6.1}$$

$$M = \begin{bmatrix} \cos(2\pi\nu_0) & \beta_0^* \sin(2\pi\nu_0) \\ -\sin(2\pi\nu_0)/\beta_0^* & \cos(2\pi\nu_0) \end{bmatrix} \begin{bmatrix} 1 & 0 \\ 4\pi\Delta\nu_0 F(x)/\beta_0^* & 1 \end{bmatrix}, \tag{6.2}$$

where x is the position of the particle, x' is dx/ds, s is the distance along the collider, $\nu_0 = \oint ds/\beta(s)$ is the tune, $\Delta\nu_0$ is the input tune shift, β_0^* is the betatron oscillation amplitude at the interaction point (IP), and $F(x)$ is the 1-D truncation of the force from a round Gaussian beam

$$F(x) = \frac{1 - \exp\left(-x^2/2{\sigma_{x0}}^2\right)}{x^2/2{\sigma_{x0}}^2}, \tag{6.3}$$

where σ_{x0} is the beam standard deviation in x. This formulation is similar to that of Neuffer *et al.*;[27] however, here both beams are of the same charge. For comparison with one-dimensional simulation results, $F(x)$ becomes the force of a 1-D Gaussian slab:

$$F(x) = \sqrt{\frac{\pi}{2}}\left(\frac{\sigma_{x0}}{x}\right)\mathrm{erf}\left(\frac{x}{\sqrt{2}\sigma_{x0}}\right), \tag{6.4}$$

where erf is the error function.

The first matrix in Eq. (6.2) takes into account the particle motion from the lattice magnets.[5] The second matrix takes into account the kick from the beam-beam interaction.

6.2 Vlasov Code

This section describes a Vlasov-Maxwell code. Vlasov-Maxwell codes can be used to simulate various electromagnetic phenomena that occur in plasmas or charged-particle systems.[38,39]

In this simulation technique, a plasma is represented by a discretized version of the Vlasov-Maxwell system of equations. The Vlasov equation is a continuity equation representing a system of particles as a fluid in phase space. Thus it is free of the noise plaguing PIC models due to the finite number of discrete particles. On the other hand, it needs to follow greater dimensions (typically twice as many) than the PIC models, since it represents phase space instead of the configuration space. It is written in the form:[39]

$$\frac{\partial f_s}{\partial t} + \frac{\vec{p}_s}{m}\cdot\frac{\partial f_s}{\partial \vec{x}} + \vec{F}_s\cdot\frac{\partial f_s}{\partial \vec{p}} = 0, \tag{6.5}$$

where the subscript s refers to the individual species (background electrons, beam electrons, ions, *etc.*) and $\vec{F}_s$ is the Lorentz force:

$$\vec{F}_s = q_s(\vec{E} + \vec{v}_s \times \vec{B}/c). \tag{6.6}$$

One of the greatest shortcomings of the Vlasov model, that of too much grid space information, may be ameliorated by the adoption of the recent development of massively parallel computation. In this section we specifically describe the implementation of a 2-D Vlasov-Maxwell system on a MIMD (multiple instruction multiple data) parallel computer. A Vlasov-Maxwell code that is already running in parallel on the Connection machine[40] is chosen as an initial code platform. The fields $(\vec{E}, \vec{B})$ in the Lorentz force equation are obtained from the set of Maxwell's equations:

$$\nabla\cdot\vec{E} = 4\pi\rho, \tag{6.7}$$

$$\nabla\times\vec{E} = -\frac{1}{c}\frac{\partial\vec{B}}{\partial t}, \tag{6.8}$$

$$\nabla \cdot \vec{B} = 0\,, \tag{6.9}$$

$$\nabla \times \vec{B} = 4\pi \vec{J} + \frac{1}{c}\frac{\partial \vec{E}}{\partial t}\,. \tag{6.10}$$

The density ρ and current $\vec{J}$ are calculated self-consistently from

$$\rho(\vec{x}) = \sum_s q_s \int d\vec{p}\; f_s(\vec{x},\vec{p},t)\,, \tag{6.11}$$

$$\vec{J}(\vec{x}) = \sum_s q_s \int d\vec{p}\; \vec{v}_s\; f_s(\vec{x},\vec{p},t)\,. \tag{6.12}$$

In the current formulation the electrostatic field calculated from Eq. (6.7) is neglected. This approximation assumes that the charge density ρ is 0 everywhere at all times and, therefore, the electrostatic component of the field is 0. The approximation of $\rho = 0$ everywhere eliminates plasma oscillations from the system.

The Vlasov equation is discretized in two dimensions using a "splitting" technique.[39] In this technique the distribution function $f = f(v_{xi}, v_{zj}, x_k, z_l)$ is advanced in time in a four-step process for each species s:[39,41]

$$\begin{aligned} f_{ijkl}^{n+1/4} &= f_{ijkl}^{n} - \frac{\Delta t}{2\Delta x}\frac{p_{xi}}{\gamma_{ij}} \cdot (f_{k+1}^{n} - f_{k-1}^{n})_{ijl} \\ &\quad + \left(\frac{\Delta t}{2\Delta x}\frac{p_{xi}}{\gamma_{ij}}\right)^2 \cdot (f_{k+1}^{n} - 2f_{k}^{n} + f_{k-1}^{n})_{ijl} \end{aligned} \tag{6.13}$$

$$\begin{aligned} f_{ijkl}^{n+1/2} &= f_{ijkl}^{n+1/4} - \frac{\Delta t}{2\Delta z}\frac{p_{zj}}{\gamma_{ij}} \cdot (f_{l+1}^{n+1/4} - f_{l-1}^{n+1/4})_{ijk} \\ &\quad + \left(\frac{\Delta t}{2\Delta z}\frac{p_{zj}}{\gamma_{ij}}\right)^2 \cdot (f_{l+1}^{n+1/4} - 2f_{l}^{n+1/4} + f_{l-1}^{n+1/4})_{ijk} \end{aligned} \tag{6.14}$$

$$\begin{aligned} f_{ijkl}^{n+3/4} &= f_{ijkl}^{n+1/2} - \frac{\Delta t}{2\Delta p_x} F_{xjkl} \cdot (f_{i+1}^{n+1/2} - f_{i-1}^{n+1/2})_{jkl} \\ &\quad + \left(\frac{\Delta t}{2\Delta p_x} F_{xjkl}\right)^2 \cdot (f_{i+1}^{n+1/2} - 2f_{i}^{n+1/2} + f_{i-1}^{n+1/2})_{jkl} \end{aligned} \tag{6.15}$$

$$\begin{aligned} f_{ijkl}^{n+1} &= f_{ijkl}^{n+3/4} - \frac{\Delta t}{2\Delta p_z} F_{zikl} \cdot (f_{j+1}^{n+3/4} - f_{j-1}^{n+3/4})_{ikl} \\ &\quad + \left(\frac{\Delta t}{2\Delta p_z} F_{zikl}\right)^2 \cdot (f_{j+1}^{n+3/4} - 2f_{j}^{n+3/4} + f_{j-1}^{n+3/4})_{ikl}\,, \end{aligned} \tag{6.16}$$

where

$$F_{xjkl} = q_s \left(E_{xkl} + \frac{v_{zl}}{c} B_{ykl} \right)^{n+\frac{1}{2}} \tag{6.17}$$

$$F_{zikl} = q_s \left(E_{zkl} - \frac{v_{xl}}{c} B_{ykl} \right)^{n+\frac{1}{2}} , \tag{6.18}$$

and

$$E_{x_{kl}}^{n+\frac{1}{2}} = \frac{1}{2}(E_{x_{l+\frac{1}{2}}} + E_{x_{l-l+\frac{1}{2}}})_k \tag{6.19}$$

$$E_{z_{kl}}^{n+\frac{1}{2}} = \frac{1}{2}(E_{z_{k+\frac{1}{2}}} + E_{z_{k-\frac{1}{2}}})_l \tag{6.20}$$

$$B_{y_{kl}}^{n+\frac{1}{2}} = \frac{1}{2}(B_{y_{kl}}^{n+1} + B_{y_{kl}}^{n}) . \tag{6.21}$$

In each step the distribution function is advanced a full time step using only one term at a time in the Vlasov equation. The fractional time indices for the distribution function f at each step are used for notational purposes only. This discretization scheme is numerically stable when the following conditions are met:[39,41]

$$\frac{p_x \Delta t}{m \Delta x} < 1, \qquad \frac{p_z \Delta t}{m \Delta x} < 1 , \tag{6.22}$$

$$\frac{F_x \Delta t}{\Delta p_x} < 1, \qquad \frac{F_x \Delta t}{\Delta p_z} < 1 . \tag{6.23}$$

Maxwell's equations are written in a left-handed Cartesian system for convenience:

$$\frac{\partial E_x}{\partial t} = c \frac{\partial B_y}{\partial z} - J_x \tag{6.24}$$

$$\frac{\partial E_z}{\partial t} = -c \frac{\partial B_y}{\partial x} - J_z , \tag{6.25}$$

$$\frac{\partial B_y}{\partial t} = c \left[\frac{\partial E_x}{\partial z} - \frac{\partial E_z}{\partial x} \right] . \tag{6.26}$$

These equations are discretized in the following manner:

$$E_{x_{k+\frac{1}{2}\ l}}^{n+\frac{1}{2}} = E_{x_{k+\frac{1}{2}\ l}}^{n-\frac{1}{2}} - \Delta t J_{x_{k+\frac{1}{2}ll}}^{n} + \frac{c \Delta t}{\Delta z_l} \left(B_{y_{k+\frac{1}{2}\ l+\frac{1}{2}}}^{n} - B_{y_{k+\frac{1}{2}\ l-\frac{1}{2}}}^{n} \right) \tag{6.27}$$

$$E_{z_{k\ l+\frac{1}{2}}}^{n+\frac{1}{2}} = E_{z_{k\ l+\frac{1}{2}}}^{n-\frac{1}{2}} - \Delta t J_{z_{k\ l+\frac{1}{2}}}^{n} - \frac{c \Delta t}{\Delta x_k} \left(B_{y_{k+\frac{1}{2}\ l+\frac{1}{2}}}^{n} - B_{y_{k-\frac{1}{2}\ l+\frac{1}{2}}}^{n} \right) \tag{6.28}$$

$$B_{y\,k+\frac{1}{2}\,l+\frac{1}{2}}^{n+1} = B_{y\,k+\frac{1}{2}\,l+\frac{1}{2}}^{n} - \frac{c\Delta t}{\Delta x_k}\left(E_{z\,k+1\,l+\frac{1}{2}}^{n+\frac{1}{2}} - E_{z\,k\,l+\frac{1}{2}}^{n+\frac{1}{2}}\right)$$

$$- \frac{c\Delta t}{\Delta z_l}\left(E_{x\,k+\frac{1}{2}\,l+1}^{n+\frac{1}{2}} - E_{x\,k+\frac{1}{2}\,l}^{n+\frac{1}{2}}\right). \tag{6.29}$$

The currents J_x and J_z are calculated from

$$J_{x\,kl}^{n} = \sum_s q_s \sum_i \sum_j A_{ij} f_{sijkl}^{n} \left(\frac{p_{xi}}{m_0\gamma_{ij}}\right) \Delta v_x \Delta v_z \tag{6.30}$$

$$J_{z\,kl}^{n} = \sum_s q_s \sum_i \sum_j A_{ij} f_{sijkl}^{n} \left(\frac{p_{zj}}{m_0\gamma_{ij}}\right) \Delta v_x \Delta v_z\,, \tag{6.31}$$

where A_{ij} is a normalization constant, and then

$$J_{x\,k+\frac{1}{2}\,l}^{n} = \frac{1}{2}(J_{x\,k+1\,l}^{n} + J_{x\,k\,l}^{n}) \tag{6.32}$$

$$J_{z\,k\,l+\frac{1}{2}}^{n} = \frac{1}{2}(J_{z\,k\,l+1}^{n} + J_{z\,k\,l}^{n})\,. \tag{6.33}$$

A similar set of finite-difference equations for the Vlasov equation and Maxwell's equations can be written in cylindrical coordinates.

6.2.1 Boundary Conditions

The boundary conditions used are dependent on whether Cartesian or cylindrical coordinates are used for the test problem. In both geometries the boundary conditions are taken to be periodic in the z direction. In the case of Cartesian coordinates periodic boundary conditions are employed in the two spatial directions (x, z). Also the distribution functions are 0 beyond the momentum coordinate boundaries (p_x, p_z) for the Cartesian case and (p_r, p_z) for the cylindrical case.

In the case of cylindrical coordinates, conducting wall boundary conditions are employed at $r = R$, where R is the maximum radius of the domain. For conducting wall boundary conditions all field quantities, currents, and distribution function values are equal to 0. Handling the field, currents, and distribution function at $r = 0$ is a little trickier. The field quantity that needs special care is the $E_{z\,1\,l+\frac{1}{2}}$ field component. Its calculation requires the knowledge of $B_{\theta\,\frac{1}{2}\,l+1}$ for $r = 0$. By symmetry arguments the field $B_{\theta\,\frac{1}{2}\,l+1}$ can be said to equal $-B_{\theta\,\frac{3}{2}\,l+1}$, so the time advance equation becomes

$$E_{z\,1\,l+\frac{1}{2}}^{n+\frac{1}{2}} = E_{z\,1\,l+\frac{1}{2}}^{n-\frac{1}{2}} - \Delta t J_{z\,1\,l+\frac{1}{2}}^{n} - 2\frac{c\Delta t}{\Delta r_1}\left(B_{\theta\,\frac{3}{2}\,l+\frac{1}{2}}^{n}\right). \tag{6.34}$$

All other field quantities can be calculated once this field component is determined. The distribution function f_{ij1l} at the $r = 0$ boundary is also calculated using the symmetry

argument. In this case f_{ij2l} is chosen equal to f_{ij0l} because the distribution function is symmetric about $r = 0$. The time advance equation becomes

$$f_{ij1l}^{n+1/4} = f_{ij1l}^{n} + \left(\frac{\Delta t}{2\Delta x}\frac{p_{xi}}{\gamma_{ij}}\right)^2 \cdot 2(f_2^n - f_1^n)_{ijl} \,. \tag{6.35}$$

6.2.2 Square Geometry

The implementation of the code on the Intel i860 involves decomposing the spatial grid of the simulation into square blocks and assigning one node to each block. Each node communicates with four other nodes as shown in Figure 6.1. Communication between nodes must occur in four directions (North, South, East, and West).

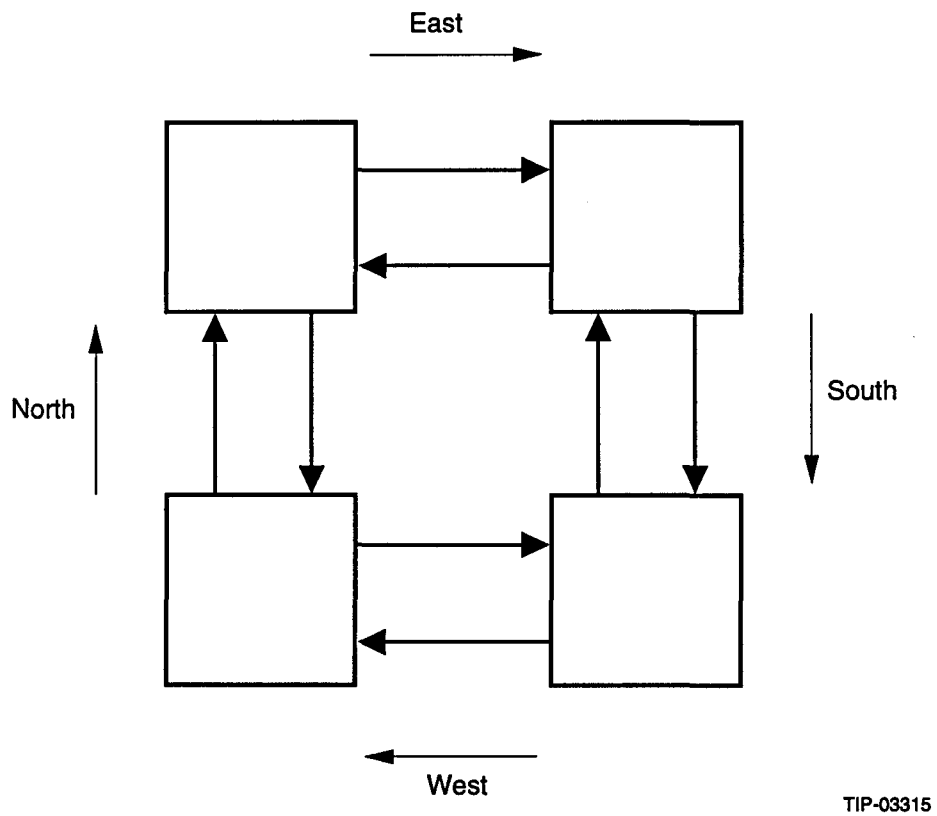

Figure 6.1. Communication Path for North, South, East, and West Communication in the Square Geometry.

The grid is decomposed in the following manner. First the number of nodes is determined in the program. The dimension of the nodes used determines the number of cells in the x direction and the z direction in Cartesian coordinates. The dimension n is defined as $nodes = 2^n$ where $nodes$ is the number of nodes used. The number of blocks in the respective directions is

$$r = n_x/(n_x + n_z) \tag{6.36}$$

$$(nb)_x = 2^{n \times r} \tag{6.37}$$

$$(nb)_z = 2^{n-n \times r}, \tag{6.38}$$

where n_x and n_z are the size of the total grid in the x and z directions, respectively, and $(nb)_x$ and $(nb)_z$ are the number of blocks in the x and z directions, respectively. The number of cells per node is

$$nxm = n_x/(nb)_x \tag{6.39}$$

$$nzm = n_z/(nb)_z\,. \tag{6.40}$$

Nodes north, south, east, and west of a particular node are calculated in the following manner:

$$ix = menod/(nb)_z + 1 \tag{6.41}$$

$$iz = (menod + 1) - (ix - 1) * (nb)_z \tag{6.42}$$

$$izp = iz + 1 \tag{6.43}$$

$$izm = iz - 1 \tag{6.44}$$

$$ixp = ix + 1 \tag{6.45}$$

$$ixm = ix - 1 \tag{6.46}$$

$$North = (ix - 1) * (nb)_z + izp - 1 \tag{6.47}$$

$$South = (ix - 1) * (nb)_z + izm - 1 \tag{6.48}$$

$$East = (ixp - 1) * (nb)_z + iz - 1 \tag{6.49}$$

$$West = (ixm - 1) * (nb)_z + iz - 1\,, \tag{6.50}$$

where *menod* is the node number of the specific node and *North*, *South*, *East*, and *West* are the node numbers of the north, south, east, and west nodes, respectively.

The quantities that are transferred between nodes are fields, currents, and distribution functions. They update the boundary cells of each square block assigned to each node. This update is done at every time step. The dominant data transfer is done with the distribution function. The boundaries need to be updated at both the x and z boundaries in Cartesian coordinates or at the r and z boundaries in cylindrical coordinates. Therefore, in the square decomposition scheme the distribution function is transferred twice.

Boundary conditions are handled in the transfer of the data to the respective boundary cells. In the case of Cartesian coordinates, periodic boundary conditions are imposed on all quantities. Blocks at either end of the grid transfer data in a wraparound fashion. Blocks at the west end transfer data to the east blocks, and blocks at the east end transfer data

to blocks at the west end. A similar situation occurs for blocks at the north and south ends. In the case of cylindrical coordinates, the north and south block data are handled in the same manner since the boundary conditions are periodic in this direction. Blocks at the east end have all quantities at their eastern boundaries set equal to 0, which takes into account the conducting wall boundary conditions there. The western blocks are at the $r = 0$ boundary. The west end of these blocks handles the fields, distribution function, and currents as described in Section 6.2.1.

6.3 Particle-in-Cell Codes

In this section collider models using Particle-in-Cell (PIC) codes are described. In these models the collider is broken into two sections; one section models the interaction region, and the other models the rest of the storage ring. In the interaction region it is necessary to take into account the beam-beam interaction. Since self-consistent effects play an important role in the beam dynamics there, PIC codes are used. The rest of the collider is modelled using the Courant-Synder map, which simply involves a symplectic rotation of the particles in phase space.[5]

Two types of PIC codes are used to model the beam-beam interaction region: a fully electromagnetic code and a strong-strong code. The strong-strong code uses the "strong-strong" model described in Section 3.0. Our model differs from previous models of the beam-beam interaction.[26–28,42] Previous models as described in Section 5.0 approximated the beam-beam interaction as either a two-particle interaction, a single-particle–many-particle interaction ("weak-strong" approximation),[27,42] or a many-particle–many-particle interaction ("strong-strong"), where the beam is constrained to be a Gaussian.[26,28] Using a PIC code in the beam-beam model allows a many-particle–many-particle interaction with internal degrees of freedom in the beam shapes.

The steps of the simulation for one turn in the collider are:

1. interaction region
2. reset of fields to 0
3. symplectic mapping.

These steps are repeated until the necessary number of turns is attained. Figure 6.2 shows the basic geometry used in the simulation models.

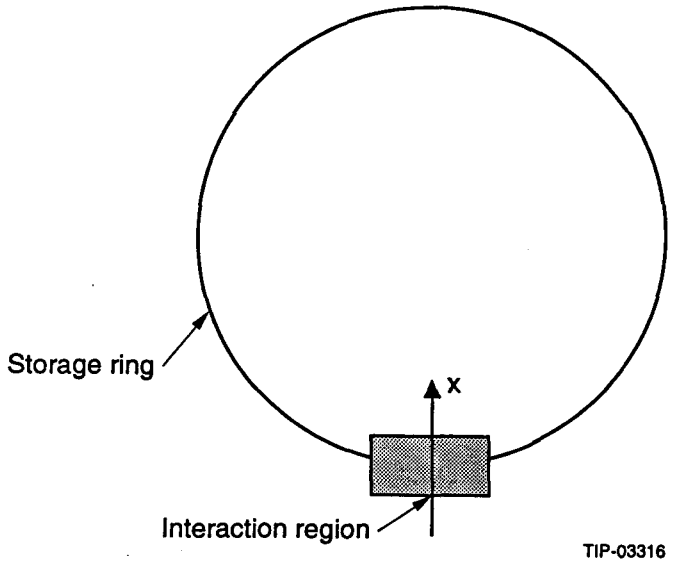

Figure 6.2. The Two Components Used to Model the Collider.

6.3.1 Accelerator Model

The model we use for the accelerator is shown in Figure 6.2. Outside of the interaction region self-consistent effects are not as important as in the interaction region, since the density of the beams is much lower. Therefore, the approximation of single-particle dynamics is a very good one. With this approximation a linear map can represent the collider in matrix notation:

$$\begin{pmatrix} x \\ x' \end{pmatrix}_{n+1} = \begin{pmatrix} 1 & -\Delta s \\ 0 & 1 \end{pmatrix} \begin{pmatrix} \cos(2\pi\nu_0) & \beta_0^* \sin(2\pi\nu_0) \\ -\frac{1}{\beta_0^*}\sin(2\pi\nu_0) & \cos(2\pi\nu_0) \end{pmatrix} \begin{pmatrix} x \\ x' \end{pmatrix}_n , \tag{6.51}$$

where Δs is the drift length along the collider path. The first matrix accounts for the finite length of the interaction region by treating the region as a free drift space and subtracting it from the full rotation. The second matrix is the Courant-Synder map around the collider, where $\nu_0 = \oint ds/\beta(s)$ is the unperturbed tune and $\alpha = 0$ everywhere in the ring.[5]

6.3.2 Electromagnetic Code

A 1-2/2 dimensional (x, p_x, p_y, p_z) relativistic electromagnetic PIC code is used to model the interaction region.[36,37] The main purpose of this code is to determine the electromagnetic effects on the beams. Detailed descriptions of this type of code can be found elsewhere.[36,37] The particular modifications made to this code to study the beam-beam interaction will be described in this section.

Typically, fully electromagnetic codes solve the full set of Maxwell's Eq. (6.7). The main constraint on these types of codes is the time step size Δt, which needs to be small enough to follow light waves for numerical stability:[36,37]

$$c\Delta t < \Delta\,, \tag{6.52}$$

where c is the speed of light and Δ is the grid size of the simulation. Because of the small time step size, the number of time steps to follow particles in the interaction region is prohibitively large for SSC parameters. For realistic SSC parameters the simulation time step size Δt is about $3 \times 10^{-5}\tau_{int}$, where τ_{int} is the interaction time. So 30,000 time steps would be necessary for one interaction. To reduce this constraint, the energy of the beams can be reduced. When SSC parameters are relaxed to reduce the number of time steps, the electrostatic field begins to dominate, causing the beams to spread too quickly. In order to eliminate this spreading, the electrostatic field in Eq. (6.7) is ignored. The main purpose of this code is to examine the effects of the transverse fields on the beam-beam interaction at high beam energies, where the electrostatic fields causing beam spread are small. Therefore, the approximation is justified.

6.3.3 Strong-Strong Code

The shortcoming of the fully self-consistent electromagnetic treatment described in the previous section is the time step size. Since light waves are followed in this code, a large number of time steps is needed to maintain numerical stability. To eliminate this, a strong-strong code is developed. The code has one spatial dimension x and three velocity coordinates (v_x, v_y, v_z). In this strong-strong code two approximations are made: (1) light waves are ignored and (2) self fields (space charge effects) among particles of the same beam are ignored. Ignoring the effects of light waves can be justified for the SSC by considering the collisionless skin depth, λ_c, of the beam, where

$$\lambda_c = \frac{c}{\omega_b} \tag{6.53}$$

$$\omega_b = \sqrt{\frac{4\pi e^2 n_b}{\gamma m_b}}\,. \tag{6.54}$$

Using parameters for the SSC, $\lambda_c \gg w$, where w is the width of the beam and λ_c is the scale length over which a plasma responds to light waves. Since λ_c is much larger than the size of the beam, particles do not strongly interact with light waves. Self fields of the beam are neglected, since the forces from the other beam are much larger. The ratio of the self fields to the kick fields from the other beam is

$$(\text{self fields}) \approx \frac{1}{\gamma^2}(\text{kick fields}), \tag{6.55}$$

where $\gamma = 2.13 \times 10^4$ for SSC parameters.

With the elimination of light waves the time step of the simulations can be on the order of the plasma frequency ω_p, which occurs on a much longer time scale than light waves. The time of interaction between the two beams is $\tau_{int} = \Delta s/2c$, where τ_{int} is the time the simulation is run before the particles are rotated in phase space. With simulation time steps in units of fractions of ω_p, the time period can now be represented by 1–4 simulation time steps.

In particle simulations the beams are represented by a number of macroparticles. Each particle in the simulation has a particle shape factor $S(x)$. $S(x)$ is chosen to give the particles finite size, so that short wavelength oscillations are filtered out in the fields.[36,37] This reduces noise and short-range collision forces. The particular form chosen is

$$S(x) = \frac{1}{\sqrt{2\pi}a} \exp\left(-\frac{x^2}{2a^2}\right), \tag{6.56}$$

where a is the finite particle size.

Care must be taken when choosing the particle size a. When it becomes comparable to the beam width w, the tune shift $\Delta\nu$ is reduced . This can be expressed by

$$\frac{\Delta\nu_{point}}{\Delta\nu_{fsp}} = \left(1 + 4\left(\frac{a}{w}\right)^2\right)^{1/2}, \tag{6.57}$$

where $\Delta\nu_{point}$ is the tune shift for a point particle, $\Delta\nu_{fsp}$ is the tune shift for a finite size particle, a is the particle size, and w is the beam width. This calculation is based on the assumption that the particle is Gaussian in shape, as in Eq. (6.56). The particle size must be chosen so that $a << w$ and, therefore,

$$\frac{\Delta\nu_{point}}{\Delta\nu_{fsp}} \approx 1. \tag{6.58}$$

The macroparticles are advanced by the Lorentz force equation:

$$\frac{d\vec{p}_i}{dt} = e\int_{-\infty}^{\infty} dx S(x - x_i)(\vec{E}(\vec{x}) + \vec{v}_i \times \vec{B}(\vec{x})/c), \tag{6.59}$$

where $\vec{x}_i$ is the position, $\vec{p}_i$ is the momentum, $\vec{v}_i$ is the velocity of particle i, $S(x)$ is the particle shape factor, and $\vec{E}(\vec{x}_i)$ and $\vec{B}(\vec{x}_i)$ are the electric and magnetic field of the other beam, respectively. The integral over x takes into account the finite size of the particle.

The calculation of the fields can be simplified by performing the appropriate Lorentz transforms and taking into account the highly relativistic nature of the beams being studied. For a general Lorentz transformation to a frame moving at velocity $\vec{v}$, the transformation of the fields can be written:[43]

$$\vec{E} = \gamma(\vec{E}' + \vec{\beta} \times \vec{B}') - \frac{\gamma^2}{\gamma+1}\vec{\beta}(\vec{\beta} \cdot \vec{E}'), \tag{6.60}$$

$$\vec{B} = \gamma(\vec{B}' - \vec{\beta} \times \vec{E}') - \frac{\gamma^2}{\gamma+1}\vec{\beta}(\vec{\beta} \cdot \vec{B}'), \tag{6.61}$$

where $\vec{\beta} = \vec{v}/c$ and γ is the relativistic factor. Eqs. (6.60) and (6.61) can represent transformations of the fields from the frame moving with the beam $(\vec{E}', \vec{B}')$ to the lab frame $(\vec{E}, \vec{B})$. In the beam frame the beam particles have only thermal velocities. These velocities are small and randomly oriented. Therefore, only small remnant currents are present, and the approximation $|\vec{B}'| \approx 0$ can be made. Eqs. (6.60) and (6.61) become

$$\vec{E} = \gamma\vec{E}' - \frac{\gamma^2}{\gamma+1}\vec{\beta}(\vec{\beta} \cdot \vec{E}'), \tag{6.62}$$

$$\vec{B} = -\gamma(\vec{\beta} \times \vec{E}'). \tag{6.63}$$

Assuming the motion of the beams is in the z direction, the fields can be written:

$$E_x = \gamma E'_x, \tag{6.64}$$

$$B_y = \gamma\beta E'_x. \tag{6.65}$$

Since the beams are highly relativistic ($\gamma \gg 1$), the approximation $|\vec{\beta}| \approx 1$ can be made. Thus, $E_x \approx B_y$. Using this in Eq. (6.59), we obtain

$$\frac{d\vec{p}_i}{dt} \approx e\int_{-\infty}^{\infty} dx S(x - x_i) E_x(x)(1 + v_i/c), \tag{6.66}$$

where v_i is the velocity of the beam kicked by the other beam. Again the approximation $v_i \approx c$ can be used:

$$\frac{d\vec{p}_i}{dt} \approx 2e\int_{-\infty}^{\infty} dx S(x - x_i) E_x(x). \tag{6.67}$$

Therefore, including the effects of the magnetic field kick to the beam simply involves doubling the contribution of the electrostatic field of the other beam.

The electric field E_x is calculated from

$$\frac{\partial E_x}{\partial x} = 4\pi e \int S(x - x')\rho(x')dx' , \tag{6.68}$$

where $\rho(x)$ is the charge density and $S(x)$ is the particle shape factor. The charge density $\rho(x)$ is the accumulation of the finite size macroparticles:

$$\rho(x) = \sum_{j=1}^{N} q_j S(x - x_j) , \tag{6.69}$$

where N is the number of particles and q_j is the charge of particle j. Since the charge is accumulated on a grid, Fast Fourier Transforms (FFT) can be used to transform the grid to k space, where manipulation is easier:

$$\rho(x) = \sum_{j=1}^{N} q_j e^{-(x-x_j)^2/2a^2} , \tag{6.70}$$

$$\rho(k) = q e^{-k^2a^2/2} \sum_g e^{-ikx_g} \sum_{j \in g} e^{-ik\delta_j} , \tag{6.71}$$

where a Gaussian shape factor is used $S(x - x_j) = \exp[-(x - x_j)^2/2a^2]$, the sum on g is over the grid points, a is the particle size, and δ_j is the distance of the particle from the nearest grid point $x_j - x_g$. The summation term with $j \in g$ is a sum over all particles j in grid cell g.

In order to increase the accuracy, the accumulation is done using cubic spline interpolation.[37,44] This assignment technique allows a smoother grid assignment than lower-order methods such as the subtracted-dipole scheme (SUDS) or area-weighting scheme.[36,37] The charge density then takes the form:[37]

$$\rho(k) = q e^{-k^2a^2/2} \left[\sum_g e^{-ikx_g} \left(\sum_{j \in g} s_1 + \sum_{j \in g-1} s_2 \right) - ik \sum_g e^{-ikx_g} \left(\sum_{j \in g} s_3 + \sum_{j \in g-1} s_4 \right) \right] , \tag{6.72}$$

where the summation terms with $j \in g - 1$ are sums over all particles j in grid cell $g - 1$, and the s terms are the weighting factors:

$$s_1 = (1 - \delta_j)^2(1 + 2\delta_j) \tag{6.73}$$

$$s_2 = \delta_j^2(3 - 2\delta_j) \tag{6.74}$$

$$s_3 = \delta_j(1 - \delta_j)^2\Delta \tag{6.75}$$

$$s_4 = -(1-\delta_j)\delta_j^2\Delta\,. \tag{6.76}$$

The electric field in Eq. (6.68) can be transformed to k space using the FFT:

$$-ikE_x = 4\pi e\rho(k)\,, \tag{6.77}$$

where $\rho(k)$ is from Eq. (6.72). Using Eq. (6.72) and rearranging terms,[37] we obtain

$$E_x(k) = \frac{iqe^{-k^2a^2/2}}{k}[\mathrm{FFT(G1X)} - ik\mathrm{FFT(G2X)}]\,, \tag{6.78}$$

where FFT is the Fast Fourier Transform and

$$\mathrm{G1X} = \sum_{j\in g} s_1 + \sum_{j\in g-1} s_2 \tag{6.79}$$

$$\mathrm{G2X} = \sum_{j\in g} s_3 + \sum_{j\in g-1} s_4\,, \tag{6.80}$$

where G2X corresponds to derivatives of the charge density. Note that two quantities, G1X and G2X, need to be accumulated in this method. The force on the particles $F(x)$ can be calculated in a similar manner:[37]

$$F(x) = qE(x) \tag{6.81}$$

$$= s_1(\delta)F_s(x_g) + s_2(\delta)F_s(x_g+\Delta) + s_3(\delta)F_d(x_g) + s_4(\delta)F_d(x_g+\Delta)\,, \tag{6.82}$$

where δ is the distance from the nearest grid point $x - x_g$, and

$$F_s = \frac{q}{2\pi L}\mathrm{FFT}^{-1}[e^{-k^2a^2/2}E(k)]\,, \tag{6.83}$$

$$F_d = \frac{q}{2\pi L}\mathrm{FFT}^{-1}[ike^{-k^2a^2/2}E(k)]\,, \tag{6.84}$$

where L is the system length and FFT^{-1} is the inverse transform.

The previous field calculation solves the field for periodic boundary conditions. Note that the field equation does not take into account finite charge in the system. Finite charge is included in the $k = 0$ term. However, this term cannot be incorporated, because we would be dividing by 0. To account for finite charge in the system, the $k = 0$ term in E_x can be explicitly calculated:[45]

$$E_x^{k=0}(x) = -4\pi\rho(0)\left(\frac{L_x}{2} - x\right)\,, \tag{6.85}$$

where L_x is the length of the system and $\rho(0)$ is the $k = 0$ component of the charge density that calculates the total charge in the system. By adding this field to the field calculated from Eq. (6.78), one obtains the field with vacuum boundary conditions.

In the SSC design each beam has $\sim 10^{10}$ particles and a large number of beam-beam interactions (10^8). Due to computer time limitations the beams may be represented only by $\sim 10^3$–10^4 particles. We find that the representation of Eqs. (6.68) and (6.59) by the well known PIC method[36,37] with macroparticles shows a large amount of noise due to the small number of computational macroparticles. This is especially apparent when single-particle diffusion is studied. To study particle diffusion, therefore, we implemented a few improved algorithms for noise reduction. One is the cubic spline for smoother interpolation,[37] which was described above. Another is the loading of the macroparticles using a quiet start.[36] The third is to follow the portion of the particles due to the perturbed distribution only.[37,46,47] This is described in the next section.

Normally simulation macroparticles are distributed initially in a Gaussian profile via random number generators. A distribution produced from this method is shown in Figure 6.3. The distribution integrated over p_x is shown in Figure 6.4. Although the distribution resembles a Gaussian, it contains spikes and peaks that produce start-up noise.

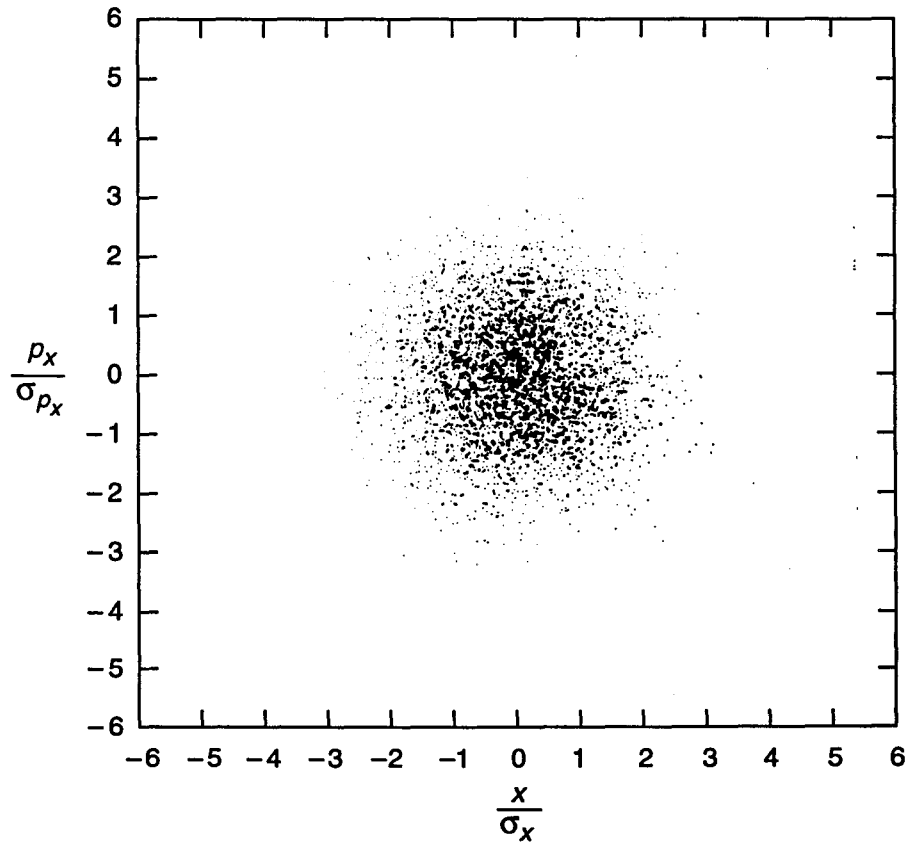

Figure 6.3. A Gaussian Distribution of Particles Produced from a Random Number Generator.

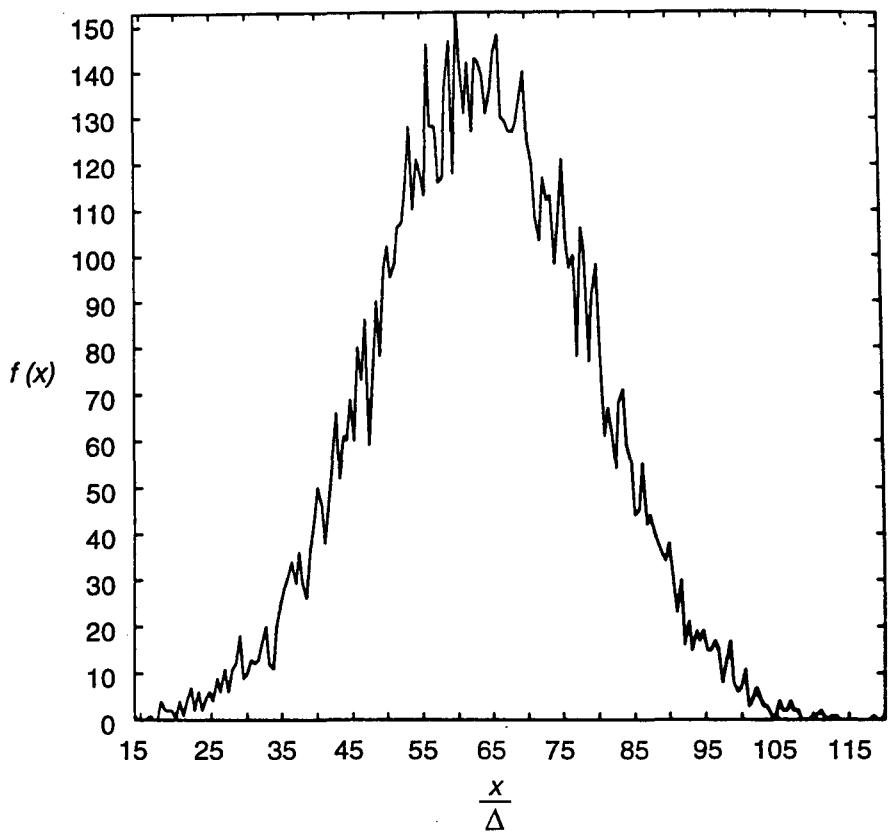

Figure 6.4. Distribution Integrated over p_x with Random Number-Generated Phase Space Positions.

This start-up noise can be minimized by using the technique of the quiet start to load the macroparticles.[36] Two methods of loading simulation macroparticles are described. One method distributes the particles uniformly in phase space and assigns charge nonuniformly to the particles based on the initial particle distribution. The other method involves nonuniform distribution of the particles in phase space and uniform charge for each particle.

In the first method the particles are distributed uniformly in r and θ, where r and θ are defined in terms of x and p_x as

$$r^2 = \frac{x}{\beta_0^*}^2 + \frac{p_x}{p}^2 \tag{6.86}$$

$$\tan(\theta) = \frac{x}{\beta_0^*}\frac{p}{p_x}, \tag{6.87}$$

where β_0^* is the betatron oscillation length at the interaction point and p is the particle momentum along the collider. The increments in r and θ are determined from values input into the code. The r increment Δr is r_{max}/n_r, where r_{max} is the maximum value of r, and n_r is the number of r segments. The angle increment $\Delta\theta$ is $2\pi/n_\theta$, where n_θ is the number

of angle segments. The initial distribution for 10,000 particles is shown in Figure 6.5. We assume a Gaussian profile for the beam in $x - p_x$ of the form

$$f(x, p_x) = \frac{N}{2\pi\sigma_x\sigma_{p_x}} \exp\left(-\frac{x^2}{2\sigma_x^2} - \frac{p_x^2}{2\sigma_{p_x}^2}\right). \tag{6.88}$$

Each particle can be assigned charge q_i:

$$q_i = Ne\frac{r_i \exp\left(-\frac{r_i^2}{2\sigma^2}\right)}{\sum_{i=1}^{N} r_i \exp\left(-\frac{r_i^2}{2\sigma^2}\right)}, \tag{6.89}$$

where N is the number of simulation particles, e is the unit charge, r_i is obtained from Eq. (6.86) for particle i, and σ is σ_x. Although each particle is assigned a different charge q_i, each particle is also assigned a different mass m_i, so that the force on each particle is the same.

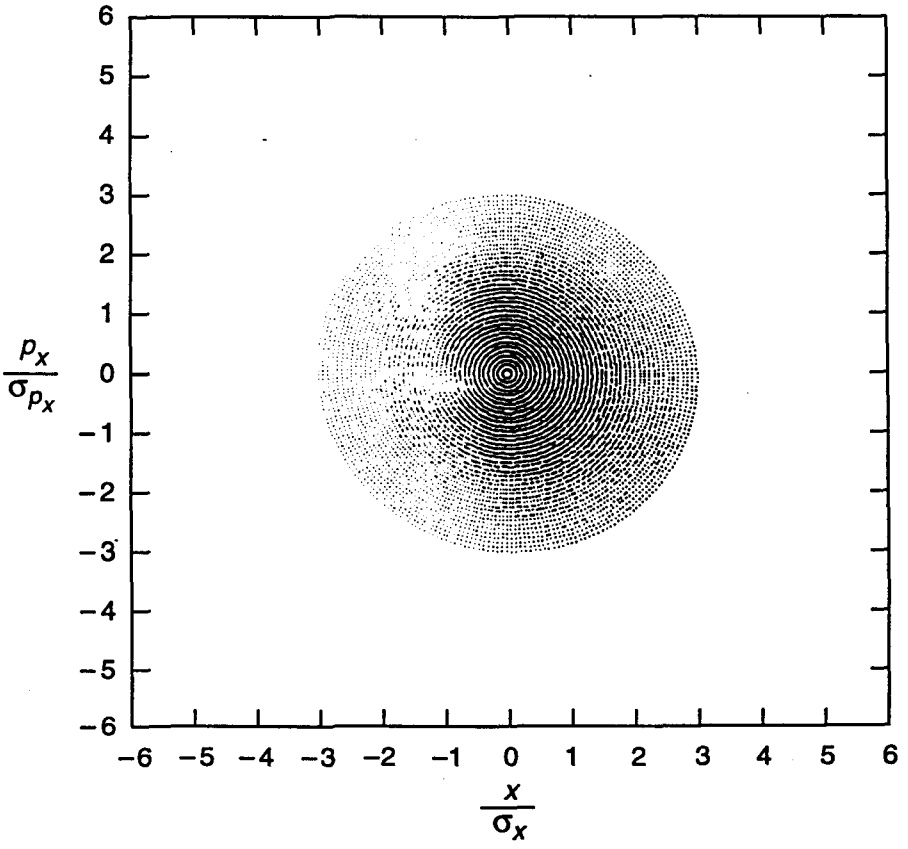

Figure 6.5. Uniform Distribution of 10,000 Particles in x, p_x Phase Space.

The distribution integrated over p_x after the charge assignment is shown in Figure 6.6. In comparison with the random distribution (Figure 6.4), this distribution is much smoother in the tails and is more symmetric about the center. This symmetry reduces the higher-order moments in the distribution and, therefore, produces less start-up noise.

In the second quiet start method, particles are distributed nonuniformly in r and θ, where r and θ are defined in terms of x and p_x in Eqs. (6.86) and (6.87).[48] The number of particles at each r value is determined by a cumulative integration method.[36,37] Again a Gaussian distribution $f(x, p_x)$ in x and p_x is assumed (Eq. (6.88)). This function can be integrated in r and θ coordinates to yield

$$N(r) = N\left[1 - \exp\left(-\frac{r^2}{2\sigma_r^2}\right)\right], \tag{6.90}$$

where $N(r)$ is the number of particles contained within radius r and N is the total number of simulation particles. Eq. (6.90) can be used to obtain the number of particles to add between r and $r + \Delta r$:

$$\Delta N = N\left[\exp\left(\frac{r^2}{2\sigma_r^2}\right) - \exp\left(\frac{(r+\Delta r)^2}{2\sigma_r^2}\right)\right], \tag{6.91}$$

where ΔN is the number of particles to be added. The ΔN particles between r and $r + \Delta r$ are distributed uniformly in θ, with a random offset θ_{ran} at $r + \Delta r/2$. The initial distribution for 10,000 particles is shown in Figure 6.7. The distribution integrated over p_x is shown in Figure 6.8. This distribution is smoother than both the random distribution of particles (Figure 6.4) and the uniform distribution of differently charged particles (Figure 6.6).

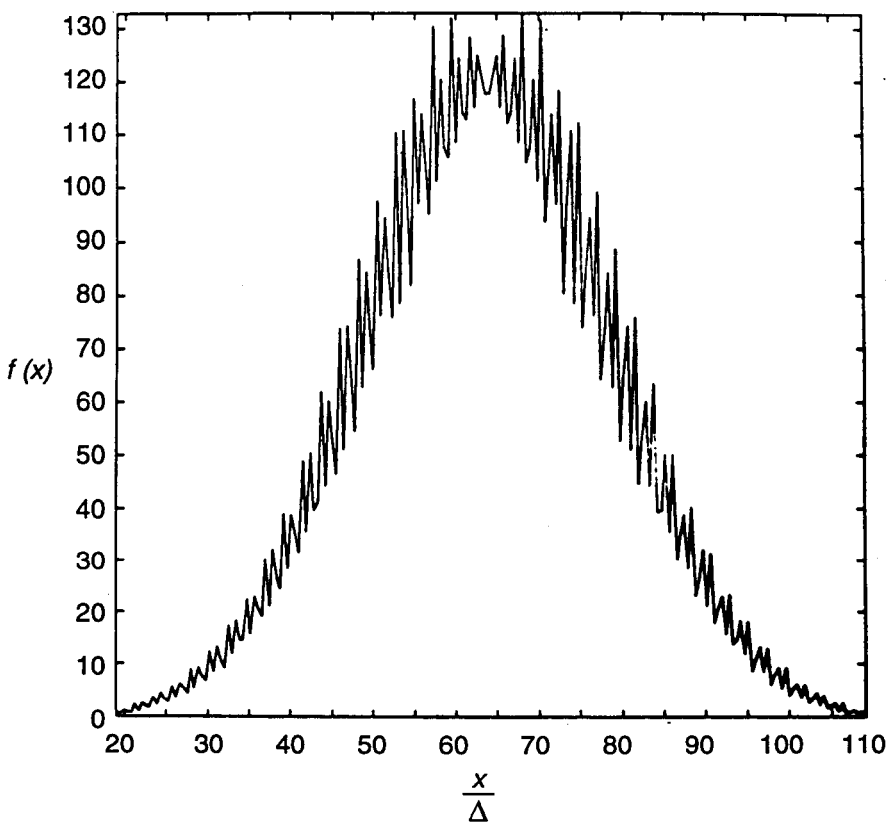

Figure 6.6. Distribution Integrated over p_x with Uniform Distribution and Nonuniform Charge Assignment.

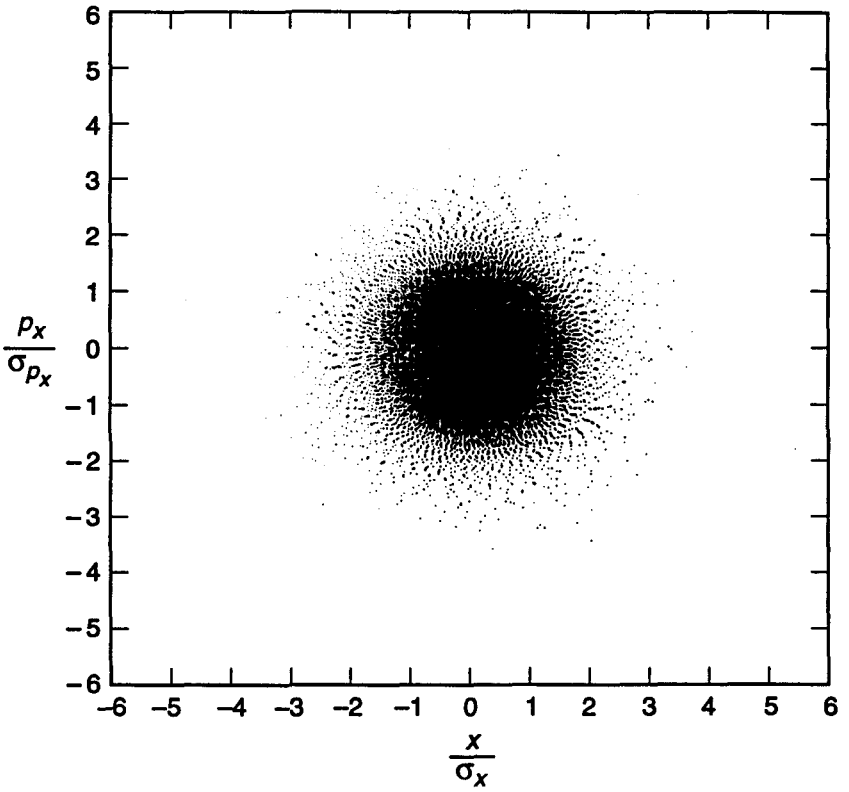

Figure 6.7. A Nonuniform Distribution of 10,000 Particles with Equal Charge.

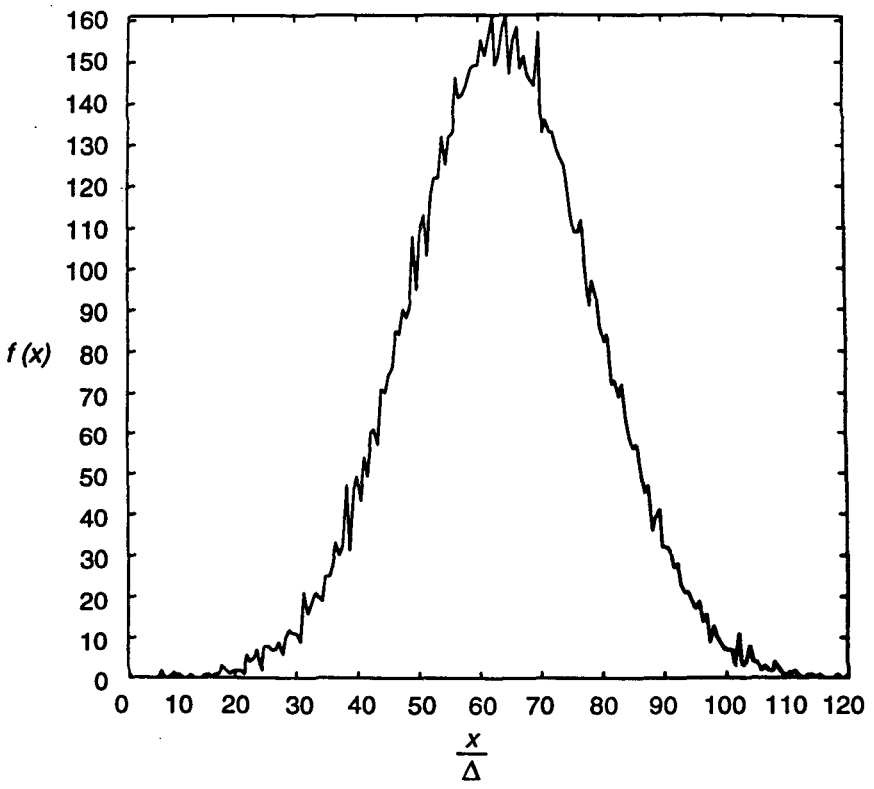

Figure 6.8. The Profile in x of a Nonuniform Distribution of Particles.

6.3.4 Noisy Model

In order to study particle diffusion brought about by the beam-beam interaction, sources of numerical noise in the PIC codes need to be quantified. One source of noise is the fluctuations due to the use of a finite number of particles. To model this noise in PIC simulations, noise is added to the tracking code described in Section 6.1. This is done by adding a fluctuation term to the tune shift $\Delta\nu_0$:

$$\Delta\nu = \Delta\nu_0(1 + R\, n(x)), \tag{6.92}$$

$$n(x) = \frac{1}{\sqrt{N(x)}}, \tag{6.93}$$

where $N(x)$ is the number of particles contained between $-x$ and $+x$, and R is a random number between -1 and 1. $n(x)$ gives an idea of the fluctuation level:

$$N(x) = N \operatorname{erf}\left(\frac{x}{\sqrt{2}\sigma_x}\right), \tag{6.94}$$

where N is the total number of particles. Eq. (6.94) is calculated for a Gaussian distribution of particles.

6.4 δf Algorithm

PIC codes typically use macroparticles to represent the entire distribution of particles. In the beam-beam interaction for the SSC, the beams consist of 10^{10} particles each. Simulating this many particles with the PIC technique is computationally prohibitive. With the conventional PIC code 10^{10} particles are represented by only 10^3–10^4 simulation particles, allowing simulation of the beam-beam interaction in a reasonable computation time. However, the fluctuation level of various quantities such as the beam density ρ in the code is much higher than that of the real beam. The fluctuation level $\delta\rho$ is described approximately as

$$\frac{\delta\rho}{\rho} \approx \frac{\sqrt{N}}{N}, \tag{6.95}$$

where N is the number of particles. Therefore, the fluctuation level of the PIC code is about 10^3 times higher than that of the real beam. Although this probably is not significant for beam blowup near resonances, the higher fluctuation level has a large effect on more subtle phenomena such as particle diffusion. To facilitate the study of subtle effects, a δf code has been developed.[37,46,47,49]

The δf method follows only the fluctuating part of the distribution instead of the entire distribution. This is essentially modelling the numerator on the right-hand side

of Eq. (6.95), which goes as $\sqrt{N}$. So the 10^3–10^4 computational particles are used to represent $\sqrt{10^{10}}$ or 10^5 real fluctuation particles. This is only one or two orders of magnitude beyond the number of computer particles.

In the previous sections the strong-strong code used a finite number of particles to represent the Vlasov equation or Klimontovich equation.[50] In the particular case of the beam-beam interaction,

$$\frac{\partial f}{\partial s} + x'\frac{\partial f}{\partial x} - \big(K(s)x - F(x,s)\big)\frac{\partial f}{\partial x'} = 0\,, \tag{6.96}$$

where $K(s)x$ is the usual magnetic guiding force and $F(x,s)$ is the beam-beam force

$$F(x,s) = \frac{2eE_x(x)}{\gamma m v^2}\delta_p(s)\,, \tag{6.97}$$

where $E_x(x)$ is calculated from the distribution of the particles, and $\delta_p(s)$ is the periodic δ-function. $\delta_p(s) = 1$ when $s = nL$, where L is the accelerator circumference and $n = 0, 1, \ldots$. The distribution function f is represented by a finite number of particles by

$$f(x,x',s) = \sum_{i=1}^{N} \delta\big(x - x_i(s)\big)\delta\big(x' - x_i'(s)\big)\,, \tag{6.98}$$

where N is the number of simulation particles used.

In the δf method only the perturbative part of the distribution is followed.[37,46,47] The total distribution function $f(x,x',s)$ is decomposed into

$$f(x,x',s) = f_0(x,x',s) + \delta f(x,x',s)\,, \tag{6.99}$$

where $f_0(x,x',s)$ is the steady or slowly varying part of the distribution and $\delta f(x,x',s)$ is the perturbative part. The key to this method is finding a distribution $f_0(x,x',s)$ that is close to the total distribution $f(x,x',s)$. The perturbative part $\delta f(x,x',s)$ is then small, causing only small changes to the distribution, and thus representing only the fluctuation levels. If a distribution $f_0(x,x',s)$ close to the total distribution is not found, then $\delta f(x,x',s)$ represents more than the fluctuating part of the total distribution. This defeats the purpose of the method. The ideal situation is for $f_0(x,x',s)$ to have an analytic solution. In this case any numerical truncation errors that result from the necessary derivatives of this function are eliminated. If an analytic solution cannot be found, then a numerical solution needs to be found that is close to the total distribution $f(x,x',s)$ and is slowly varying. Continual numerical update of $f_0(x,x',s)$ would also defeat the purpose of the δf method, since the PIC technique essentially does this also.

In the particular case of the beam-beam interaction, an analytic solution to an equation close to the original Vlasov equation can be found. In the case of a linearized beam-beam force, the Vlasov equation can be written in the form:

$$\frac{\partial f_0}{\partial s} + x'\frac{\partial f_0}{\partial x} - (K(s) - F_0(s))x\frac{\partial f_0}{\partial x'} = 0\,, \tag{6.100}$$

where

$$F_0(s) = F_0\delta_p(s)\,. \tag{6.101}$$

F_0 is the linear portion of the beam-beam force $F(x)$. The solution is a Gaussian of the form:

$$f_0(r) = \frac{N\beta^*}{2\pi\sigma^2}\exp\left(-\frac{r^2}{2\sigma^2}\right), \tag{6.102}$$

where $r^2 = x^2 + \beta^{*2}x'^2$, N is the total number of particles in the beam, β^* is the betatron oscillation length, and σ is in the x direction. Note that if the beam-beam force were linear, this solution $f_0(r)$ would represent the distribution for all time in the interaction region as well as in the rest of the storage ring. Only the values of β^* and σ differ between the two regions. In the interaction region the β^* and σ are calculated using the dynamic β model, which assumes a linear beam-beam force:[10,51]

$$\cos(2\pi\nu) = \cos(2\pi\nu_0) + 2\pi\Delta\nu\sin(2\pi\nu_0)\,, \tag{6.103}$$

$$\frac{\beta^*}{\beta_0^*} = \frac{\sin(2\pi\nu_0)}{\sin(2\pi\nu)}\,, \tag{6.104}$$

where ν_0 and β_0^* are the unperturbed quantities valid in the rest of the storage ring, and ν and β^* are the quantities perturbed by the linearized beam-beam force. From the perturbed β^* the perturbed beam width σ can be calculated from the formula:

$$\frac{\beta_0^*}{\beta^*} = \frac{\sigma_0^2}{\sigma^2}\,, \tag{6.105}$$

where σ_0 is the unperturbed beam width that is obtained from the assumption that the beam emittance is unchanged due to this linear beam-beam force. An equation for the perturbed β^* can be written in terms of unperturbed quantities from Eqs. (6.103) and (6.104):

$$\left(\frac{\beta^*}{\beta_0^*}\right)^2 - 4\pi\Delta\nu_0\cot(2\pi\nu_0)\left(\frac{\beta^*}{\beta_0^*}\right)^{3/2} - (2\pi\Delta\nu_0)^2\left(\frac{\beta^*}{\beta_0^*}\right) - 1 = 0\,, \tag{6.106}$$

where $\Delta\nu_0$ is the unperturbed, one-dimensional tune shift. Eq. (6.106) can be expressed in terms of the perturbed σ using Eq. (6.105):

$$\left(\frac{\sigma}{\sigma_0}\right)^4 - 4\pi\Delta\nu_0\cot(2\pi\nu_0)\left(\frac{\sigma}{\sigma_0}\right)^3 - (2\pi\Delta\nu_0)^2\left(\frac{\sigma}{\sigma_0}\right)^2 - 1 = 0\,. \tag{6.107}$$

Both equations can be solved for the perturbed σ or β^* using a root finder. Once this is obtained the other perturbed quantities, ν and $\Delta\nu$, are obtained from Eqs. (6.103) and (6.104).

Subtracting the linearized equation in Eq. (6.100) from the total Vlasov equation in Eq. (6.96), we obtain the perturbative part of Eq. (6.96) for δf:

$$\frac{\partial \delta f}{\partial s} + x' \frac{\partial \delta f}{\partial x} - \big(K(s)x - F_0(x,s)\big)\frac{\partial \delta f}{\partial x'} = -\big(F(x,s) - F_0(s)x\big)\frac{\partial f_0}{\partial x'} . \tag{6.108}$$

$F_0(x,s)$ is the kick from a Gaussian beam, and $F(x,s)$ is the kick from a Gaussian beam $F_0(x,s)$ plus the perturbation $\delta F(x,s)$. As a result of using the dynamic beta model for the stationary solution f_0, only the nonlinear part of the beam-beam force on the right-hand side of Eq. (6.108) is used to advance δf. The terms $\frac{\partial f_0}{\partial x'}$ and $F_0(x,s)$ are calculated using the perturbed dynamic beta quantities β^* and σ. Note that the unperturbed Gaussian field $F_0(x,s)$ is used on the left-hand side of Eq. (6.108), which makes the equation linear in δf. The term that has been neglected is

$$\delta F(x,s)\frac{\partial \delta f}{\partial x'} . \tag{6.109}$$

This term can be shown to be small in our problem. A possible incorporation of this term in the algorithm is described in Section 8.0. The reason for choosing the particular form of the steady-state solution is apparent. It is chosen so that the right-hand side of Eq. (6.108) is small.

6.4.1 Finite Particle Representation

The perturbative part of the distribution δf (Eq. (6.108)) can be represented by a finite number of particles (characteristics):

$$\delta f(x,x',s) = \sum_{i=1}^{N} w_i\big[s, x_i(s), x_i'(s)\big]\,\delta\big(x - x_i(s)\big)\,\delta\big(x' - x_i'(s)\big) . \tag{6.110}$$

Substituting this into the equation for δf advance, we obtain

$$\frac{dw_i}{ds} = -\frac{1}{n}\left[\big(F(x,s) - F_0(s)x\big)\frac{\partial f_0}{\partial x'}\right]_i , \tag{6.111}$$

where

$$n = \left(\frac{N_c}{\Delta x \Delta x'} \right). \tag{6.112}$$

This density n is calculated on the assumption that the particles are distributed uniformly in phase space. The density n is assumed constant through the entire run. This approximation is no longer valid when there is either significant clumping of particles or the particles have spread out in phase space. Thus, the δf algorithm is most suited to problems that occur far away from resonances.

In the δf algorithm x_i, x_i', and w_i are advanced. The advance of the extra term w_i increases the number of operations over the PIC method and leads to other numerical constraints that will be described in the next section.

The simulation particles are distributed evenly in phase space upon initialization. The particles are distributed uniformly in x and p_x phase space in a cylindrical coordinate system r and θ. r and θ are defined in terms of x and p_x:

$$r^2 = \frac{x}{\beta_0^*}^2 + \frac{p_x}{p}^2, \tag{6.113}$$

$$\tan(\theta) = \frac{x}{\beta_0^*} \frac{p}{p_x}, \tag{6.114}$$

where β_0^* is the betatron oscillation length at the interaction point and p is the particle momentum along the collider in s. The maximum r value is input into the code and is broken up into segments of length Δr. The number of particles at each r value is determined by a cumulative integration method.[37] The particular functional form is

$$\Delta N = \frac{N}{N_r^2}(2r - 1), \tag{6.115}$$

where ΔN is the number of particles to be added, N is the number of particles, and N_r is the number of Δr segments to the edge of the distribution. Once the number of particles between r and $r+\Delta r$ is known, they are distributed uniformly in θ with a random offset θ_{ran} at $r + \Delta r/2$. The initial distribution for 1000 particles is shown in Figure 6.9. The purpose of this method is to have each particle cover an equal area of phase space.

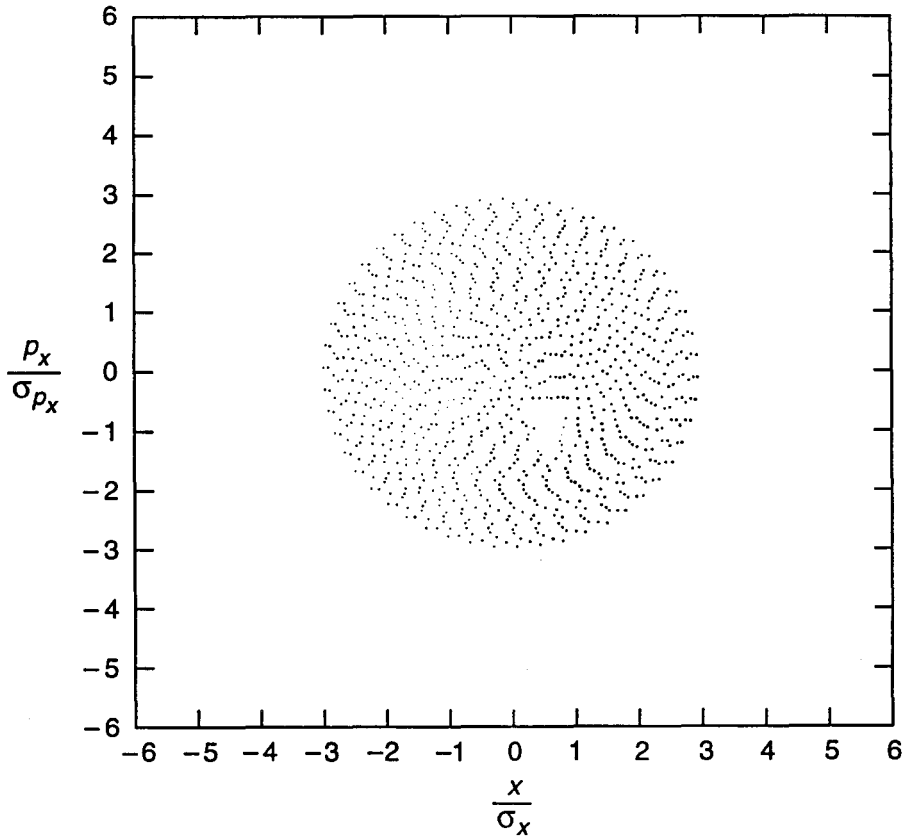

Figure 6.9. Uniform Distribution of 1000 Particles in x, p_x Phase Space.

6.4.2 Symplectic Mapping

Results from previous runs indicate that a higher-order integration scheme for the characteristic advance is necessary for the δf algorithm. In runs where only the leapfrog scheme is used, the code is inaccurate in the particle push. This higher-order integration scheme for the particles is needed in the δf algorithm because small changes to the initial distribution are being studied. In the PIC codes the numerical noise caused by the finite number of particles is larger than that produced by the numerical diffusion of the particles caused by the leapfrog integration scheme.

In this section we describe a symplectic, finite-difference scheme to counter the effects of numerical diffusion on the particle motion. In this scheme the normal symplectic mapping is used to advance the particles with an additional perturbation term.

Without the beam-beam force term, a symplectic transformation map for the characteristics with the magnetic field can be written. Also in the case of a linearized beam-beam force a symplectic transformation map can be written with slight modifications. The map can be written in the form:

$$\begin{pmatrix} x \\ x' \end{pmatrix}_f = \begin{pmatrix} \cos(\theta) & \beta_0^* \sin(\theta) \\ -\frac{1}{\beta_0^*}\sin(\theta) & \cos(\theta) \end{pmatrix} \begin{pmatrix} x \\ x' \end{pmatrix}_i , \tag{6.116}$$

where $x = dx/ds$, s is the coordinate along the collider, $\theta = \int_0^s ds/\beta_0^*$, and the indices i and f refer to the initial and final positions, respectively. This map is used at all places in the storage ring, including the interaction region. Upon adding the symplectic map the particle motion is accurate to many decimal places.

A simple implementation of the beam-beam force that preserves symplecticity involves approximating the force with an impulse. Using Hill's equation:

$$x'' + K(s)x = \frac{F(x)}{\gamma m v^2}\delta_p(s) , \tag{6.117}$$

where the term on the right-hand side of the equation is due to the beam-beam force. The mapping is the same as a tracking code with the beam-beam force:

$$\begin{pmatrix} x \\ x' \end{pmatrix}_f = \begin{pmatrix} 1 & 0 \\ G(x) & 1 \end{pmatrix} \begin{pmatrix} x \\ x' \end{pmatrix}_i , \tag{6.118}$$

where

$$G(x) = \frac{F_0(x)}{\gamma m v^2}\frac{1}{x} , \tag{6.119}$$

and $F_0(x)$ is the unperturbed force due to a Gaussian beam.

In the particle advance scheme the particles are advanced first using the transfer matrix for a distance in $\theta = \Delta s/4\beta_0^*$, where $\Delta s = c\Delta t$. The particles are then kicked by the beam-beam field for $\Delta s/2\beta_0^*$ and then advanced again $\Delta s/4\beta_0^*$. The total matrix is

$$\begin{pmatrix} x \\ x' \end{pmatrix}_f = M(\theta) \begin{pmatrix} 1 & 0 \\ G(x) & 1 \end{pmatrix} M(\theta) \begin{pmatrix} x \\ x' \end{pmatrix}_i , \tag{6.120}$$

$$M(\theta) = \begin{pmatrix} \cos(\theta) & \beta_0^* \sin(\theta) \\ -\frac{1}{\beta_0^*}\sin(\theta) & \cos(\theta) \end{pmatrix} , \tag{6.121}$$

where $\theta = \Delta s/(4\beta_0^*)$ and x used in $G(x)$ is the intermediate x value obtained from the first transfer matrix application:

$$G(x) = \frac{F_0(x)}{\gamma m v^2}\frac{1}{x}\frac{\Delta s}{2} . \tag{6.122}$$

6.4.3 Time Advance

In this section the time advance scheme of the code is described. The entire predictor-corrector advance scheme is shown in Table 6.1.

Table 6.1. Steps for Advance of δf Algorithm.

1	Start with $x^n, x'^n, \delta f^n, \delta f^{n-1}$
2	$\delta f^{n+1}_{\text{predict}}$ from $x^n, x'^n, \delta f^{n-1}, F^n(x^n, \delta f^n)$
3	$\delta f^{n+\frac{1}{2}}_{\text{predict}} = \frac{1}{2}(\delta f^{n+1}_{\text{predict}} + \delta f^n)$
4	$x^{n+\frac{1}{2}}, x'^{n+\frac{1}{2}}$
5	$\delta f^{n+1}_{\text{correct}}$ from $x^{n+\frac{1}{2}}, x'^{n+\frac{1}{2}}$ $\delta f^n, F^{n+\frac{1}{2}}(x^{n+\frac{1}{2}}, \delta f^{n+\frac{1}{2}}_{\text{predict}})$
6	x^{n+1}, x'^{n+1}
7	repeat steps 1–6 until the end of the interaction region
8	rotate x^{n+1}, x'^{n+1}
9	repeat steps 1–8 until the end of the simulation run

The n in Table 6.1 refers to the time step number. In step 2 $\delta f^{n+1}_{\text{predict}}$ is calculated from the discretization of Eq. (6.111):

$$w_i^{n+1}{}_{\text{predict}} = w_i^{n-1} - \frac{1}{n}\left[\left(F^n(x_i^n, \delta f^n) - F_0 x_i^n\right)\frac{\partial f_0(x_i^n, x_i'^n)}{\partial x'}\right] 2\Delta s\,, \tag{6.123}$$

where $\Delta s = c\Delta t$, and $F^n(x_i^n, \delta f^n)$ is the force calculated from the unperturbed Gaussian beam $F_0(x_i^n)$ plus the perturbation force $\delta F^n(x_i^n, \delta f^n)$. $\delta f^{n+1}_{\text{predict}}$ is then calculated using Eq. (6.110):

$$\delta f(x, x', s)^{n+1}_{\text{predict}} = \sum_{i=1}^{N} w_i^{n+1}{}_{\text{predict}}\,\delta\big(x - x_i(s)\big)\delta\big(x' - x_i'(s)\big)\,. \tag{6.124}$$

The same procedure is used in step 5 to calculate $\delta f^{n+1}_{\text{correct}}$:

$$w_i^{n+1}{}_{\text{correct}} = w_i^n + \Delta w\,, \tag{6.125}$$

$$\Delta w = -\frac{1}{n}\left[\left(F^{n+\frac{1}{2}}(x_i^{n+\frac{1}{2}}, \delta f^{n+\frac{1}{2}}) - F_0(s) x_i^{n+\frac{1}{2}}\right)\frac{\partial f_0\left(x_i^{n+\frac{1}{2}}, x_i'^{n+\frac{1}{2}}\right)}{\partial x'}\right]\Delta s\,. \tag{6.126}$$

In steps 4 and 6 x and x' are advanced using Eq. (6.120). In step 8 x and x' are advanced using Eq. (6.116):

$$\begin{pmatrix} x \\ x' \end{pmatrix}_i^{n+1} = \begin{pmatrix} \cos(2\pi\nu) & \beta_0^* \sin(2\pi\nu) \\ -\frac{1}{\beta_0^*}\sin(2\pi\nu) & \cos(2\pi\nu) \end{pmatrix} \begin{pmatrix} x \\ x' \end{pmatrix}_i^{n+1}, \tag{6.127}$$

where

$$\nu = \nu_0 - \frac{\Delta s}{\beta_0^*}, \tag{6.128}$$

which takes into account the finite length of the interaction region Δs in the phase space rotation.

6.5 Diagnostic Quantities

Analysis of the dynamics of the beam-beam interaction requires diagnostics of several quantities. Two typical accelerator quantities, the beam-beam tune shift parameter $\Delta\nu$ and the beam emittance ϵ, are calculated from the simulation. These quantities give an idea of the beam strength and beam size, respectively. Various moments of the beam are also measured to get an idea of macroscopic beam behavior. It is also important to determine the amount of particle diffusion occurring within the beams. This diffusion is measured using Poincare sections and the method of Chirikov.[3] Each of these diagnostic quantities is described in more detail in the following sections.

6.5.1 Emittance

A quantity of importance to accelerator physics is beam emittance ϵ. It is a measure of phase space area occupied by the beam particles. In a Hamiltonian system phase space area is conserved and, therefore, the phase space area should be conserved. The quantity often calculated in accelerator physics is the normalized emittance ϵ_n:[27]

$$\epsilon_n = (\beta\gamma)\pi\frac{1}{2}\frac{1}{\beta_0^*}\sum_{i=1}^{N}\left({x_i}^2 + \beta_0^* {x_i'}^2\right), \tag{6.129}$$

where β and γ are the usual relativistic quantities, β_0^* is the betatron oscillation length at the interaction point, $x' = p_x/p$, p_x is the transverse momentum, p is the momentum along the collider path, and N is the number of simulation particles. By including γ, ϵ_n remains constant even during the boost or acceleration phase of the beam. In the PIC codes ϵ_n may be calculated by just summing over the number of particles. In the δf algorithm an initial unperturbed emittance is calculated:

$$\epsilon_{n0} = (\beta\gamma)\pi\frac{1}{2}\frac{1}{\beta_0^*}\sum_{i=1}^{N}({x_i}^2 + \beta_0^* {x_i'}^2)w_{0i}, \tag{6.130}$$

where w_{0i} is the initial unperturbed distribution function f_0 for particle i. The perturbation is

$$\delta\epsilon_n = (\beta\gamma)\pi\frac{1}{2}\frac{1}{\beta_0^*}\sum_{i=1}^{N}({x_i}^2 + \beta_0^* {x_i'}^2)w_i, \tag{6.131}$$

where w_i is the time-evolving perturbation δf for particle i. This perturbation emittance is calculated and added to the initial ϵ_n to obtain the total ϵ_n.

6.5.2 Tune Shift

As described previously, the tune shift $\Delta\nu$ stands as a measure of the strength of the beam-beam kick. As the beams expand and contract, the kick weakens and strengthens, respectively. The various methods by which $\Delta\nu$ can be measured are described.

One method for measuring $\Delta\nu$ involves a least-squares-fit to the kicks of small and large amplitude particles. We use Sands'[52] expression for linear tune shift, which is valid for small amplitude particles:

$$\Delta\nu = \frac{\beta_0^*}{4\pi}\Delta K\ \Delta s\,, \tag{6.132}$$

$$\Delta K\ \Delta s = \frac{\Delta x'}{x}\,, \tag{6.133}$$

where $\Delta x' = \Delta p_x/p$ and $\Delta p_x = 2eE_x(x)\Delta t$. A least-squares-fit to $\Delta\nu$ can be performed:

$$(\Delta\nu)x_i = \left(\frac{\beta_0^*}{4\pi}\frac{1}{p}\right)\Delta p_{x_i}\,, \tag{6.134}$$

where x_i and Δp_{x_i} are for individual particles and the average $\Delta\nu$ is given as

$$\Delta\nu = \frac{\beta_0^*}{4\pi}\frac{1}{p}\frac{A}{B}\,, \tag{6.135}$$

where

$$A = N\sum_{i=1}^{N} x_i\Delta p_{x_i} - \sum_{i=1}^{N} x_i \sum_{i=1}^{N}\Delta p_{x_i}\,, \tag{6.136}$$

$$B = N\sum_{i=1}^{N} x_i^2 - \sum_{i=1}^{N} x_i \sum_{i=1}^{N} x_i\,. \tag{6.137}$$

The sums are over the number of particles N used in the fit. The tune shift for small-amplitude particles is measured from simulation particles lying within $0.1\sigma_0$ of the beam. Tune shifts measured using particles of the entire beam are smaller only for small-amplitude particles, since $\Delta\nu$ drops off at large amplitude. In the PIC codes the sums are carried out over the number of particles. In the δf method the sums are also carried out over the number of particles with the modifications:

$$A = N\sum_{i=1}^{N} x_i\Delta p_{x_i}w_i - \sum_{i=1}^{N} x_iw_i \sum_{i=1}^{N}\Delta p_{x_i}w_i\,, \tag{6.138}$$

$$B = N\sum_{i=1}^{N} x_i^2w_i - \sum_{i=1}^{N} x_iw_i \sum_{i=1}^{N} x_iw_i\,, \tag{6.139}$$

where w_i is the total distribution function value $f(x,x') = f_0(x,x') + \delta f(x,x')$ for particle i.

Another method for calculating $\Delta\nu$ uses the electric field $E_x(x)$. This can be done at one point x in the beam or as an average over several points. For one point:

$$\Delta\nu = \frac{\beta_0^*}{4\pi}\Delta K\ \Delta s\,, \tag{6.140}$$

$$\Delta K = \frac{2eE_x(x)}{\gamma m v^2}\frac{1}{x}\,, \tag{6.141}$$

and for several points:

$$\Delta\nu = \frac{\beta_0^*}{4\pi}\Delta K\ \Delta s\,, \tag{6.142}$$

$$\Delta K = \frac{1}{N}\sum_{i=1}^{N}\frac{2eE_x(x_i)}{\gamma m_i v_i^2}\frac{1}{x_i}\,, \tag{6.143}$$

where the sum is over N particles. The tune shift $\Delta\nu$ is calculated in the δf algorithm at one point from Eq. (6.140) by using $E_x(x) = E_{x0}(x) + \delta E_x(x)$, where $E_{x0}(x)$ is the unperturbed field and $\delta E_x(x)$ is the perturbation field. For several points in the δf method Eq. (6.142) becomes

$$\Delta\nu = \frac{\beta_0^*}{4\pi}\Delta K\ \Delta s\,, \tag{6.144}$$

$$\Delta K = \frac{\sum_{i=1}^{N}\frac{2eE_x(x_i)}{\gamma m_i v_i^2}\frac{1}{x_i}w_i}{\sum_{i=1}^{N}w_i}\,, \tag{6.145}$$

where w_i is the total distribution function value $f(x,x') = f_0(x,x') + \delta f(x,x')$ for particle i.

The power spectra of the x position of sample particles are another diagnostic method. The x positions are sampled after each complete turn around the collider. The power spectral density $P(\nu)$ is calculated from[53]

$$P(\nu) = \int_{-\infty}^{\infty} dn'\ \exp(-in'\nu)C(n')\,, \tag{6.146}$$

where n refers to the turn number, and $C(n)$, the autocovariance function, is given by

$$C(n') = \lim_{N\to\infty}\left\{\frac{1}{2N}\int_{-N}^{+N} x(n)\ x^*(n+n')dn\right\}, \tag{6.147}$$

where n' is the lag in the number of rotations. The previous expression assumes that $x(n)$ is a continuous function of n. In the simulations, $C(n')$ is calculated from a discrete set of values:[54]

$$C(r) = \frac{1}{N-r} \sum_{n=1}^{N-r} x(n)x^*(n+r)\,, \tag{6.148}$$

where $r = 0, ..., m$, r is the rotation lag, m is the maximum rotation lag, and N is the total number of rotations. The autocovariance function may be calculated using an FFT with $N = 2^k$. The maximum rotation lag was constrained to be less than 0.25 N for accuracy. The power spectral density is calculated by

$$P(\nu) = \mathrm{FFT}[C(r)W(r)]\,, \tag{6.149}$$

where $W(r)$ is the window function, the Parzen lag weighting functions.[55] The tune shift can be determined from the frequency shift in the power spectral peak. The frequency spectrum peaks at the unperturbed tune ν_0 when the beam-beam interaction is not present. The error in measuring the tune shift $\Delta\nu$ is given by

$$\delta(\Delta\nu) = \frac{2}{m}\,, \tag{6.150}$$

where m is the maximum lag in rotations.

6.5.3 Determination of Beam Moments

Other quantities of importance in diagnosing beam dynamics are the beam moments, which may be studied in two different approaches. One way involves calculating the cumulants of the particle positions x for each beam:[56]

$$< x > = \frac{1}{N} \sum_{i=1}^{N} x_i \tag{6.151}$$

$$< x^2 > = \frac{1}{N} \sum_{i=1}^{N} (x_i - < x >)^2 \tag{6.152}$$

$$< x^3 > = \frac{1}{N} \sum_{i=1}^{N} (x_i - < x >)^3 \tag{6.153}$$

$$< x^4 > = \frac{1}{N} \sum_{i=1}^{N} (x_i - < x >)^4 - 3(x_i - < x >)^2\,, \tag{6.154}$$

where N is the number of particles. In the δf technique the cumulants are calculated:

$$< x > = \frac{1}{N} \sum_{i=1}^{N} x_i w_i \tag{6.155}$$

$$< x^2 > = \frac{1}{N} \sum_{i=1}^{N} (x_i - < x >)^2 w_i \tag{6.156}$$

$$< x^3 > = \frac{1}{N} \sum_{i=1}^{N} (x_i - < x >)^3 w_i \tag{6.157}$$

$$< x^4 > = \frac{1}{N} \sum_{i=1}^{N} (x_i - < x >)^4 - 3(x_i - < x >)^2 w_i \,. \tag{6.158}$$

Power spectra of the cumulants give the frequency components that contribute to each mode.

Another method involves taking the moments directly from a certain functional form:

$$f(m) = \sum_{i=1}^{N} \exp(im\theta_i) \,, \tag{6.159}$$

where N is the particle number, m is the particular moment, and

$$\theta_i = \tan^{-1} \left(\frac{\beta^* x_i'}{x_i} \right) , \tag{6.160}$$

where x_i is the particle position, and x_i' is $\frac{dx}{ds}_i$. The advantage of this method is in determining the mode structure of the beams. The growth of the quantity $f^*(m)f(m)$, where $f^*(m)$ is the complex conjugate of $f(m)$, determines the strength of particular modes in the beam. For example, particular modes should dominate near resonances. The mode $m = 4$ should dominate near $\nu = \frac{1}{4}$, and mode $m = 6$ should dominate near $\nu = \frac{2}{6}$.

6.5.4 Determination of Diffusion

Two methods of determining the stochastic nature of particle motion are employed. One simple method involves the use of Poincare surface of sections. A Poincare map is generated of sample test particles that are placed in the code. The map plots the particle position in x/β^* and x' coordinates at each time step. Each point represents the particle on a turn-by-turn basis. The advantage of this method is in seeing the diffusive nature of the particles and in determining regions of stability in phase space.

The second method is to calculate the diffusion of particles. Diffusion coefficients may be calculated in the following manner:[2,3]

$$D_k = \frac{2}{N_k(N_k-1)} \sum_{m>l} \frac{[\bar{X}(m) - \bar{X}(l)]^2}{(\Delta N_k)(m-l)}\,, \qquad k = 1,2\,, \tag{6.161}$$

where N_k is the number of subintervals, ΔN_k is the size of the subinterval in terms of rotations, k refers to the subinterval type, and $\bar{X}(m)$ is the average of x_n over the subinterval m:

$$\bar{X}(m) = \frac{1}{\Delta N_k} \sum_{n=1}^{\Delta N_k} \left| \frac{x_{l+n}}{\sigma_x} \right|, \tag{6.162}$$

where $l = m\,\Delta N_k$. The total number of rotations is broken up into two different subinterval sizes. Diffusion coefficients are calculated for each different subinterval. If we find the coefficients computed with different sampling intervals,

$$D_1 \approx D_2\,, \tag{6.163}$$

then the motion x is diffusive. This occurs since a diffusive process should be independent of the number of subintervals. On the other hand, if the initial conditions are chosen within "islands" of stable oscillatory motion : $[\bar{X}(m) - \bar{X}(l)] \propto (\Delta N_k)^{-1}$, then

$$\frac{D_2}{D_1} \propto \frac{(\Delta N_1)^3}{(\Delta N_2)^3} < 1\,. \tag{6.164}$$

The average in Eq. (6.162) is intended to lower the influence of bounded energy oscillations and to pick out accumulating changes.[3] The averaging made over all pair combinations of intervals is intended to increase the time scale for which diffusion is described by the rate, and it facilitates the separation of diffusion processes from side effects. The mean value of Δt is about half the total time and is independent of the length of the interval Δt_n.[3]

7.0 SIMULATION RESULTS

In this section we describe results of the study of the beam-beam interaction with the various codes that have been developed. The effects of the filamentation instability[23] are examined using the electromagnetic code and Vlasov code. Beam-beam collective effects are examined using the electromagnetic code, strong-strong code, and δf code. Particle diffusion is also examined with the use of all the codes. A comparison of the different codes is made.

7.1 Filamentation Instability

In this section we discuss the results from the electromagnetic PIC code and the Vlasov code. We focus on the filamentation instability in counterstreaming beams.

7.1.1 Electromagnetic Code Results

To test the electromagnetic code described in Section 6.3.2, runs are performed with two counterstreaming proton beams and with no rotation in phase space due to accelerator magnets. This is a control run to check the growth rate of the filamentation instability. Figure 7.1 shows the filament formation of one beam in (x, p_x) space at $\omega_b T = 50$, 100, and 150, where ω_b is the beam plasma frequency. The beams are counterstreaming in the the y direction. The initial beam size is 128Δ, with a simulation box size of 512Δ and a relativistic factor of $\gamma = 100$. The maximum growth rate expected is $\Gamma_{max}\gamma^{1/2}/\omega_b = 0.5$ with a filament size of $\lambda \approx \lambda_c$, where $\lambda_c = c\gamma^{1/2}/\omega_b$ is the collisionless skin depth. At $\omega_b T = 150$ the separate filament sizes correspond approximately to a collisionless skin depth λ_c, and the measured growth rate is $\Gamma_{max}/\omega_b \approx 0.3$. Figure 7.2 shows results from varying the relativistic factor γ. The measured growth rates Γ_{max}/ω_n are in close agreement with the predicted growth rate of $\Gamma_{max}/\omega_n = 1/2$, where $\omega_n = \omega_b/\gamma^{1/2}$ is the beam plasma frequency normalized by γ.

Results of simulation runs with a small ratio of beam radius, w_b, to collisionless skin depth, $\lambda_c = c\gamma^{1/2}/\omega_b$, are shown in Figure 7.3. Growth rates were measured with and without the electric field included in the simulation. It is apparent that the growth rates with the electric field included in the simulation are in agreement with the theoretical growth rate of $\Gamma/\omega_n = 0.5$. Thus, it appears as if the small beam width has not suppressed the instability. When the electric field calculation is not included, the growth rates increase by a factor of approximately two. The inclusion of the electric field causes expansion of the beams and suppresses the pinching in x of the beams by the magnetic field.

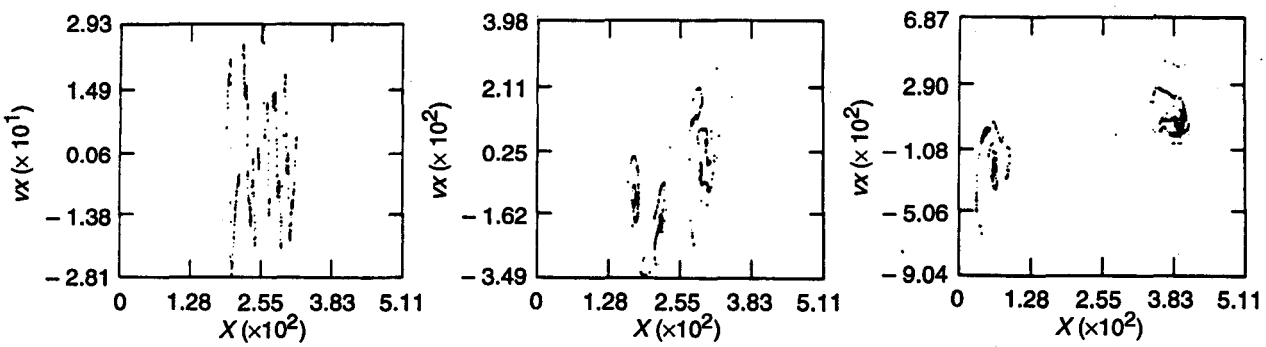

Figure 7.1. (x, p_x) Phase Space Plots for $\omega_b T = 50$, 100, and 150 at the Top, Middle, and Bottom of the Figure, Respectively, with $\gamma = 100$.

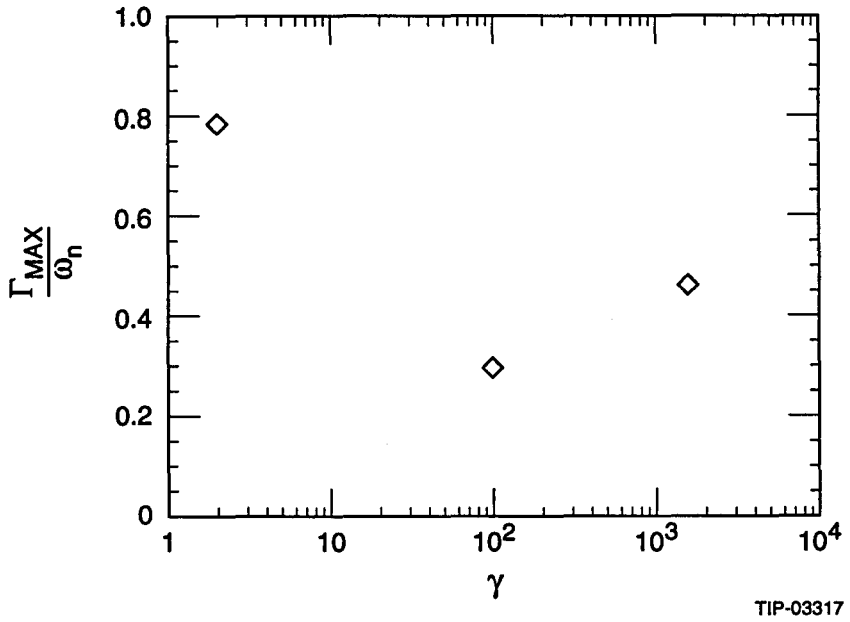

Figure 7.2. Growth Rate of Filamentation Instability Γ_{max}/ω_n, Where $\omega_n = \omega_b/\gamma^{1/2}$, for Three Values of γ.

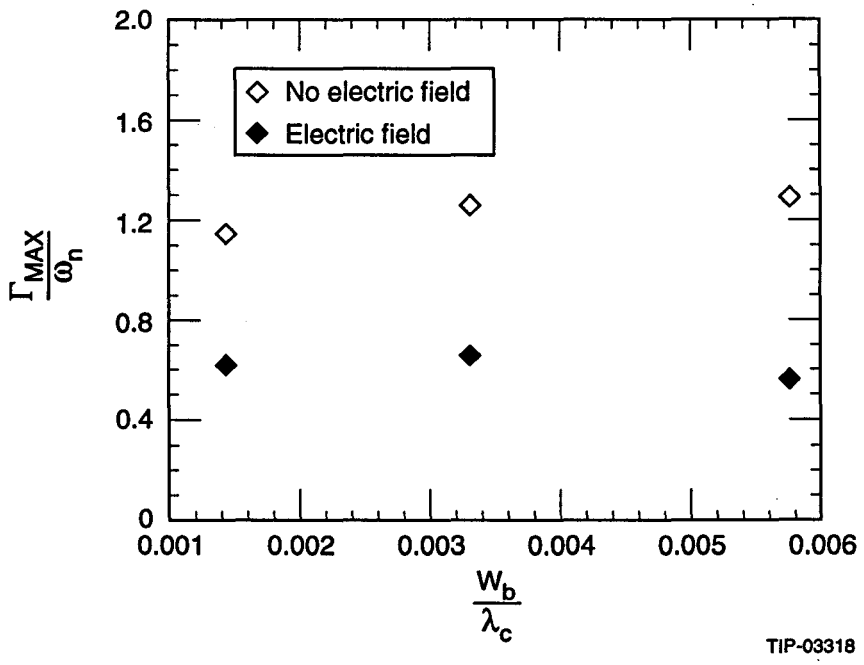

Figure 7.3. Maximum Growth Rate Γ_{max}/ω_n With and Without the Electrostatic Field Calculation, Where $\omega_n = \omega_b/\gamma^{1/2}$, Versus the Ratio of Beam Radius ω_b to Collisionless Skin Depth $\lambda_n = c\gamma^{1/2}/\omega_b$.

7.1.2 Vlasov Code Results

A problem involving two counterstreaming electron beams is examined with the Vlasov code. The beams are unstable to the filamentation instability, which has a maximum growth rate Γ_{max} of[23]

$$\frac{\Gamma_{max}\gamma^{1/2}}{\omega_b} = \frac{1}{2}. \tag{7.1}$$

The code is timed for various problem sizes, and performance is compared with the Cray YMP. The results presented here are only for the Cartesian geometry case.

Figure 7.4 shows the growth in the field energy as a function of time in units of the background plasma frequency, ω_{pe}. The field energies are plotted for the three machines on which the problem was run (Intel i860, a Connection Machine, and a Cray YMP). Note that the results agree well over the length of the run. The slight differences can be attributed to the differences in precision and random number generators used for the initialization of the fields. Using the growth time of 400 simulation time steps from the simulations, the measured growth rate is

$$\frac{\Gamma\gamma^{1/2}}{\omega_b} \approx 0.4. \tag{7.2}$$

This measured growth rate is close to the theoretical filamentation growth rate. The ratio of beam width w_b to the collisionless skin depth λ_c is

$$\frac{w_b}{\lambda_c} \approx 1.5. \tag{7.3}$$

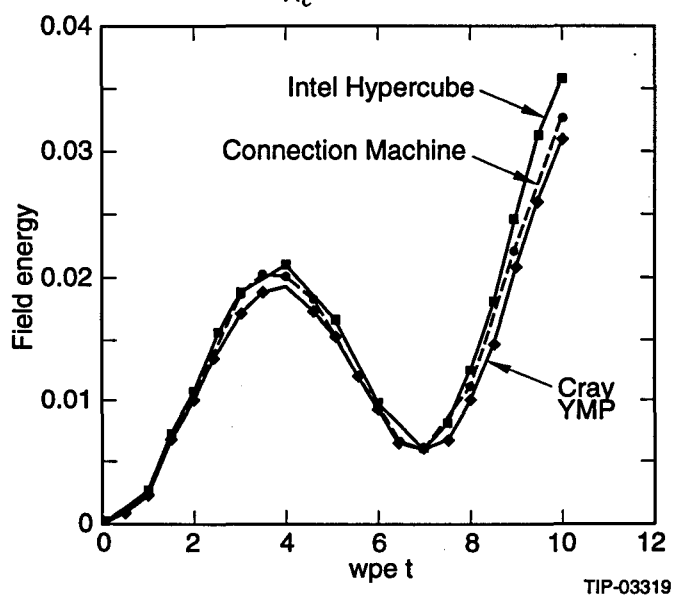

Figure 7.4. Comparison Between the Intel Hypercube, the Connection Machine, and the Cray YMP on a Test Problem. The growth in field energy as a function of time ($\omega_{pe}t$) is shown.

The integrated distribution functions of one of the beams at various time steps are shown in Figures 7.5 and 7.6. The other beam evolves in a similar manner. The evolution of the $x - z$ distribution function is shown in Figure 7.5. The beam starts out as a finite-width beam in x with an initial small perturbation in z. (The oscillations can be seen along the beam at the top.) As the beam evolves, it begins to spread in x. The filament formation is evident for $f(x, z)$ in Figure 7.5 after 400 time steps. The filament sizes are approximately between $0.5\lambda_c$ and λ_c. By the end of a 1000-time step run the beam has spread to the point where the multiple beams are beginning to overlap due to the periodic boundary conditions. By the end of the run the results are no longer valid for a single beam, since overlap has occurred. Results before this point are valid.

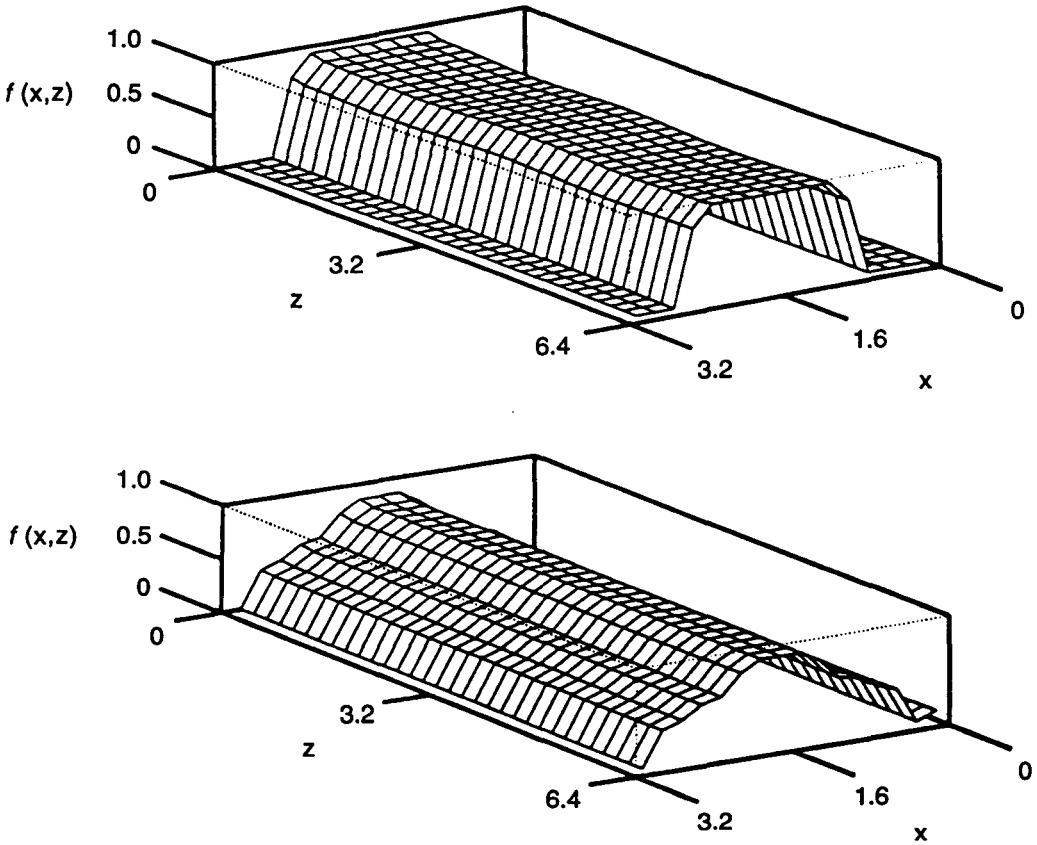

Figure 7.5. Integrated Distribution Function $f(x, z)$ at 0 and 400 Time Steps from the Top to the Bottom.

Note that the $z - p_z$ distribution function in Figure 7.6 becomes negative, an inherent problem with Vlasov simulation techniques. Since only two points are chosen to represent the distribution function of the two beams in p_z space, truncation errors result that cause the distribution function to become negative. A solution to this problem may be in higher resolution in p_z, which translates into a larger number of grid cells and more memory. Another approach may be to use transform methods in the momentum directions.[38] This truncation error still needs to be resolved.

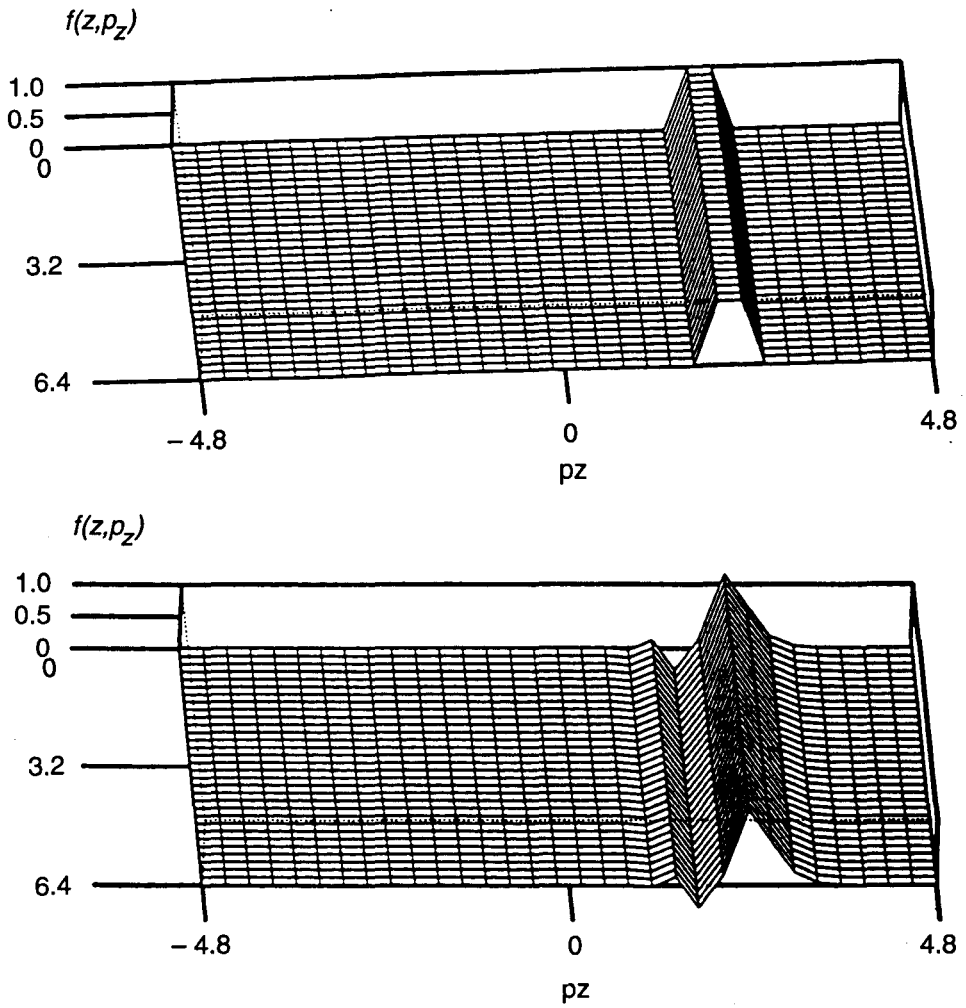

Figure 7.6. Integrated Distribution Function $f(z, p_z)$ at 0 and 400 Time Steps from the Top to the Bottom.

The maximum speed of the code is approximately 152-million floating-point operations per second (MFLOPS) for 32 nodes. The efficiency of the code is dependent on the ratio of the number of floating-point operations per node to the number of transfers per node. It is obvious that reduction in communication increases efficiency. In the extreme case of no communication the number of MFLOPS would be linearly dependent on the number of nodes. We assume the exclusion of speedup due to vectorization that would depend on problem sizes. The amount of communication per node can be minimized by considering the shape of the region computed for each node. Two quantities that give an indication of the shape are the perimeter of the region, which is $2(nc_x + nc_z)$, and the area of the region, $nc_x \cdot nc_z$, where nc_x and nc_z are the number of cells per node in the x and z direction, respectively. The ratio of the perimeter to the area of the region is in proportion to the amount of communication per computation for each node. The ratio can be represented by the formula

$$\frac{p}{a} = \left(\frac{2(r+1)}{\sqrt{r}}\right)\frac{1}{\sqrt{N}}, \tag{7.4}$$

where

$$r = \frac{nc_x}{nc_z}, \tag{7.5}$$

$$N = nc_x \cdot nc_z. \tag{7.6}$$

Minimizing p/a reduces the amount of communication per computation for each node. The smallest value is achieved by choosing $r = 1$ for a fixed number of cells per node N. At this point it can be seen why a slab geometry is not optimal for communication. Although the slab geometry needs only two directions of communication, the ratio r is generally far from 1. Also, as the number of nodes is increased, the ratio r increases. Eq. (7.4) also shows that the larger the total problem size, the larger N is for a fixed number of nodes. So efficiency is also enhanced when the problem size is large. The problems with the highest efficiency or MFLOPS per node are the problems with the largest number of grid points per node.

As a comparison of outright speed, a serial version of the code was also run on the Cray YMP at NASA Ames. No effort was made to optimize the code for vectorization. Tests are performed on the code with 32 nodes on the Ames hypercube. The speed was 2.3 times faster than the Cray YMP for the largest problems run. Although this may not be a fair test, it does give a rough idea of the size of the parallel machine necessary to achieve speeds comparable to a Cray YMP. Obviously a more rigorous test needs to be performed where both codes are optimized for each specific machine.

There are a few improvements that can be made. The distribution function goes negative after a few hundred time steps. A solution may be to increase the resolution of the velocity distribution or to go to some type of transform method.[38] Another solution is to use the δf method on the Vlasov technique, which will be discussed in Section 8.0.

7.2 Collective Beam-Beam Effects

In this section the object is to describe the effects of the beam-beam interaction on macroscopic beam behavior—that is, phenomena that deal with the entire beam, such as beam blowup.

7.2.1 Reference Parameters

Our research is generic enough to cover the beam-beam interaction of various colliders or storage rings. We make specific reference to the parameters of the SSC, shown in Table 7.1. Using the numbers from the table we have: $\gamma = 2.13 \times 10^4$ and $\omega_b \tau_{int} = 0.035$,

where $\omega_b = \sqrt{4\pi e^2 n_b/\gamma m_b}$, $n_b = N_B/(lwh)$ is the beam density, m_b is the mass of the beam particles (protons), γ is the relativistic factor, and $\tau_{int} = L/2c$ is the interaction time of the colliding beams. The horizontal tune shift $\Delta\nu_{HO}$ is calculated for a two-dimensional Gaussian beam. Since the present simulations deal with only one-dimension, this quantity is recalculated. Using the equation for the one-dimensional tune shift:

$$\Delta\nu_0 = \sqrt{\frac{2}{\pi}}\frac{\beta^* r_p N_B}{\gamma h w}, \tag{7.7}$$

and using values from Table 7.1, the one-dimensional tune shift is $\Delta\nu_0 = 2.1 \times 10^{-3}$. A series of simulation runs is performed using the parameters described in Table 7.1.

Table 7.1. SSC Parameters.

$l \times w \times h$	=	7.5 cm $\times 10^{-3}$ cm $\times 10^{-3}$ cm
N_B	=	7.3×10^9
T	=	20 TeV protons
β^*	=	50 cm
$\Delta\nu_{HO}$	=	0.84×10^{-3}
ν_{HO}	=	0.285
Luminosity	=	10^{33} cm^{-2} s^{-1}
Lifetime	=	24 h or 10^8 turns

Electromagnetic Code Results. Runs of 1000 turns are performed using the reference parameters described in Table 7.1, with $\nu_0 = 0.285$ and $\Delta\nu_0 = 2.1 \times 10^{-3}$. In order to keep the time between rotations reasonable ($\approx$ 1000 time steps), a beam width larger than that of the SSC is used. This is due to constraints of following light waves in the electromagnetic code. The ratio w_b/λ_c is still small at $\approx 10^{-3}$. Also, to save on computation time 256 particles are used for each beam. Measurements of the tune shift $\Delta\nu$ for both beams for small-amplitude particles are shown in Figure 7.7. The tune shift $\Delta\nu$ oscillates about an average of 1.87×10^{-3} and 1.93×10^{-3} for beams 1 and 2, respectively. The predicted tune shift for a one-dimensional Gaussian beam using SSC parameters is 2.1×10^{-3}. The fluctuation level of $\Delta\nu$ is approximately $\pm 15\% \Delta\nu_0$. This large fluctuation level is attributed to the small number of particles used. Figure 7.8 shows the initial and final $(x/\sigma_x, p_x/\sigma_p)$ phase space particle positions. Little difference is seen between the initial and final configurations.

Some of the shortcomings of this fully self-consistent method are clear: 1) it is too costly for such a small number of particles, and 2) a large number of time steps is necessary for one

rotation. For realistic SSC parameters the simulation time step size Δt is about $3\times10^{-5}\tau_{int}$. We will concentrate on more efficient methods of modelling the beam-beam interaction in the rest of the paper.

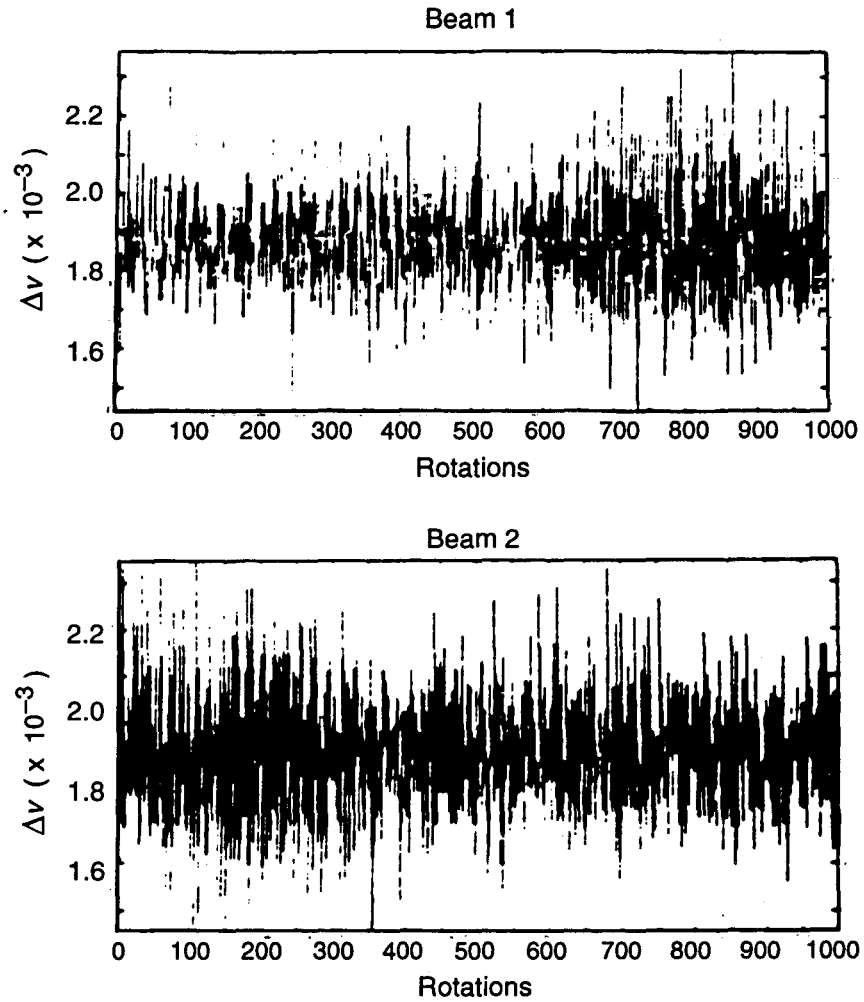

Figure 7.7. Tune Shift of Interacting Beams.

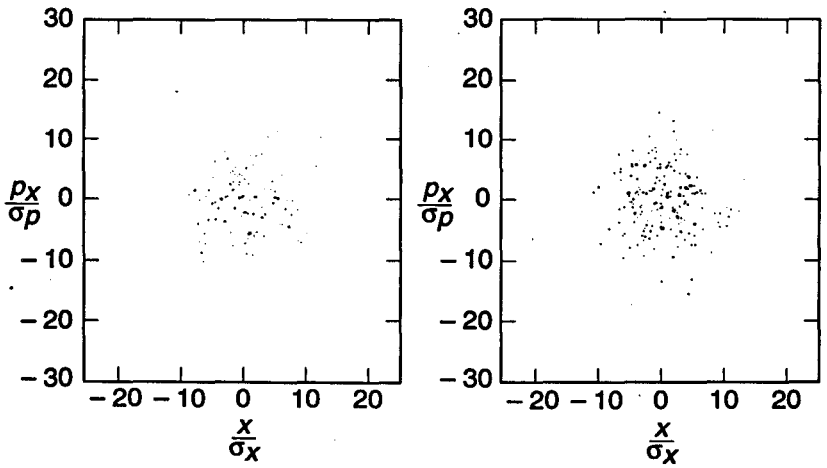

Figure 7.8. Initial (Top) and After 1000 Rotations (Bottom) $(x/\sigma_x, p_x/\sigma_p)$ Phase Space Particle Positions.

Strong-Strong Simulation Results. A series of strong-strong simulations has been performed to determine long time characteristics. The initial distribution of particles is shown in Figure 6.5. In this run 10^4 particles are used in each beam, with variable charge per particle initially to maintain a Gaussian distribution. The tune $\nu_0 = 0.285$ and the tune shift $\Delta\nu_0 = 2.1 \times 10^{-3}$. The simulation box size is 128Δ, where Δ is the cell size. The beam width w is 30Δ and the particle size a is Δ. The particle size a is small enough in relation to the beam width w so that from Eq. (6.57):

$$\frac{\Delta\nu_{point}}{\Delta\nu_{fsp}} = 1.0022\,, \tag{7.8}$$

where $\Delta\nu_{point}$ is the tune shift for a point particle and $\Delta\nu_{fsp}$ is the tune shift for a finite-size particle. Thus, finite-size particle effects on the kicks that the simulation particles receive are minimal. By normalizing the code to a plasma with density lower than the beam, where ω_0 is the normalization plasma frequency and ω_b is the beam plasma frequency, only four simulation time steps are needed to cover the interaction region. So $\omega_0\Delta t = 0.25$, where Δt is the simulation time step size.

Figure 7.9 shows the distribution of 10^4 particles in $(x/\sigma_x, p_x/\sigma_p)$ phase space for one beam after 10,240 rotations. The particles were initialized using the nonuniform charge distribution (Figure 6.5). After 10,240 rotations the particles are no longer uniformly distributed in $(x/\sigma_x, p_x/\sigma_p)$ space. Clumping of particles has occurred, and small regions contain no particles. However, no dominant mode such as an $m = 2$ mode (football shape) or $m = 4$ mode (square shape) has appeared, which would distort the shape of the whole beam. A profile in x of the distribution of particles in Figure 7.10 shows the deviation of the distribution from the initial Gaussian profile. The center of the beam is at $x = 64\Delta$. Large spikes in the distribution are visible at $x \approx 50\Delta$ and $x \approx 80\Delta$.

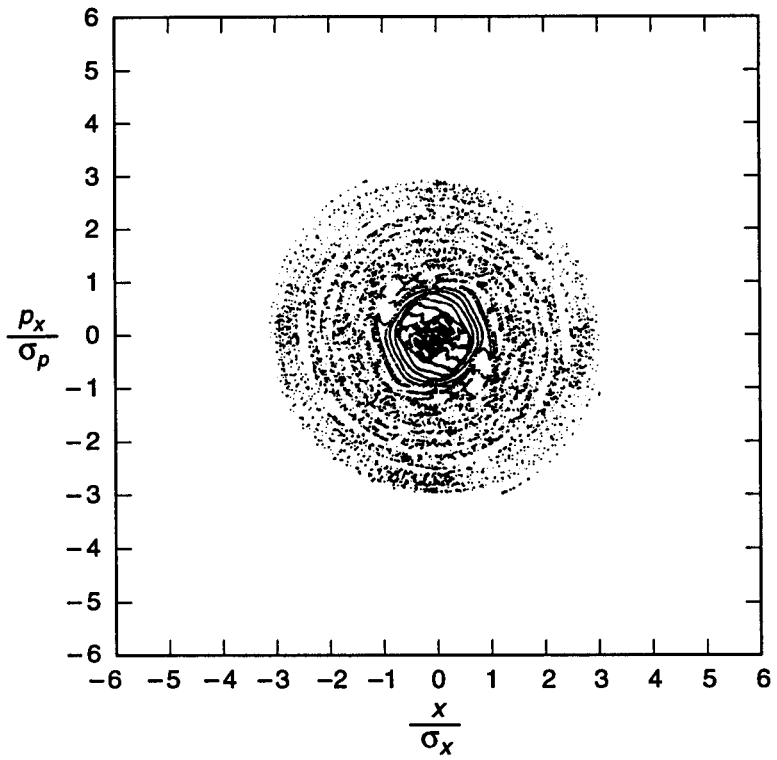

Figure 7.9. Distribution of 10^4 Simulation Particles in $(x/\sigma_x, p_x/\sigma_p)$ Space After 10,240 Rotations, with $\nu_0 = 0.285$ and $\Delta\nu_0 = 2.1 \times 10^{-3}$.

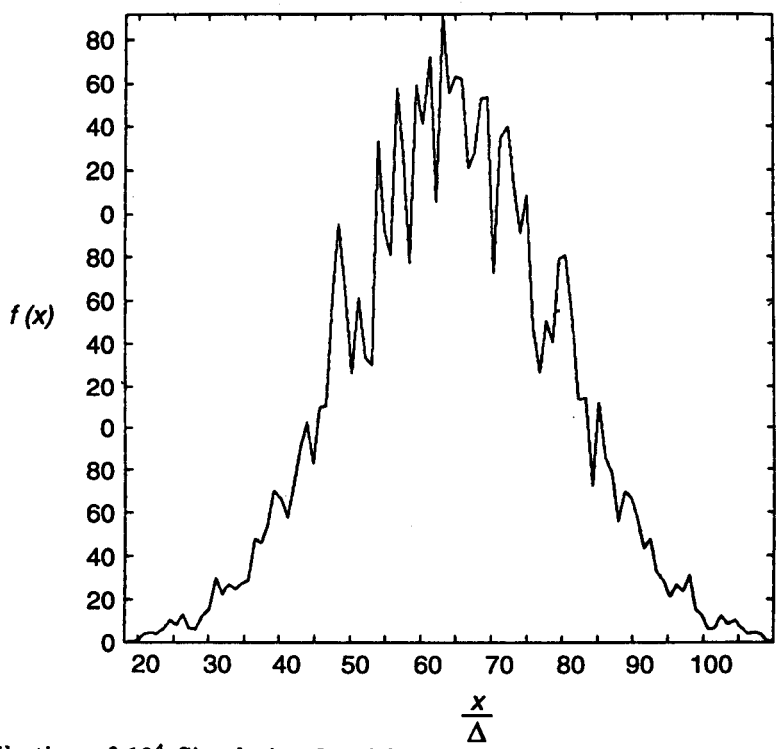

Figure 7.10. Distribution of 10^4 Simulation Particles in x After 10,240 Rotations, with $\nu_0 = 0.285$ and $\Delta\nu_0 = 2.1 \times 10^{-3}$.

We measure the tune shift $\Delta\nu$ by two methods described in Section 6.5.2. One method involves a least-squares-fit to the kicks of small- and large-amplitude particles.

Results from the least-squares-fit method for one beam are shown in Figure 7.11. The fit is done for small-amplitude particles $x < 0.1\sigma_x$ at the top of the figure, and for the entire beam for the bottom of the figure. The tune shift $\Delta\nu$ oscillates around the unperturbed values of $\Delta\nu_0 = 2.1 \times 10^{-3}$ for small-amplitude particles and $\Delta\nu_0 \approx 1.55 \times 10^{-3}$ for all the particles. The discrepancy is due to the drop-off of the kick at large values of x. When all particles are included in the least-squares-fit, the measured $\Delta\nu$ is lowered by the particles with large x. The amplitude of the variation in $\Delta\nu$ for small-amplitude particles is approximately $\pm 20\%$ of $\Delta\nu_0$ near the end of the run. The tune shift obtained from all particles decreases in amplitude with the number of rotations. The maximum variation of $\Delta\nu$ is approximately $\pm 3\%$ of its average value and occurs within the first 500 rotations. The oscillations in $\Delta\nu$ indicate expansion and contraction of the beam. The expansion and contraction of the beam decreases and increases $\Delta\nu$, respectively. Notice that the beam is expanding and contracting differently at different particle positions. The small-amplitude portion of the beam is increasing in oscillation amplitude, while the entire beam is decreasing in oscillation amplitude.

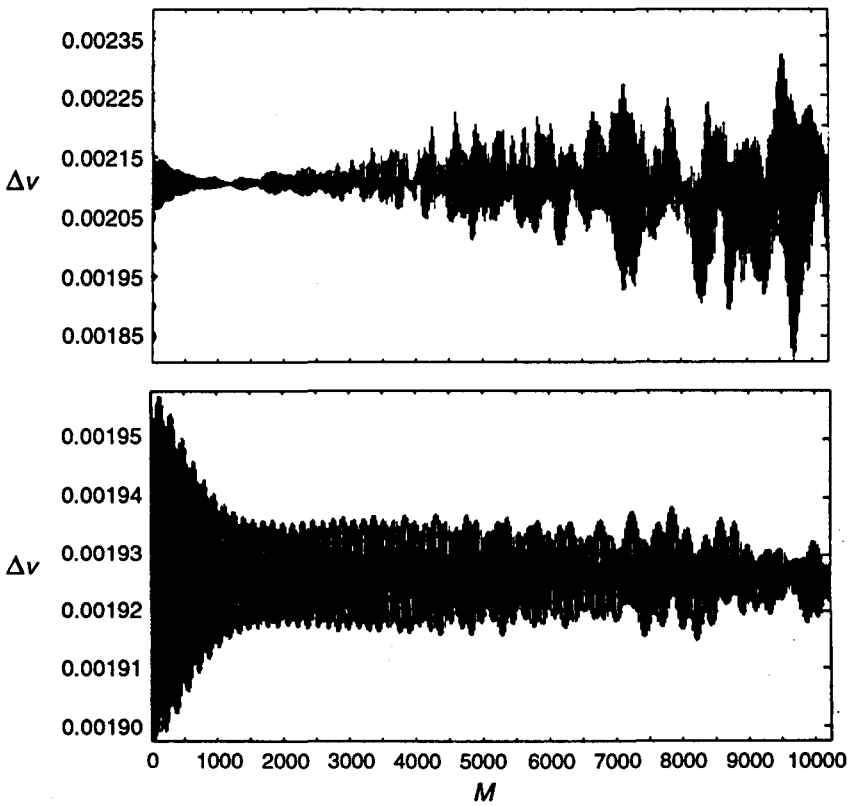

Figure 7.11. Tune Shift $\Delta\nu$ from a Least-Squares-Fit to Small-Amplitude Particles $x < 0.1\sigma_x$ (Top) and All Particles (Bottom) for $M = 10,240$ Rotations.

The other method by which the tune shift $\Delta\nu$ is measured is by obtaining power spectra of the x positions of sample particles, which are sampled once every complete rotation. Figures 7.12 and 7.13 show the particle positions and power spectra for a small- and large-amplitude particle, respectively. The tune shift $\Delta\nu$ is measured from the shift in the power spectral peak from the unperturbed tune ν_0. The small-amplitude particle in Figure 7.12 shows smearing in the particle position in phase space. This is indicative of particle diffusion, which will be discussed in Section 7.3. The peaks in $S(\nu)$ are at $\nu = \pm 0.2827148$. The difference from ν_0 is 2.2852×10^{-3}. The error in this measurement is $\delta\nu = 7.8125 \times 10^{-4}$, where the maximum lag time is 2560 rotations for the power spectrum calculation. Although the value is higher than the unperturbed tune shift $\Delta\nu_0$, it is within the errors of the calculation. The large amplitude particle in Figure 7.13 also shows smearing in the particle position in phase space, but it is less than that observed for the small-amplitude particle. The peaks in $S(\nu)$ are at $\nu = \pm 0.2832031$. The difference from ν_0 is 1.7969×10^{-3}. The error in this measurement is also $\delta\nu = 7.8125 \times 10^{-4}$. The tune shift, $\Delta\nu$, for the large-amplitude particle is smaller than the one measured for the small-amplitude particle, since $\Delta\nu$ drops off with large x for the beam-beam interaction.

Moments of one beam are shown in Figures 7.14 and 7.15. At the top of Figure 7.14 the oscillation of the average beam center $< x >$ is apparent. The beam oscillates with a maximum beam amplitude of $\delta x/\sigma_x \approx \pm 8 \times 10^{-4}$. The average $< x >$ and $< (x- < x >)^3 >$, the odd moments, are both increasing in oscillation amplitude with rotation number. The increase is more obvious for $< (x- < x >)^3 >$ at the bottom of Figure 7.14. At the top of Figure 7.15 the oscillation of the beam width can be seen. The beam is oscillating about the initial beam width σ_x^2 with a maximum amplitude of approximately $\pm 0.04\sigma_x^2$. Oscillations are also apparent for $< (x- < x >)^4 >$ at the bottom of the figure. The amplitudes of the even moments $< (x- < x >)^2 >$ and $< (x- < x >)^4 >$ are both decreasing with the number of rotations. Note that the variation in the second moment $< (x- < x >)^2 >$ closely corresponds with the variation of the tune shift measured from all beam particles in Figure 7.11. Both $\Delta\nu$ and $< (x- < x >)^2 >$ give a measure of the width of the kicking beam and the kicked beam, respectively. Since both beams are oscillating in width in the same manner, the agreement is expected.

Figures 7.16 and 7.17 show the moments and their associated power spectrum. The power spectrum of the average of x, $< x >$, is shown at the bottom of Figure 7.16. There is a peak in $S(\nu)$ at $\nu \approx 0$. This peak corresponds to oscillations seen in $< x >$ with periods between 500 and 1000 rotations. The smaller peaks at $\nu \approx \pm(\nu_0 - \Delta\nu_0)$ correspond to the betatron motion. In Figure 7.17 the peaks in the power spectra $S(\nu)$ at $\nu \approx \pm(1 - 2(\nu_0 - \Delta\nu_0))$ also correspond to the betatron motion of the beam.

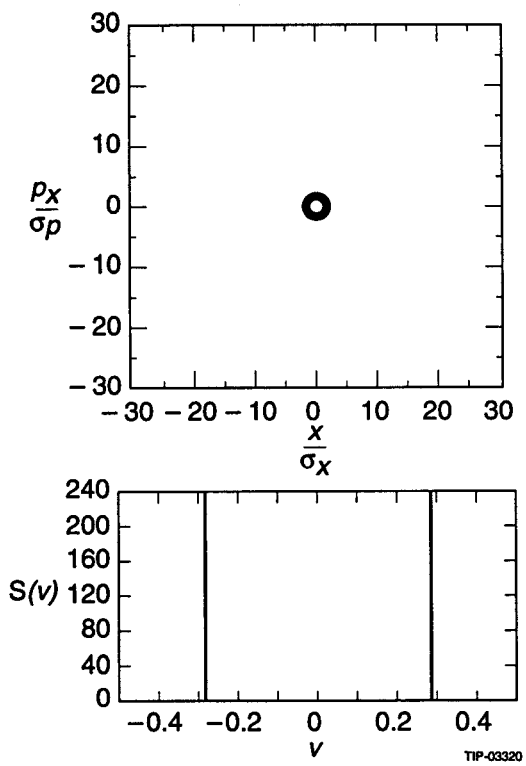

Figure 7.12. Position of an Initially Small-Amplitude Particle $x_0 = 0.1\sigma_x$ in $(x/\sigma_x, p_x/\sigma_p)$ Space for $M = 10,240$ Rotations (Top) and Power Spectrum of x Position of the Particle Versus ν (Bottom).

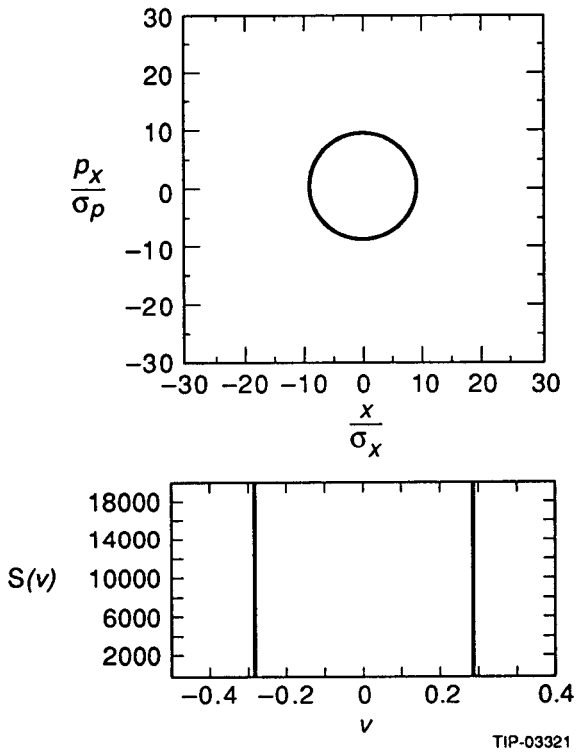

Figure 7.13. Position of an Initially Large-Amplitude Particle $x_0 = 0.9\sigma_x$ in $(x/\sigma_x, p_x/\sigma_p)$ Space for $M = 10,240$ Rotations (Top) and Power Spectrum of x Position of the Particle Versus ν (Bottom).

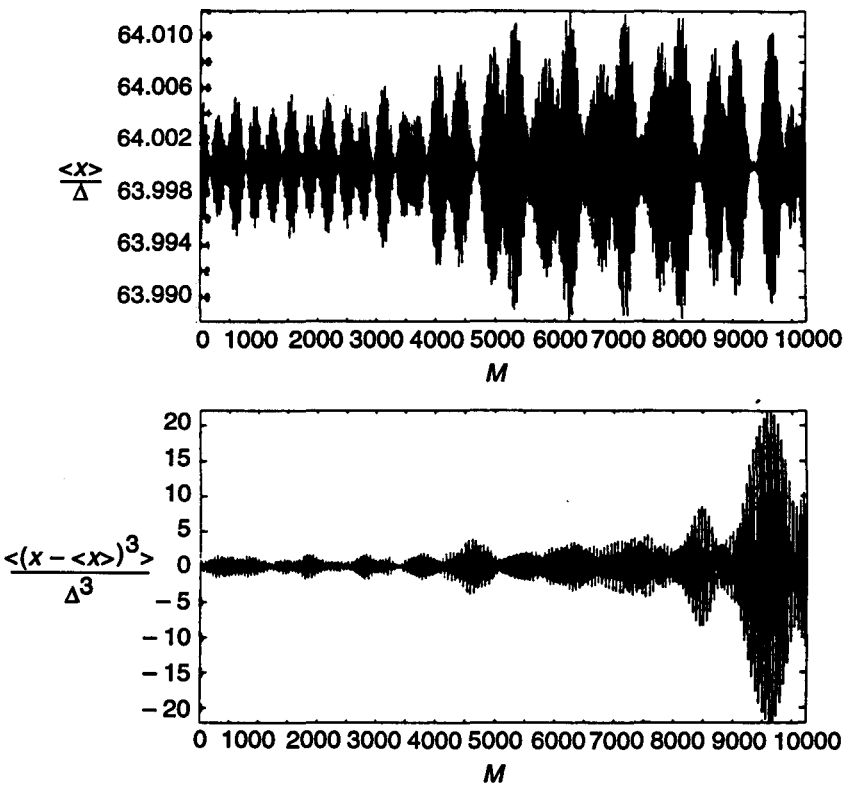

Figure 7.14. Beam Moments $< x >$ and $< (x- < x >)^3 >$ for $M = 10,240$ Rotations at the Top and Bottom of the Figure, Respectively.

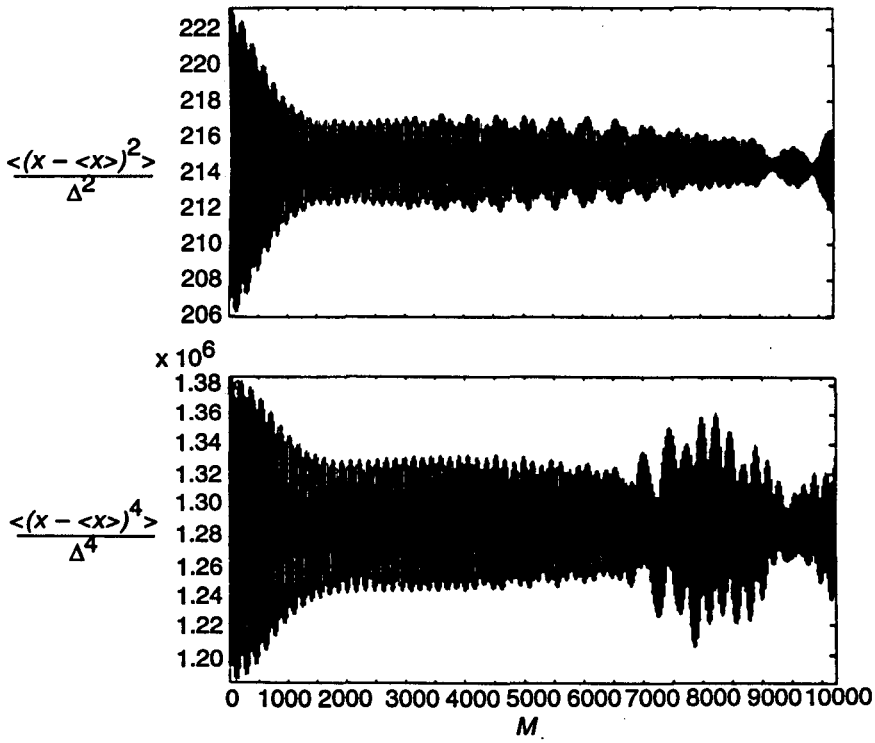

Figure 7.15. Beam Moments $< (x- < x >)^2 >$ and $< (x- < x >)^4 >$ for $M = 10,240$ Rotations at the Top and Bottom of the Figure, Respectively.

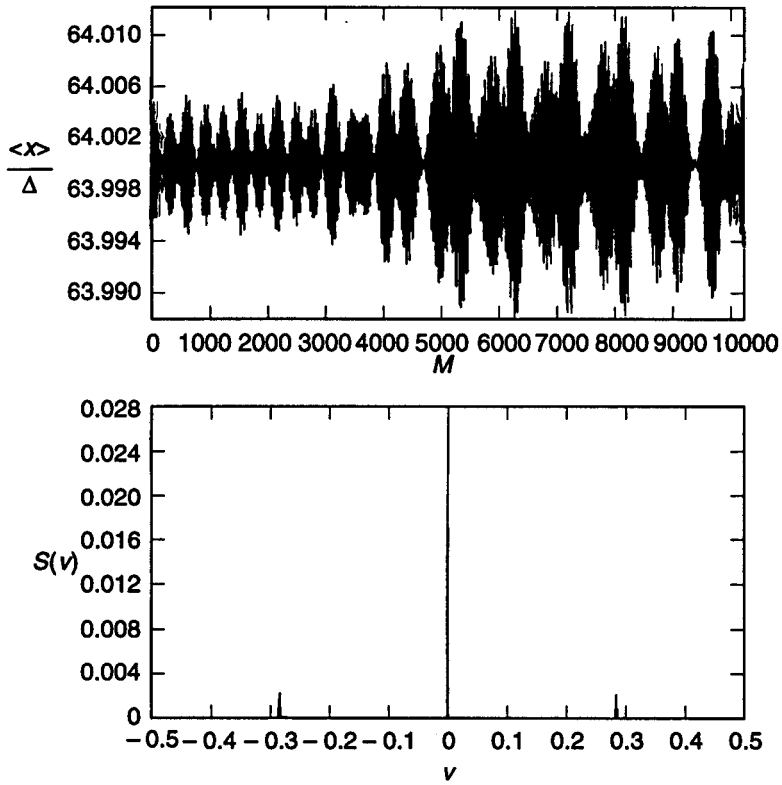

Figure 7.16. Beam Moment $< x >$ and Power Spectrum $S(\nu)$ for $M = 10,240$ Rotations at the Top and Bottom of the Figure, Respectively.

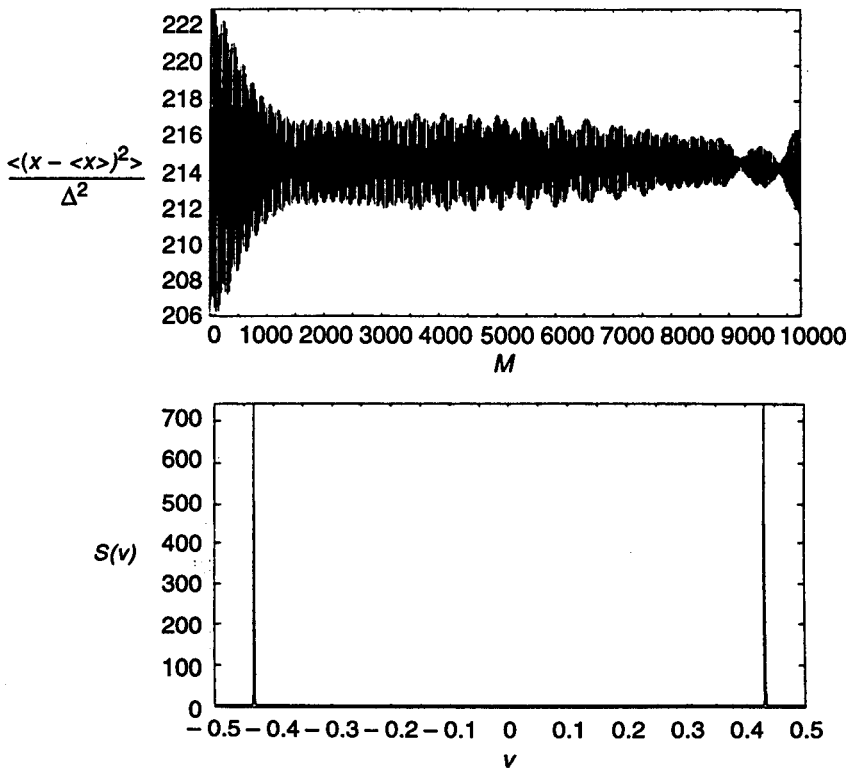

Figure 7.17. Beam Moment $< (x- < x >)^2 >$ and Power Spectrum $S(\nu)$ for $M = 10,240$ Rotations at the Top and Bottom of the Figure, Respectively.

The emittance ϵ of each beam for 10,240 rotations is shown in Figure 7.18. The emittance for one beam is at the top of the figure, and the other is at the bottom. Until about 6000 rotations the beams show similar behavior. They oscillate about the initial emittance $\epsilon_0 = 9.586\Delta$. After this the beams begin to deviate from one another. One beam is decreasing in phase space area, and the other beam is increasing. This phenomenon is similar to the "flip-flop" effect observed experimentally with equal-strength beams.[7] One beam blows up and the other decreases in size. The difference in ϵ is small between the two beams; by the end of the run it is $\delta\epsilon/\epsilon_0 = 4.4 \times 10^{-3}$. This variation in ϵ is very sensitive to the initial conditions. Figure 7.19 shows the emittance for both beams when the distribution is initialized with different random offsets in θ for the nonuniform charge distribution. The increments in r/σ are the same. The beams begin to deviate from one another at about 9000 rotations. The deviation is much smaller than the previous case. By the end of the run it is $\delta\epsilon/\epsilon_0 = 5 \times 10^{-4}$.

Runs with the uniform charge and nonuniform position initialization show different behavior than the runs with nonuniform charge and uniform position. Figure 7.20 shows the distribution of 10^4 particles in $(x/\sigma_x, p_x/\sigma_p)$ phase space for one beam after 10,240 rotations. The particles were initialized using the uniform charge distribution (Figure 6.7). After 10,240 rotations the particle distribution shows spiral arms in $(x/\sigma_x, p_x/\sigma_p)$ space. However, no dominant mode such as $m = 2$ (football shape) or $m = 4$ (square shape) has appeared that is distorting the shape of the whole beam. A profile in x of the distribution of particles in Figure 7.21 shows the deviation of the distribution from the initial Gaussian profile. The center of the beam is at $x = 64\Delta$. The profile is much smoother than the profile from the nonuniform charge distribution run (Figure 7.10).

Results from the least-squares-fit method for one beam are shown in Figure 7.22. The fit is done for small-amplitude particles $x < 0.1\sigma_x$. $\Delta\nu$ oscillates around the unperturbed tune-shift values of $\Delta\nu_0 = 2.1 \times 10^{-3}$ for small-amplitude particles. It is found that $\Delta\nu \approx 1.55 \times 10^{-3}$ for all the particles. The discrepancy is due to the drop-off of $\Delta\nu$ at large values of x. When all particles are included in the least-squares-fit, the measured $\Delta\nu$ is lowered by the particles with large x. The amplitude of the variation in $\Delta\nu$ for small-amplitude particles is approximately $\pm 3\%$ of $\Delta\nu_0$ near the end of the run, which is about a factor of 6 smaller than the deviations observed in the nonuniform charge run. The tune shift $\Delta\nu$ obtained from all particles decreases in amplitude with the number of rotations. The maximum variation of $\Delta\nu$ is approximately $\pm 3\%$ of its average value and occurs within the first 500 rotations. The oscillations in $\Delta\nu$ indicate that the expansion and contraction of the beam that is kicking the particles is smaller than the nonuniform charge runs.

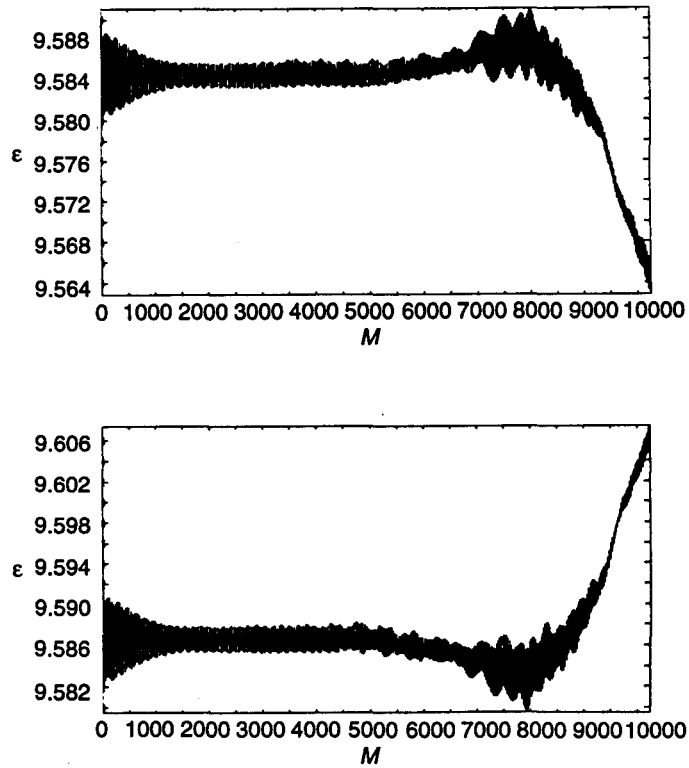

Figure 7.18. The Emittance ϵ of Both Beams for 10,240 Rotations. One beam is at the top and the other beam is at the bottom of the figure.

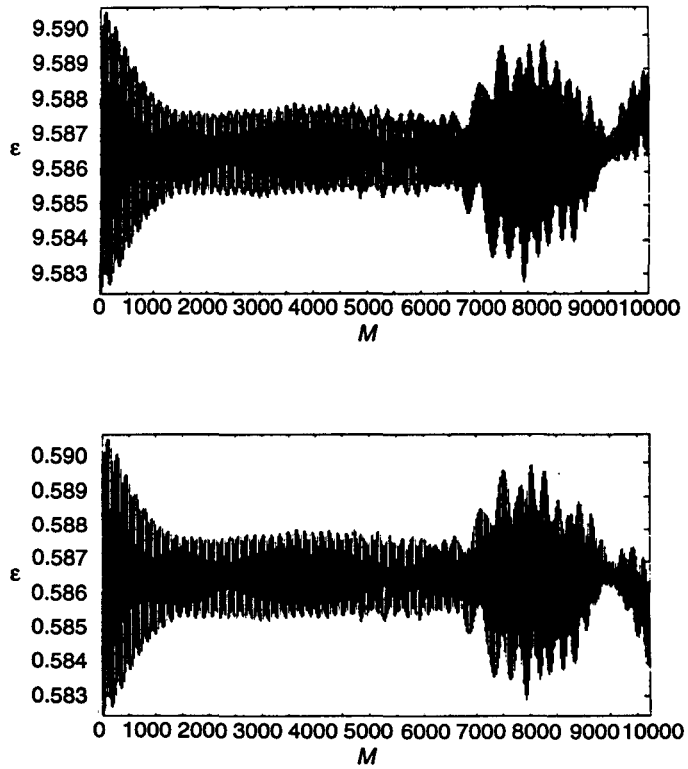

Figure 7.19. The Emittance ϵ of Both Beams for 10,240 Rotations with a Slightly Different Initialization. One beam is at the top and the other beam is at the bottom of the figure.

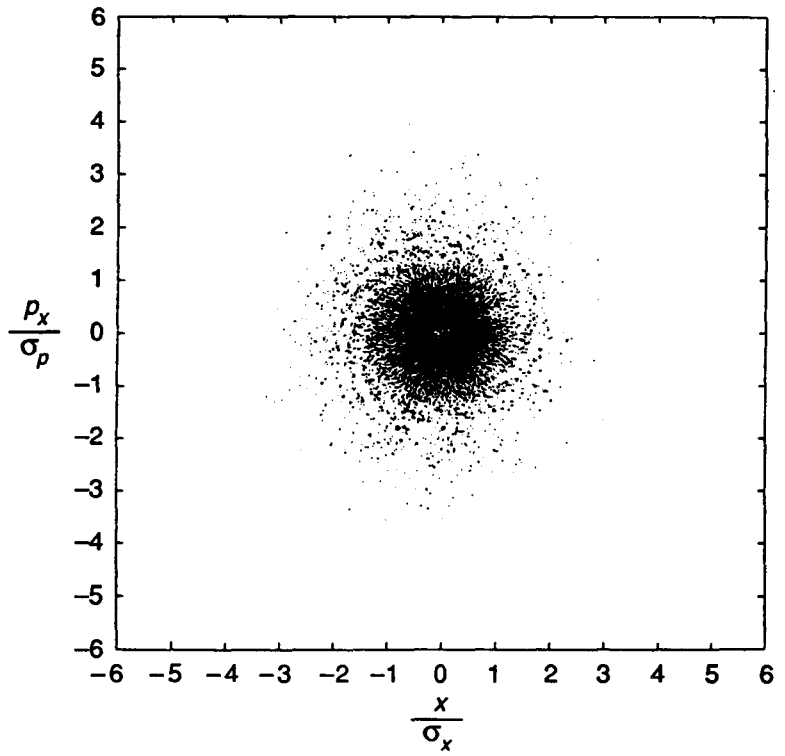

Figure 7.20. Distribution of 10^4 Simulation Particles in $(x/\sigma_x, p_x/\sigma_p)$ Space After 10,240 Rotations with $\nu_0 = 0.285$ and $\Delta\nu_0 = 2.1 \times 10^{-3}$.

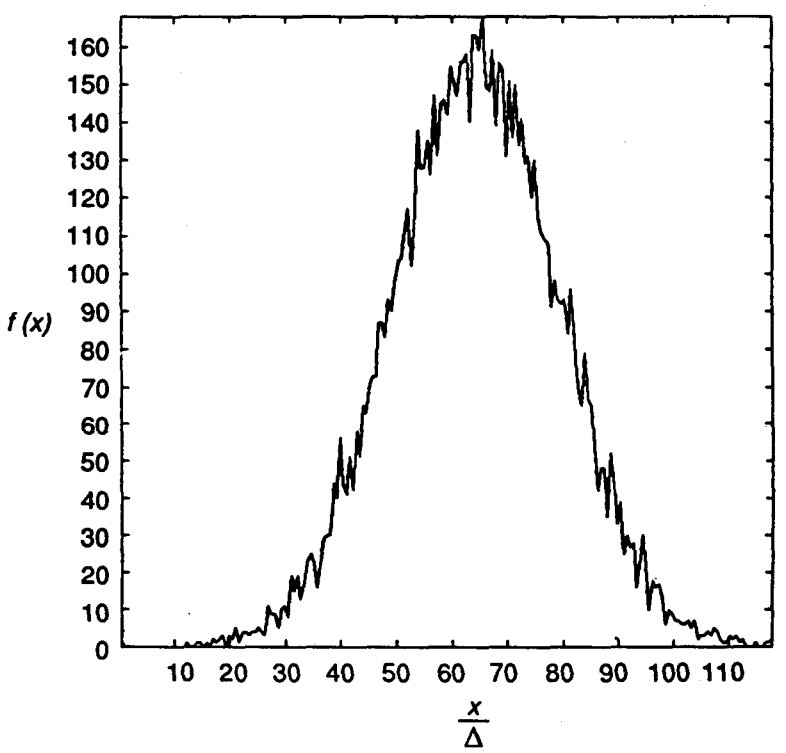

Figure 7.21. Distribution of 10^4 Simulation Particles in x After 10,240 Rotations with $\nu_0 = 0.285$ and $\Delta\nu_0 = 2.1 \times 10^{-3}$.

The emittance ϵ of each beam for 10,240 rotations is shown in Figure 7.23. The emittance for one beam is at the top of the figure, and the other is at the bottom. In this case the beams are oscillating in ϵ. The amplitude of the oscillations is largest for the first 1000 rotations. The magnitude of these oscillations is $\delta\epsilon/\epsilon_0 \approx 10^{-3}$, where ϵ_0 is the initial emittance. By the end of the run the oscillations are $\delta\epsilon/\epsilon_0 \approx 10^{-4}$.

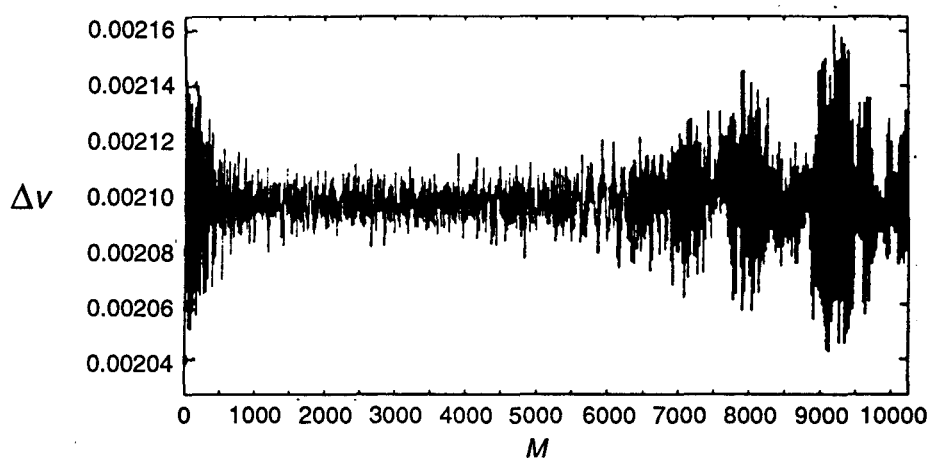

Figure 7.22. Tune Shift $\Delta\nu$ Measured from a Least-Squares-Fit to Small-Amplitude Particles $x < 0.1\sigma_x$ for $M = 10,240$ Rotations.

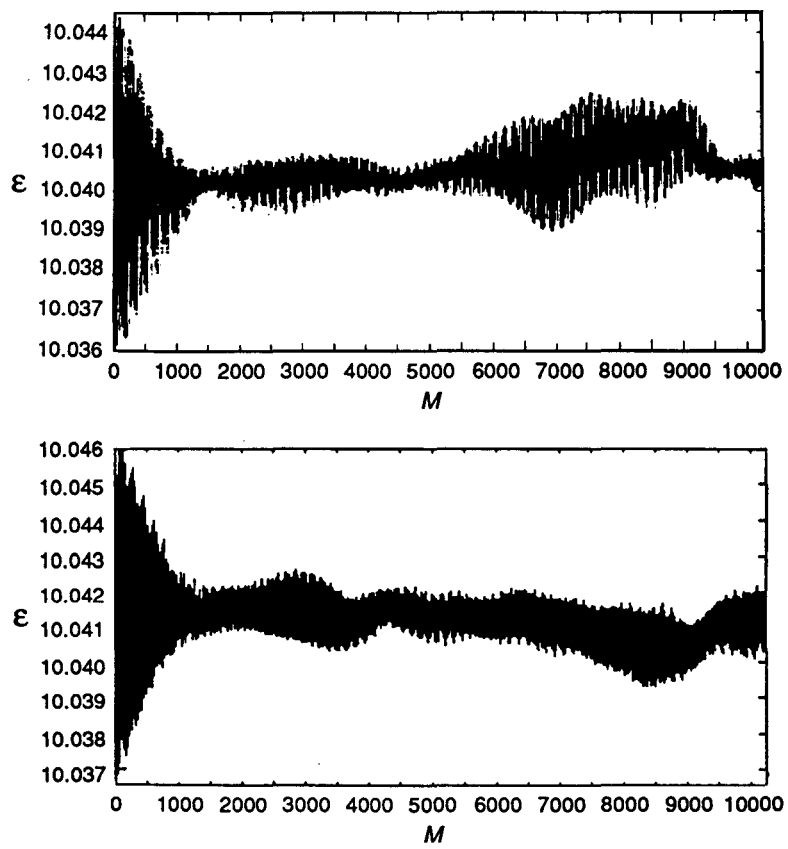

Figure 7.23. The Emittance ϵ of Both Beams for 10,240 Rotations. One beam is at the top and the other beam is at the bottom of the figure.

δf Simulation Results. A series of δf simulations has been performed to determine long time characteristics. We use 10^3 particles in the runs. The fluctuation level δ expected for the actual SSC beam is $\delta \approx 10^{-5}$ for 10^{10} particles. Figure 7.24 shows the variation with particle number of the minimum and maximum perturbations $\delta f/f_0$ for runs with 10,240 rotations. We see that the maximum perturbation is nearly independent of particle number. The minimum fluctuation value decreases exponentially with increasing particle number. It can be seen that the minimum perturbation drops below 10^{-5} for simulations with 10^3 particles and larger. Because 10^3 particles could be used, larger rotations of 10^5 could be run. The initial distribution of particles is shown in Figure 6.9. In this run 10^3 particles are used in each beam with variable charge per particle initially to maintain a Gaussian distribution. The tune $\nu_0 = 0.285$ and the tune shift $\Delta\nu_0 = 2.1 \times 10^{-3}$. The simulation box size is 128Δ, where Δ is the cell size. The beam width w is 30Δ and the particle size a is Δ. The particle size a is small enough in relation to the beam width w so that from Eq. (6.57):

$$\frac{\Delta\nu_{point}}{\Delta\nu_{fsp}} = 1.0022\,, \tag{7.9}$$

where $\Delta\nu_{point}$ is the tune shift for a point particle and $\Delta\nu_{fsp}$ is the tune shift for a finite-size particle. Thus, finite-size particle effects on the kicks that the simulation particles receive are minimal. By normalizing the code to a plasma with density lower than the beam, where ω_0 is the normalization plasma frequency and ω_b is the beam plasma frequency, only four simulation time steps are needed to cover the interaction region. Thus, $\omega_0\Delta t = 0.25$, where Δt is the simulation time-step size.

Figure 7.25 shows the distribution of 10^3 particles in $(x/\sigma_x, p_x/\sigma_p)$ phase space for one beam after 10^5 rotations. After 10^5 rotations the particles are no longer uniformly distributed in $(x/\sigma_x, p_x/\sigma_p)$ space. Some clumping of particles has occurred, and small regions contain no particles. The clumping is not significant enough to affect the validity of the constant phase space density assumption as a good approximation. A profile in x of a Gaussian distribution of particles in Figure 7.26 is shown. Figure 7.27 shows the perturbations from the δf code to the Gaussian profile after 10^5 rotations. The center of the beam is at $x = 64\Delta$. The maximum perturbations are only 0.1% of the maximum in the Gaussian profile. Thus, the δf code is still a valid approximation. Notice that the perturbed distribution makes sense physically. There is a depletion of particles from the center of the beam and an increase in particles at about $\pm 2\sigma_x$. The beam is expanding slightly.

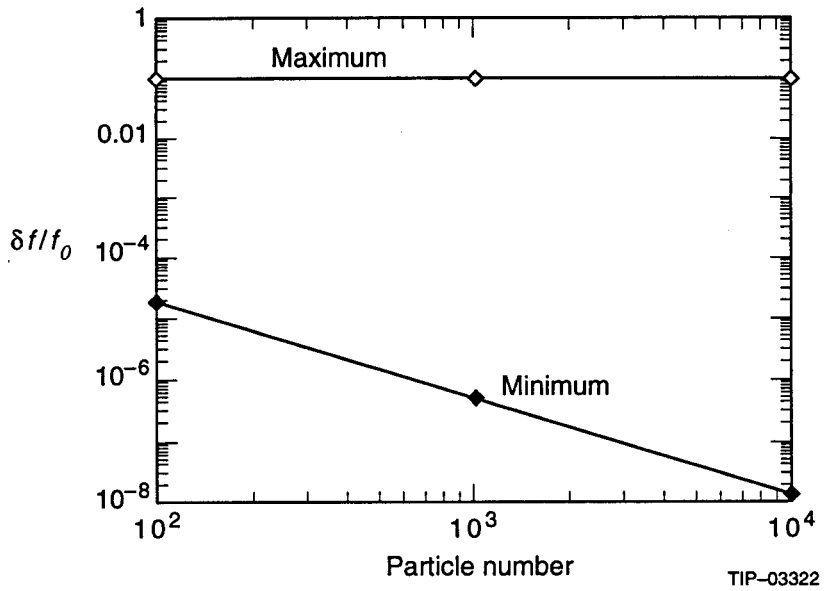

Figure 7.24. The Minimum and Maximum Perturbation Values $\delta f/f_0$ for $M = 10,240$ Rotations, $\nu_0 = 0.285$, and $\Delta\nu_0 = 2.1 \times 10^{-3}$.

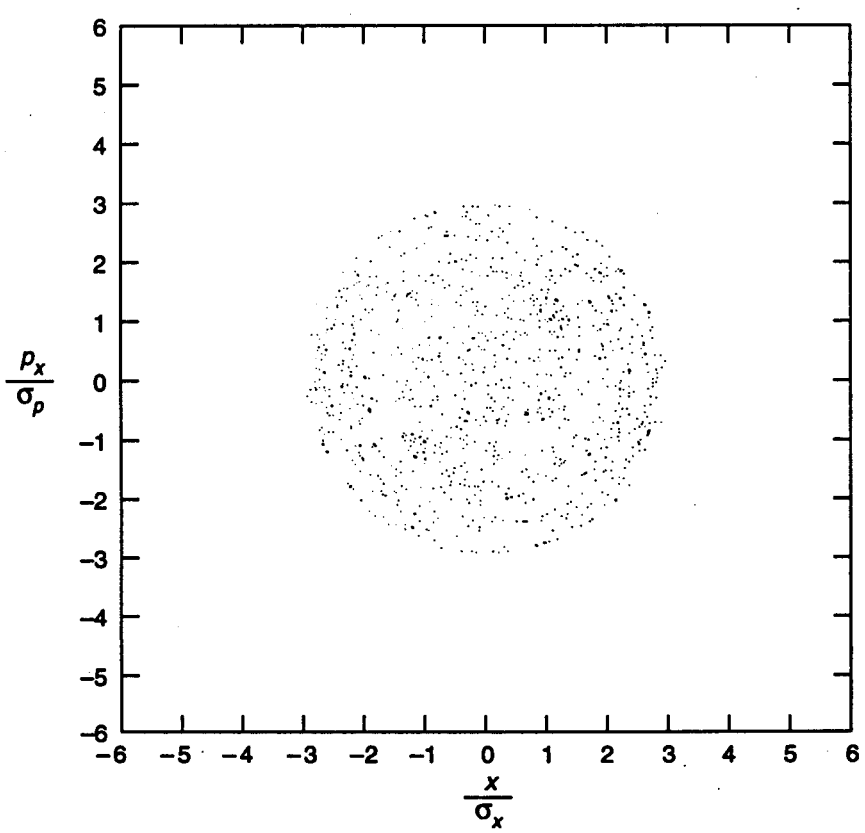

Figure 7.25. Distribution of 10^3 Simulation Particles in $(x/\sigma_x, p_x/\sigma_p)$ Space After 10^5 Rotations with $\nu_0 = 0.285$ and $\Delta\nu_0 = 2.1 \times 10^{-3}$.

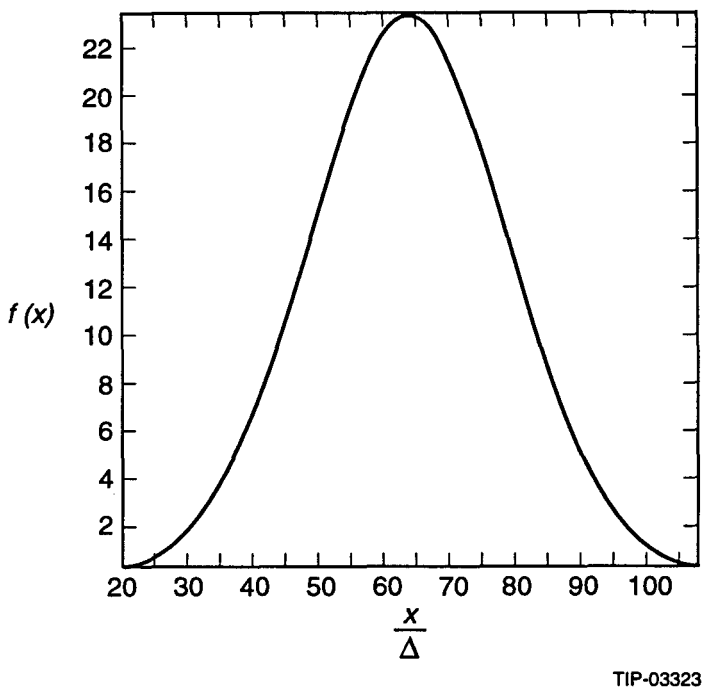

Figure 7.26. Gaussian Steady-State Distribution.

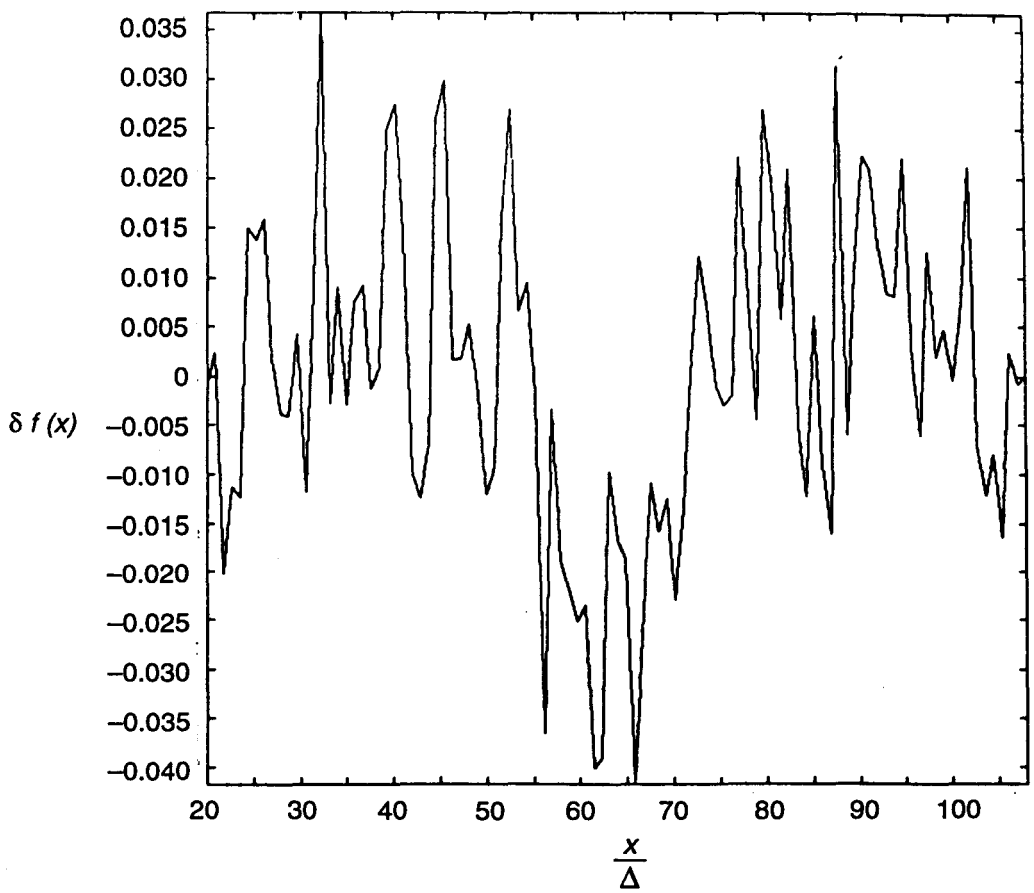

Figure 7.27. Distribution of 10^3 δf Simulation Particles Including the Particle Weights in x After 10^5 Rotations with $\nu_0 = 0.285$ and $\Delta\nu_0 = 2.1 \times 10^{-3}$.

Results from the least-squares-fit method for one beam are shown in Figure 7.28. The fit is done for small-amplitude particles $x < 0.1\sigma_x$ at the top of the figure and for the entire beam at the bottom of the figure. The tune shift $\Delta\nu$ oscillates around the unperturbed values of $\Delta\nu_0 = 2.1 \times 10^{-3}$ for small-amplitude particles and $\Delta\nu_0 \approx 1.52 \times 10^{-3}$ for all the particles. The discrepancy is due to the drop-off of $\Delta\nu$ at large values of x. The amplitude of the variation in $\Delta\nu$ for small-amplitude particles is approximately $\pm 3\%$ of $\Delta\nu_0$ throughout the run. The tune shift obtained from all particles increases in amplitude with the number of rotations until approximately 15,000 rotations; it then remains somewhat constant until the end of the run. The maximum variation of $\Delta\nu$ is approximately $\pm 4\%$. The oscillations in $\Delta\nu$ indicate expansion and contraction of the beam that is kicking the particles. Notice that the beam that is kicking the particles is expanding and contracting differently at different particle positions. The small-amplitude portion of the beam is at constant oscillation amplitude, while the entire beam is increasing in oscillation amplitude for the first 15,000 rotations.

The other method by which the tune shift $\Delta\nu$ is measured is by obtaining power spectra of the x positions of sample particles that are sampled once every complete rotation. Figure 7.29 shows the shift in the power spectral peak from 100 particle positions in phase space. The tune shift $\Delta\nu$ is measured from the shift in the power spectral peak from the unperturbed tune ν_0. Notice that $\Delta\nu$ decreases with increasing r/σ of the sample particle, where $r/\sigma = \sqrt{x^2/\sigma_x^2 + p_x^2/\sigma_p^2}$.

Moments of one beam and their associated power spectra $S(\nu)$ are shown in Figures 7.30, 7.31, 7.32, and 7.33. At the top of Figure 7.30 the oscillation of the average beam center $< x >$ is apparent. The beam oscillates with a maximum beam amplitude of $\delta x/\sigma_x \approx \pm 1.6 \times 10^{-4}$. The average $< x >$ and $< (x - < x >)^3 >$ (Figure 7.32), the odd moments, are both increasing in oscillation amplitude with rotation number. At the top of Figure 7.31 the oscillation of the beam width can be seen. The beam is oscillating about the initial beam width σ_x^2 with a maximum amplitude of approximately $\pm 0.003\sigma_x^2$. Oscillations are also apparent for $< (x - < x >)^4 >$ at the top of Figure 7.33. These oscillations are induced spontaneously. This is in spite of the initial lack of offset and initial lack of noise due to the finite number of particles. The latter is due to our adoption of the δf algorithm. The particle weights w_i were taken to be zero at $t = 0$.

The bottoms of Figures 7.30, 7.31, 7.32, and 7.33 show the moments and their associated power spectra. The power spectrum of the average of x, $< x >$, is shown at the bottom of Figure 7.30. There are peaks in $S(\nu)$ in descending power at $\nu \approx \pm\nu'$ and $\pm(5\nu' - 1)$, where $\nu' = \nu_0 - \Delta\nu_0$. These peaks correspond to harmonics of the betatron motion. In Figure 7.31 the peaks in the power spectrum $S(\nu)$ at $\nu \approx \pm(1 - 2(\nu_0 - \Delta\nu_0))$ also correspond to the betatron motion of the beam. The peak near $\nu \approx 0$ corresponds to low-frequency oscillations with periods longer than 10^4 rotations. Figure 7.32 shows $S(\nu)$ for $< (x- < x >)^3 >$. The peaks in $S(\nu)$ in descending power are at $\pm(5\nu' - 1)$, $\nu \approx \pm\nu'$, $\pm(1 - 3\nu')$, and $\pm(2 - 7\nu')$, where $\nu' = \nu_0 - \Delta\nu_0$. Similarly, in Figure 7.33, $S(\nu)$ for $< (x- < x >)^4 >$ has peaks in descending power at $\pm(1 - 2\nu')$ and $\pm(1 - 4\nu')$, where $\nu' = \nu_0 - \Delta\nu_0$. As in the case with $< (x- < x >)^2 >$, there is a low-frequency peak with oscillations having time scales longer than 10^4 rotations. It appears from these results that the even beam moments contain more power in the low-frequency components of $S(\nu)$ than do the odd beam moments.

The discrepancy between the odd and even moments is also indicative in the mode expansions of the beam distributions. Figures 7.34 and 7.35 show the variations of the odd and even modes, respectively, with rotation number. The modes are calculated from Eq. (6.159) in Section 6.5.3 for $m = 1$ to $m = 6$. As in the calculation of moments, the odd modes $m = 1, 3, 5$ are increasing with rotation number (Figure 7.34). The intensity $f(m)$ of the odd modes also increases with mode number m. The even modes $m = 2, 4, 6$ oscillate about an average throughout the entire run. The oscillation amplitude decreases with mode number m. The overall intensity $f(m)$ of the even modes is about a factor of 10 higher than that of the odd modes.

The emittance ϵ of each beam for 10^5 rotations is shown in Figure 7.36. The emittance for one beam is at the top of the figure, and the other is at the bottom. The beams show similar behavior through the 10^5 rotations. They expand and contract in phase space simultaneously. The maximum expansion is about $\delta\epsilon/\epsilon_0 \approx 2 \times 10^{-3}$.

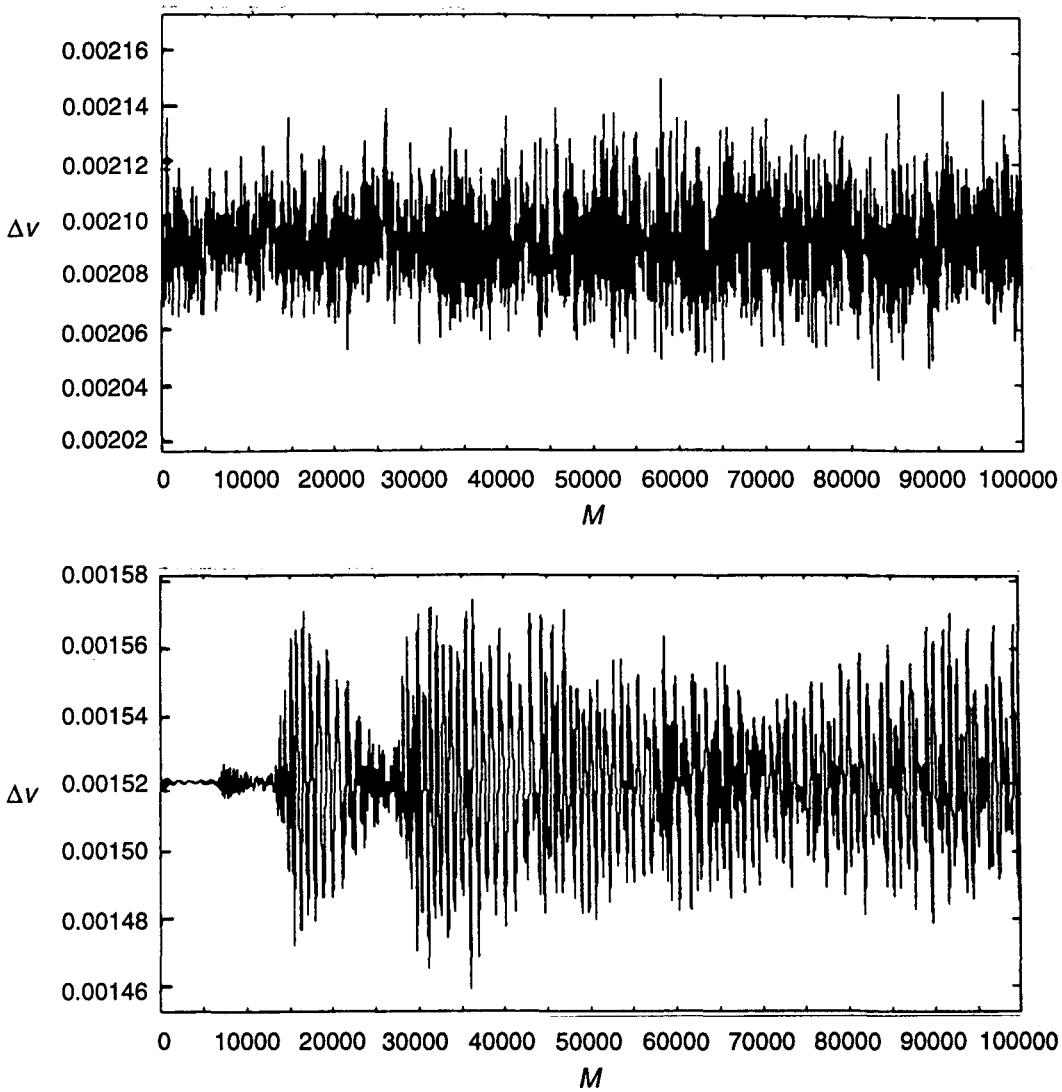

Figure 7.28. Tune Shift $\Delta\nu$ Measured from a Least-Squares-Fit to Small-Amplitude Particles $x < 0.1\sigma_x$ (Top) and All Particles (Bottom) for $M = 10,240$ Rotations.

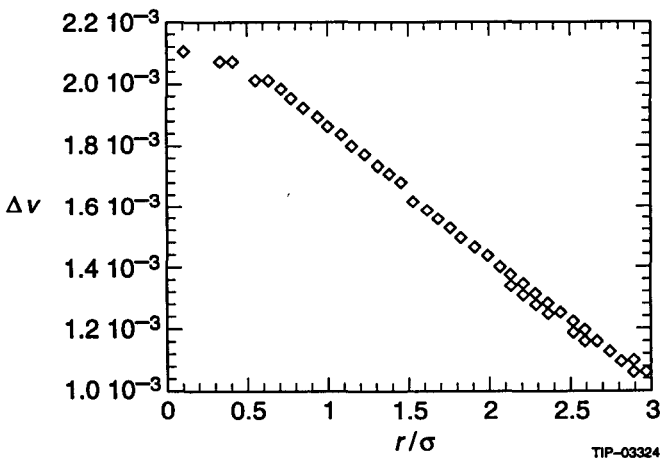

Figure 7.29. The Tune Shift $\Delta\nu$ Measured from the Shift in the Power Spectral Peaks of the x Positions of 100 Sample Particles After $M = 10^5$ Rotations.

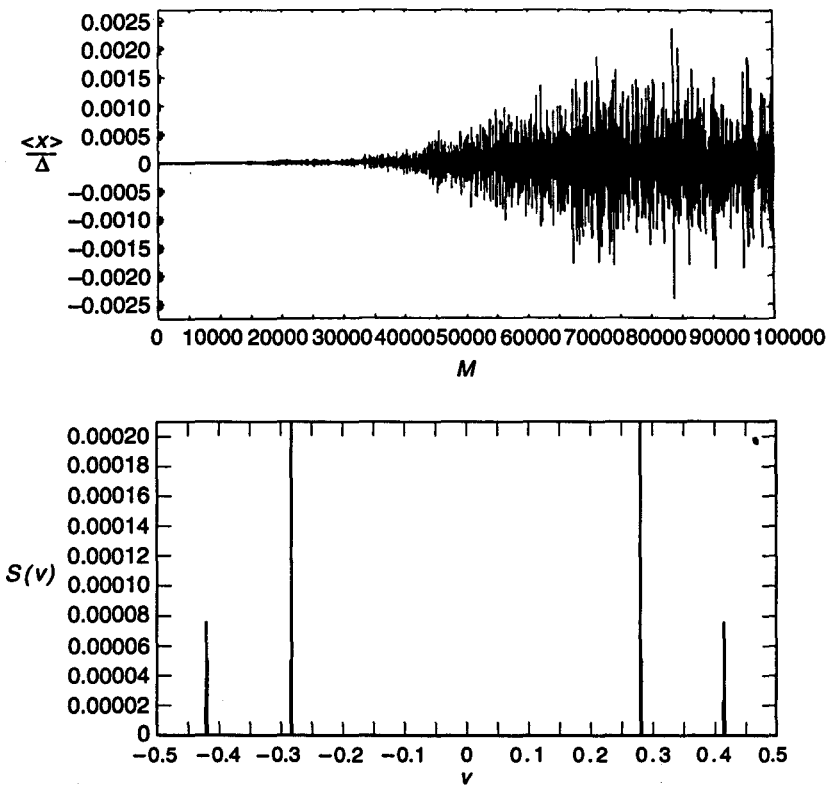

Figure 7.30. Beam Moment $< x >$ and $S(\nu)$ for $M = 10^5$ Rotations at the Top and Bottom of the Figure, Respectively.

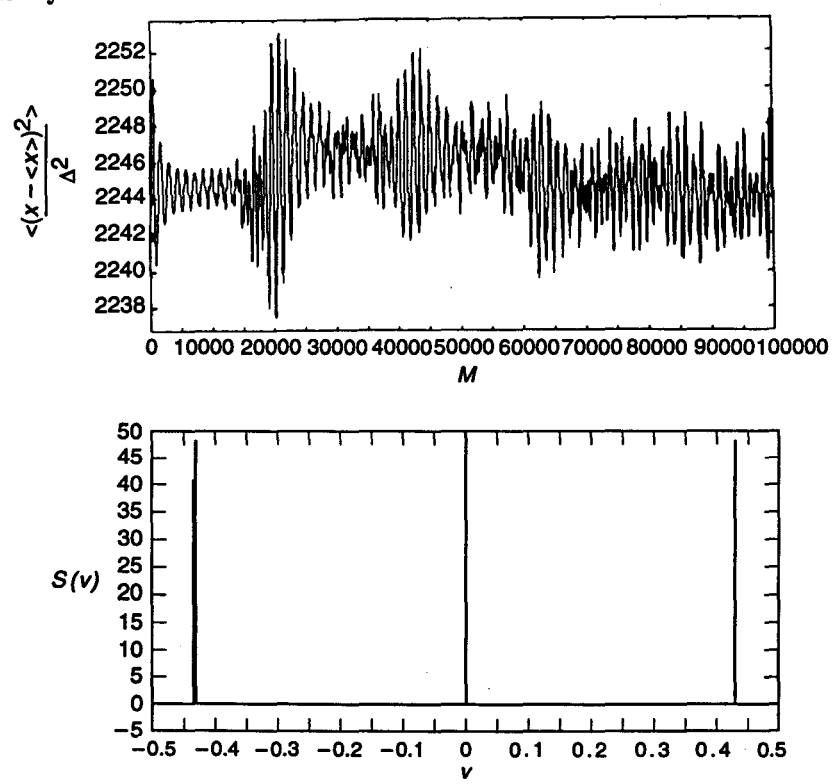

Figure 7.31. Beam Moment $< (x- < x >)^2 >$ and $S(\nu)$ for $M = 10^5$ Rotations at the Top and Bottom of the Figure, Respectively.

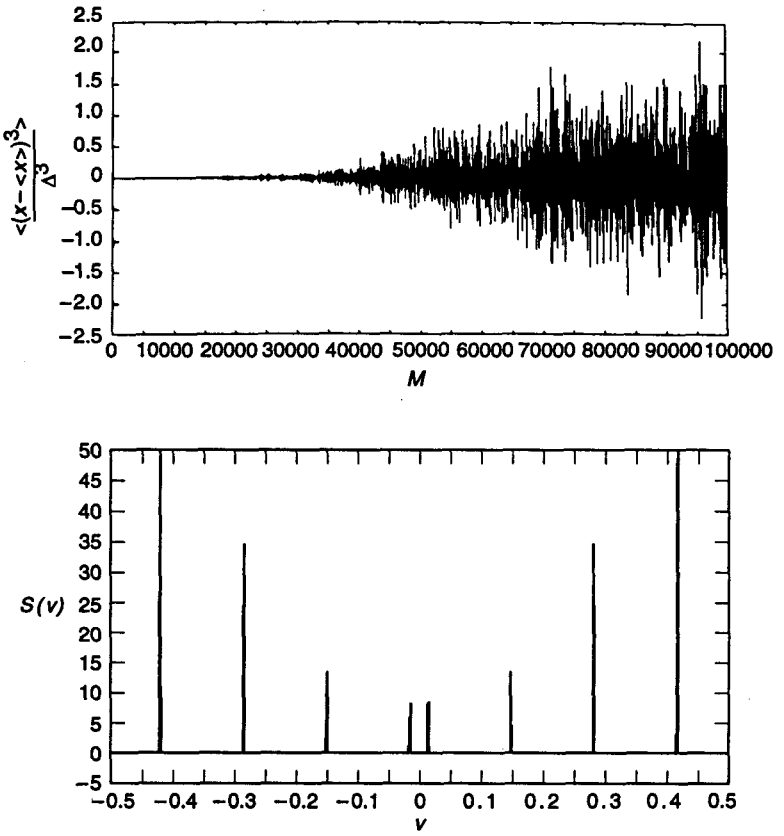

Figure 7.32. Beam Moment $< (x- < x >)^3 >$ and $S(\nu)$ for $M = 10^5$ Rotations at the Top and Bottom of the Figure, Respectively.

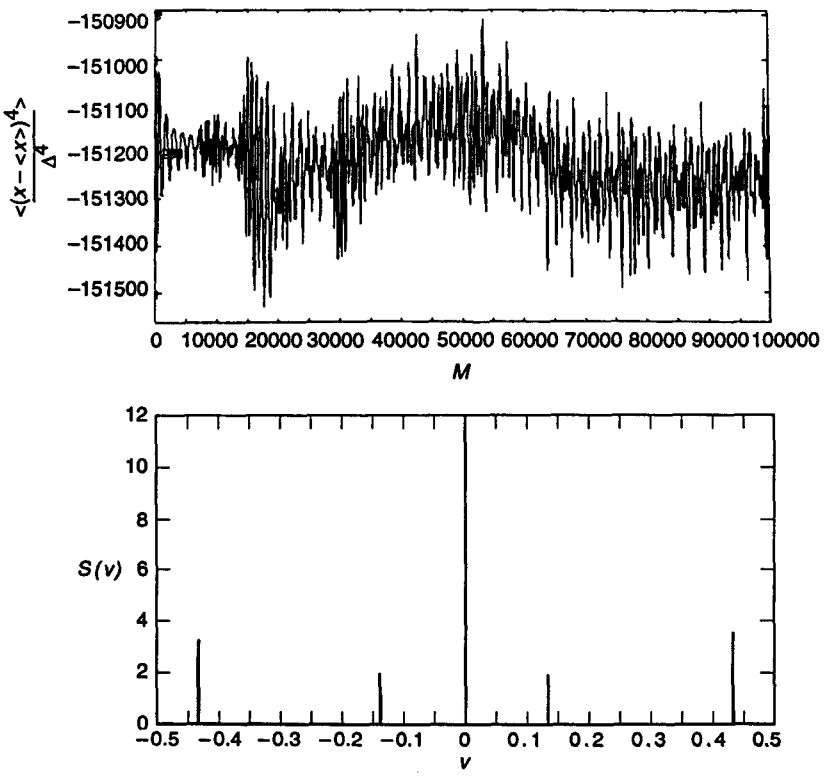

Figure 7.33. Beam Moment $< (x- < x >)^4 >$ and $S(\nu)$ for $M = 10^5$ Rotations at the Top and Bottom of the Figure, Respectively.

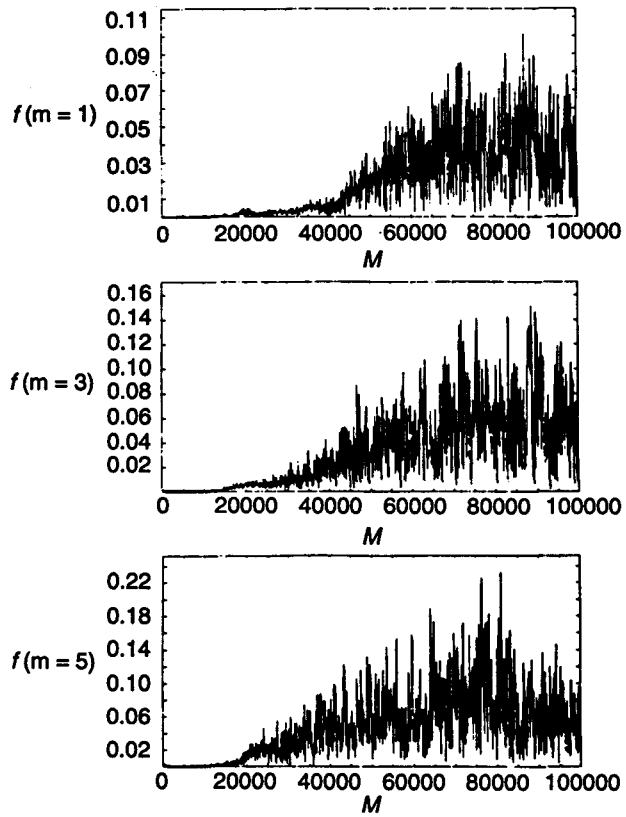

Figure 7.34. Odd Modes $m = 1, 3, 5$ Down the Figure of the Distribution of Particles for $M = 10^5$ Rotations.

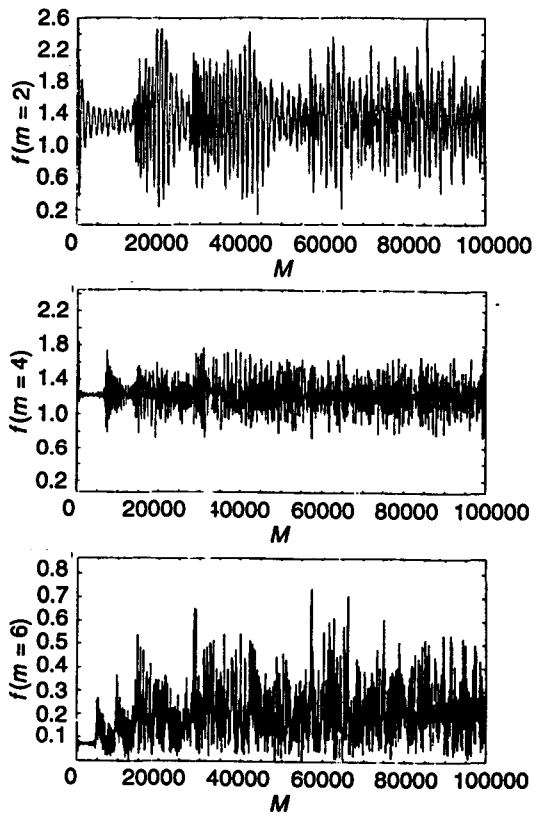

Figure 7.35. Even Modes $m = 2, 4, 6$ Down the Figure of the Distribution of Particles for $M = 10^5$ Rotations.

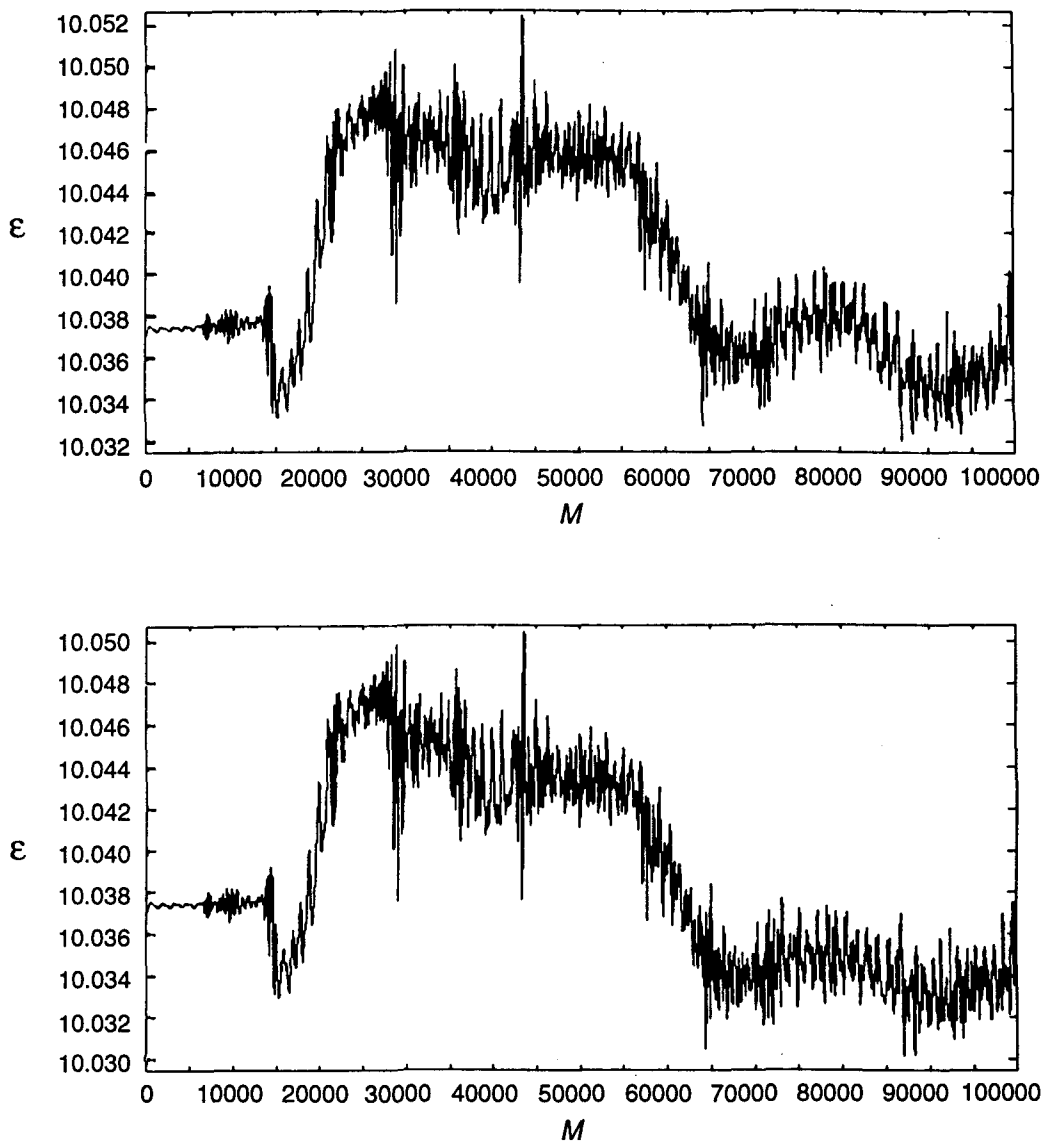

Figure 7.36. The Emittance ϵ of Both Beams for 10^5 Rotations. One beam is at the top and the other beam is at the bottom of the figure.

7.2.2 $\nu_0 - \Delta\nu_0$ Stability

In this section we examine the variation of beam stability with tune ν_0 and tune shift $\Delta\nu_0$. The strong-strong PIC simulation code is employed exclusively here. Although the δf code is quieter, it is not well-suited for studying beam blowup phenomena that distort the original distribution by a significant amount.

Figure 7.37 shows a stability diagram of $\Delta\nu_0$ versus ν_0. The dotted lines are obtained from a linear theory developed by Chao and Ruth.[18] The lines demarcate regions of linear stability and instability for equal charge beams. The stable regions are those regions contained by the dotted lines. The lines plotted are for up to eight beam modes. As is the

general case with any linear theory, the theory can predict the initial growth rates of the instability, but not the saturation levels. The points in Figure 7.37 represent strong-strong simulation code results, in which the unperturbed $\Delta\nu_0$ and ν_0 are varied. The unperturbed tune shift $\Delta\nu_0$ is scanned between the SSC reference value of 2.1×10^{-3} and a maximum value of 0.04. In each of the simulations 10^4 simulation particles are used. The codes are run for 10^4 rotations, with the exception of one run that is run for 3×10^4 rotations. All the runs are initialized with variable charge and uniform distribution. All other parameters are the same as previous strong-strong simulation runs. Beam stability for various values of $\Delta\nu_0$ and ν_0 is determined from emittance growth. If the emittance of the beams ϵ increases by 50%, then the run is designated unstable. The marginally stable case noted in Figure 7.37 is determined from the emittance growth after 30,000 rotations.

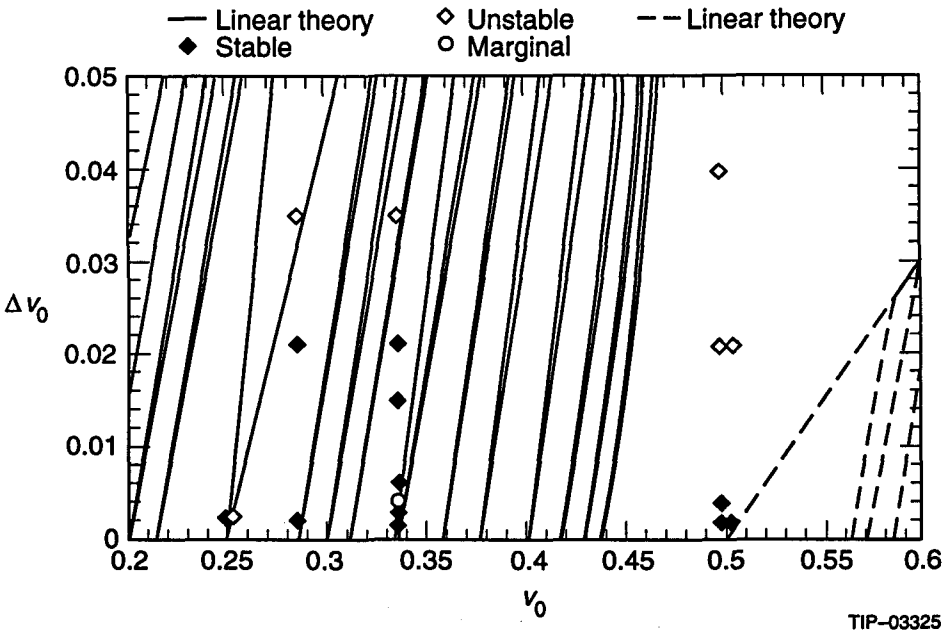

Figure 7.37. $\nu_0 - \Delta\nu_0$ Stability Diagram.

The results from the simulations show good agreement with the linear theory of Chao and Ruth.[18] The beams are unstable in regions of instability and are stable in regions of stability.

We examine in more detail the cases where $\Delta\nu_0$ is small. In this case similarly charged beams with values of the unperturbed tune ν_0 just above a resonance are kicked towards the resonance by the beam-beam interaction. In this case the beams are expected to be unstable. For beams with values of ν_0 just below a resonance, the beam-beam kick is away from the resonance and the beams are expected to be stable. Beam blowup due to strong resonance is observed just above $\nu_0 = 1/2$ and $\nu_0 = 1/4$ for values of $\Delta\nu_0 = 2.1 \times 10^{-3}$.

Figures 7.38 and 7.39 show the phase space distribution of the simulation particles. In Figure 7.38 phase space plots show simulation results around the $\nu_0 = 1/2$ resonance. At the top of Figure 7.38, where $\nu_0 = 1/2 + \Delta\nu_0$, the beam blows up. At the bottom of Figure 7.38, where $\nu_0 = 1/2 - \Delta\nu_0$, it is seen that mode 2 dominates the shape of the beam in phase space (football shape). In Figure 7.39 phase space plots show simulation results around the $\nu_0 = 1/4$ resonance. At the top of Figure 7.39, where $\nu_0 = 1/4 + \Delta\nu_0$, the beam particles are clumping, and the emittance is observed to increase by more than 50%. At the bottom of Figure 7.39, where $\nu_0 = 1/4 - \Delta\nu_0$, it is mode 4 that dominates (square shape). The beams in the case of $\nu_0 = 1/2 + \Delta\nu_0$ blow up very quickly. It takes only a few hundred rotations. The beams blow up more slowly for $\nu_0 = 1/4 + \Delta\nu_0$. This behavior is expected. Higher-order resonances have lower growth rates of instability. The beams are stable just below $\nu_0 = 1/2$ and $\nu_0 = 1/4$ for small values of $\Delta\nu_0$.

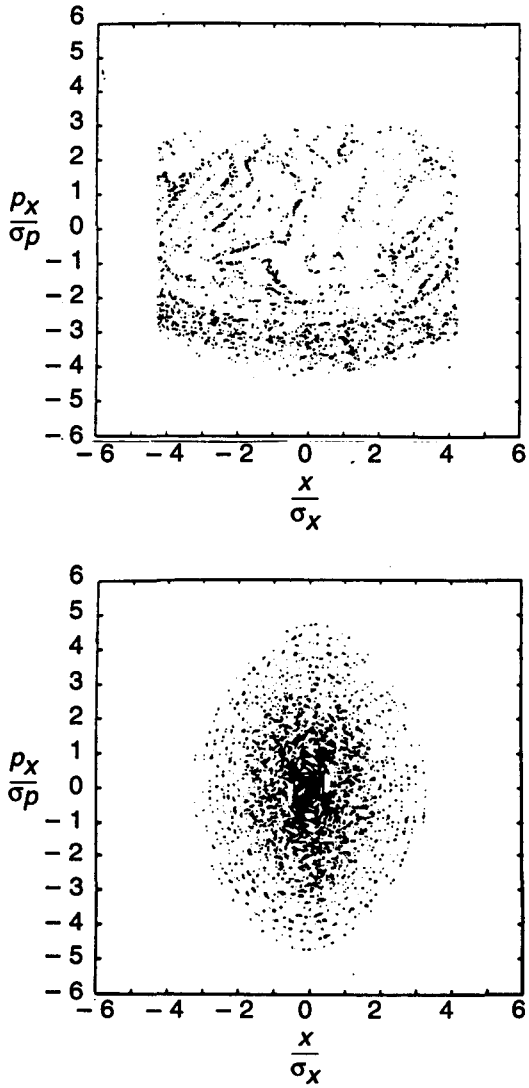

Figure 7.38. $(x/\beta^*, x')$ Distribution of Particles for $\nu_0 = 1/2 + \Delta\nu_0$ (Top) and $\nu_0 = 1/2 - \Delta\nu_0$ (Bottom), Where $\Delta\nu_0 = 2.1 \times 10^{-3}$.

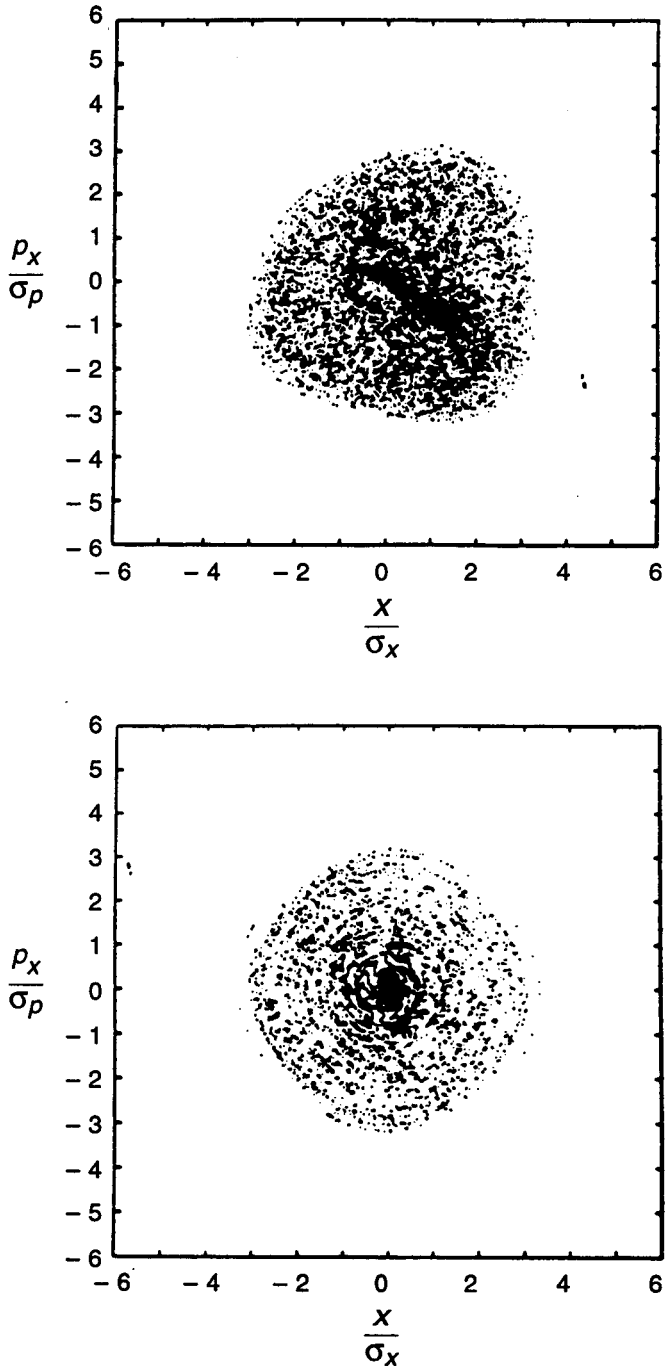

Figure 7.39. $(x/\beta^*, x')$ Distribution of Particles for $\nu_0 = 1/4 + \Delta\nu_0$ (Top) and $\nu_0 = 1/4 - \Delta\nu_0$ (Bottom), Where $\Delta\nu_0 = 2.1 \times 10^{-3}$.

A point is scanned just above $\nu_0 = 1/3$ with $\nu = \nu_0 + \Delta\nu_0$, where $\Delta\nu_0 = 4 \times 10^{-3}$. In this case the emittance ϵ is slowly growing (Figure 7.40). The beam emittance ϵ keeps growing until approximately 24,000 rotations, after which it appears to saturate until the end of the run at 30,000 rotations. The phase space distribution of one beam is shown in Figure 7.41. It can be seen that mode 6 is beginning to slowly dominate the distribution. Since two (*i.e.*, an even number of) beams are colliding, mode 2/6 is expected to dominate for $\nu_0 = 1/3 + \Delta\nu_0$. Since this is a high-order mode, the slow growth rate is expected.

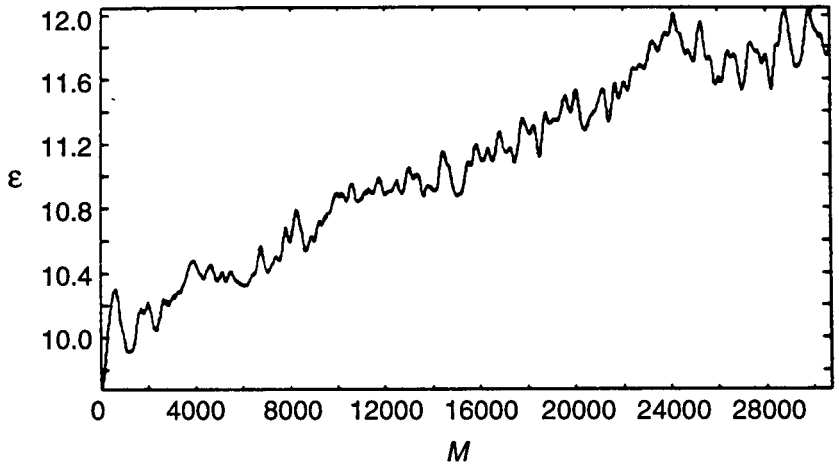

Figure 7.40. Emittance as a Function of Rotations for ν_0 Just Above 1/3.

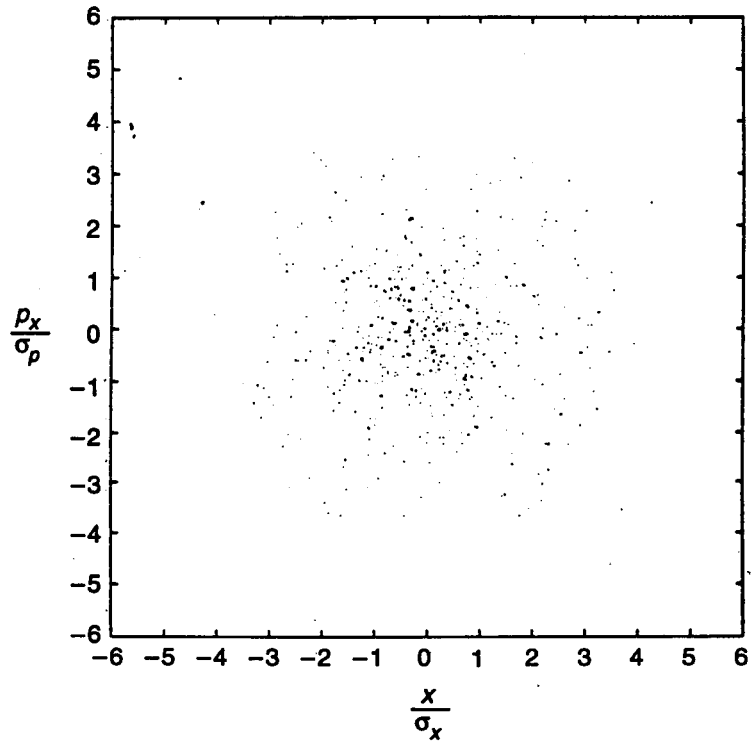

Figure 7.41. $(x/\beta^*, x')$ Distribution of Particles for $\nu_0 = 1/3 + \Delta\nu_0$, Where $\Delta\nu_0 = 2.1 \times 10^{-3}$.

7.3 Particle Diffusion

In this section we examine particle diffusion brought about by the beam-beam interaction. The diffusion is measured from the tracking code, the strong-strong code, and the δf code. We compare the diffusion coefficients measured for each of these runs. Of the three codes, the δf code gives the best representation. It is quieter than the PIC code and allows degrees of freedom of evolution from the initial distribution that are not permitted in the tracking code. We use the two methods described in Section 6.5.4 to measure particle diffusion.

7.3.1 Tracking Code Results

We first examine particle diffusion for particles tracked using the $1-D$ tracking code describe in Section 6.1.

Reference parameters described in Section 7.2.1 for the SSC are used: the tune $\nu_0 = 0.285$ and the tune shift $\Delta\nu_0 = 2.1 \times 10^{-3}$. The initial particle positions are shown in Figure 7.42. The Poincare map of two sample particles is shown after 10^5 rotations in Figure 7.43. The particles are sampled once every complete rotation. They show little diffusive motion. The circles that each particle traces out in phase space are due to the betatron motion of the particles.

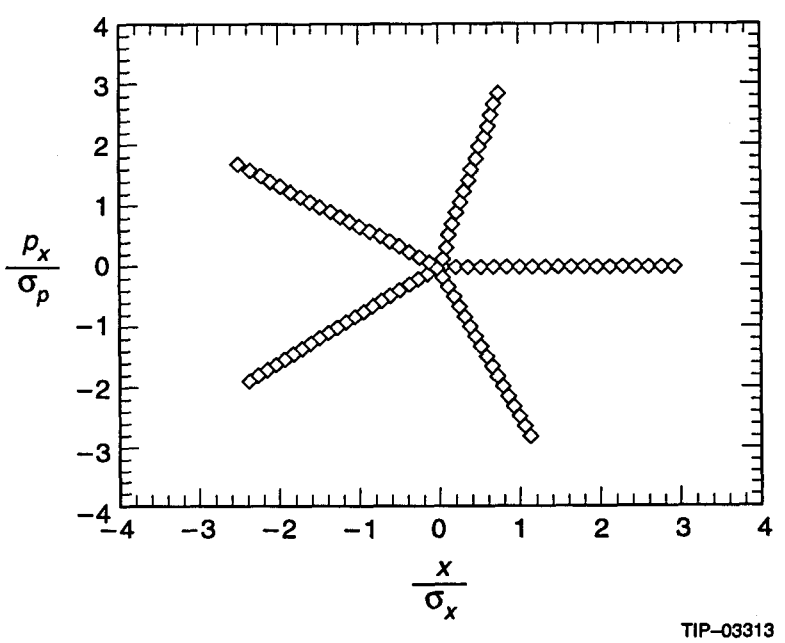

Figure 7.42. Initial Particle Positions for 100 Tracking Code Particles in $(x/\sigma_x, p_x/p)$ Phase Space.

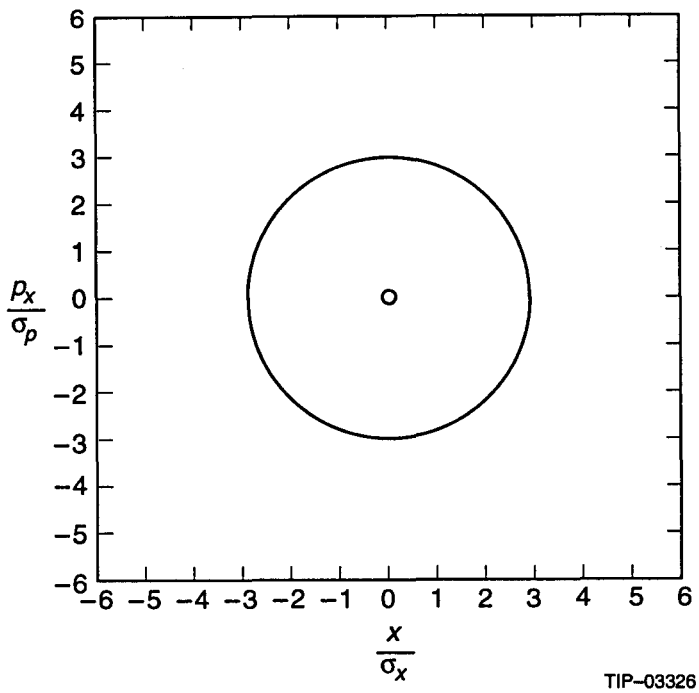

Figure 7.43. Poincare Section in $(x/\sigma_x, p_x/\sigma_p)$ Space of Small- and Large-Amplitude Tracking Code Particles After $M = 10^5$ Rotations.

A better grasp of the diffusive motion of the sample particles can be obtained from their diffusion coefficients. The diffusion coefficients, df1 and df2, calculated after 10,240 rotations, are shown in Figure 7.44, where

$$\frac{r}{\sigma} = \sqrt{\frac{x}{\sigma_x}^2 + \frac{p_x}{\sigma_p}^2} \tag{7.10}$$

is the distance in phase space from the center of the beam. The D_x means that df1 and df2 are calculated for diffusion in position $|x|$ from Eq. (6.161). The diffusion is normalized to σ_x^2/N_r, where N_r is the number of rotations. In Figure 7.44 it is apparent from the fact df1 >> df2 that the motion is largely oscillatory in phase space. The coefficients calculated over two time scales differ on average by a factor of approximately 100. This is expected for oscillatory motion, where

$$\begin{aligned} \frac{\text{df2}}{\text{df1}} &\propto \left(\frac{\Delta N_1}{\Delta N_2}\right)^3 \\ &\propto \frac{1}{1000}. \end{aligned} \tag{7.11}$$

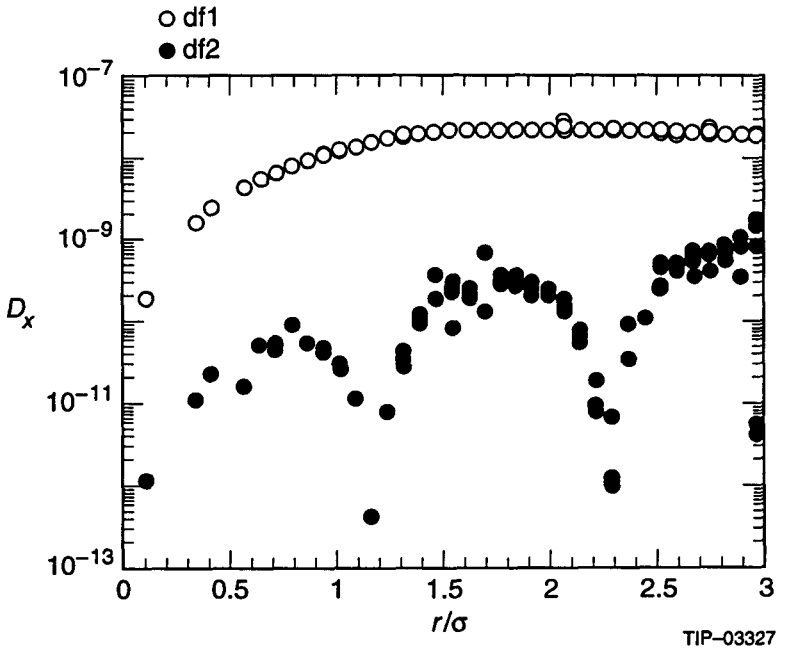

Figure 7.44. D_x from the Tracking Code with $\Delta\nu_0 = 2.1 \times 10^{-3}$ and $\nu = 0.285$ for $M = 10,240$ Rotations. df1 and df2 have time scales of $\Delta N_1 = 102$ and $\Delta N_2 = 1024$ rotations, respectively.

Figures 7.45 and 7.46 show the diffusion coefficients calculated for $M = 40,960$ and $M = 10^5$ rotations, respectively. The average diffusion rate is decreasing with increasing rotations. The range of coefficients for 40,960 rotations is 10^{-9}–10^{-14}, and for 10^5 rotations it is 10^{-10}–10^{-15}. This drop with increasing rotation number is another indication that the particle motion is still oscillatory and not diffusive. If the particles are diffusive, the diffusion coefficients would settle down to values independent of the time scale. There are some points between $r/\sigma = 1.5$ and $r/\sigma = 2$ that meet the criteria for diffusivity. That is, df1 $\approx$ df2. However, most of the coefficients differ by a factor of approximately 100. So, in tracking code simulations a majority of the particles exhibit oscillatory motion at different values of position x up to 10^5 rotations.

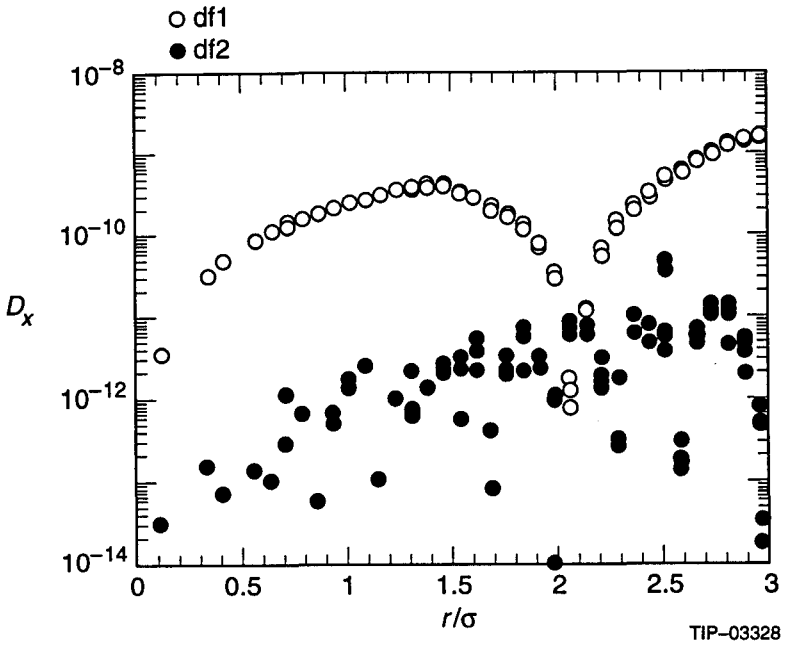

Figure 7.45. D_x from the Tracking Code with $\Delta\nu_0 = 2.1 \times 10^{-3}$ and $\nu = 0.285$ for $M = 40,960$ Rotations. df1 and df2 have time scales of $\Delta N_1 = 409$ and $\Delta N_2 = 4096$ rotations, respectively.

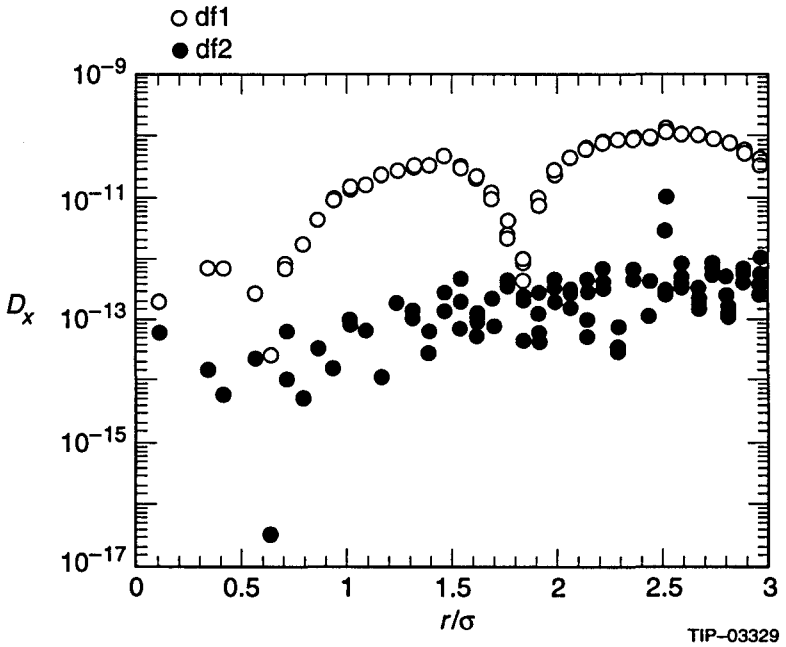

Figure 7.46. D_x from the Tracking Code of the Beam with $\Delta\nu_0 = 2.1 \times 10^{-3}$ and $\nu = 0.285$ for $M = 10^5$ Rotations. df1 and df2 have time scales of $\Delta N_1 = 1000$ and $\Delta N_2 = 10,000$ rotations, respectively.

7.3.2 Strong-Strong Simulation Results

In this section results from the strong-strong code on particle diffusion are presented. The effects of the particle initialization method are examined, and the results are compared with the tracking code. Again reference parameters described in Section 7.2.1 for the SSC are used. So the tune $\nu_0 = 0.285$ and the tune shift $\Delta\nu_0 = 2.1 \times 10^{-3}$.

Results from the strong-strong code with variable charge per particle are shown in Figure 7.47. Each beam in the simulation has 10^4 simulation particles, with the initial distribution in (x, p_x) phase space shown in Figure 6.5 and the resulting profile shown in Figure 6.88.

The Poincare map of two sample particles after 10,240 rotations is shown in Figure 7.48. The particles are sampled once every complete rotation. Diffusion is apparent for both particles, even after only 10,240 rotations. The small-amplitude particle, especially, shows the smearing out of the ring observed from the tracking-code Poincare map (Figure 7.43). The diffusion coefficients are calculated for 100 sample particles after 10,240 rotations. The initial particle positions are the same as the tracking code shown in Figure 7.42. As in the tracking code results in the previous section, the diffusion coefficients, df1 and df2, are calculated at various $|x|$ in Eq. (6.161). The diffusion D_x is normalized to σ_x^2/N_r, where N_r is the number of rotations. The diffusion coefficients differ substantially from those obtained from the tracking code (Figure 7.44). All the particles in this case show the diffusive nature. D_x is uniform across the beam radial position and is nearly an order of magnitude higher than the tracking code values. Some of this diffusiveness is from fluctuations due to the finite number of particles of the strong-strong code. This dependence is shown in Figures 7.49 and 7.50. These figures show the diffusion coefficients, df1 and df2, for two different particles after 1000 rotations. One is for a sample particle at $r/\sigma = 0.1$ (Figure 7.49), and the other is for a sample particle at $r/\sigma = 0.9$ (Figure 7.50). In both figures the solid lines and the dashed lines refer to the diffusion coefficients, df1 and df2, respectively, calculated from a tracking code. Note that the tracking code values are independent of the number of particles, since the field is calculated from one Gaussian particle ("strong beam"). Both plots show a reduction in the diffusion coefficient for the strong-strong code calculated on the longer time scale (df2). It is more apparent for the particle at $r/\sigma = 0.1$ (Figure 7.49). The reduction goes as $1/\sqrt{N}$, where N is the number of particles. This $1/\sqrt{N}$ dependence shows that finite particle fluctuation noise,[36,37] which goes as $1/\sqrt{N}$, is contributing to the diffusion of the sample particles.

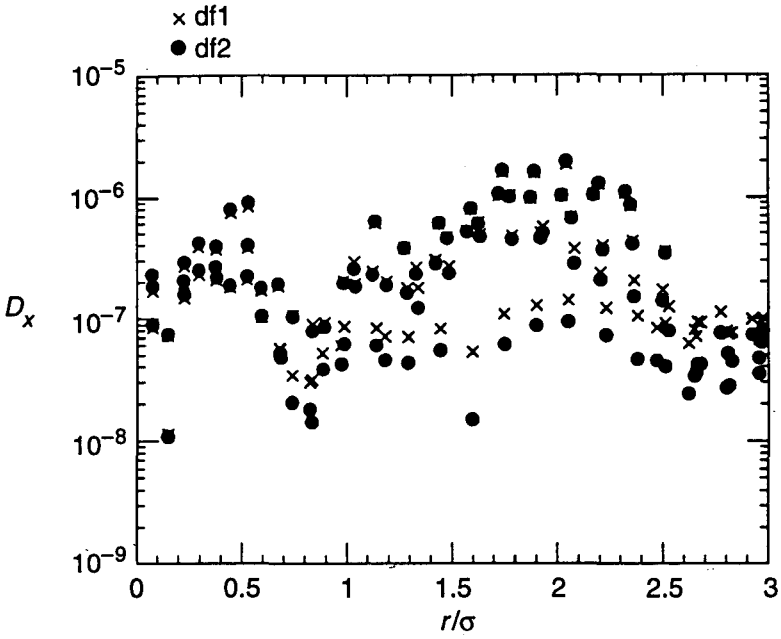

Figure 7.47. D_x from the Strong-Strong Code with $\Delta\nu_0 = 2.1 \times 10^{-3}$ and $\nu = 0.285$ for $M = 10,240$ Rotations. df1 and df2 have time scales of $\Delta N_1 = 102$ and $\Delta N_2 = 1024$ rotations, respectively.

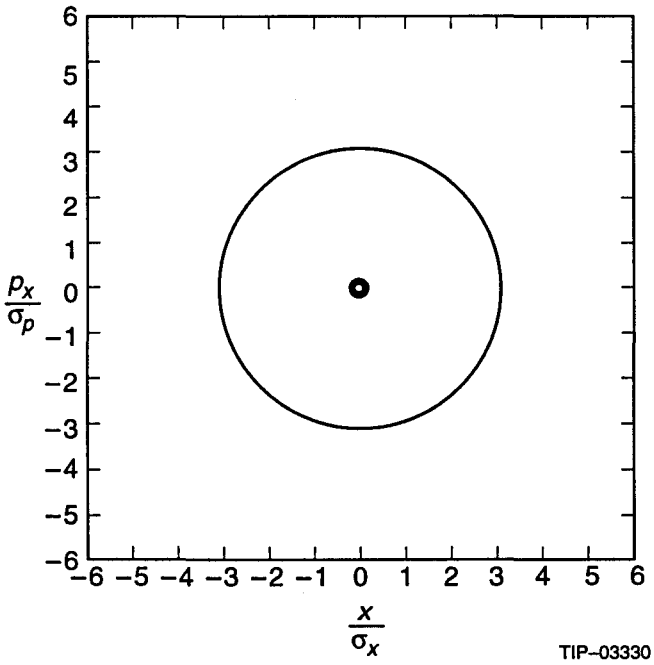

Figure 7.48. Poincare Section in $(x/\sigma_x, p_x/\sigma_p)$ Space of Small- and Large-Amplitude Strong-Strong Code Particles After $M = 10,240$ Rotations.

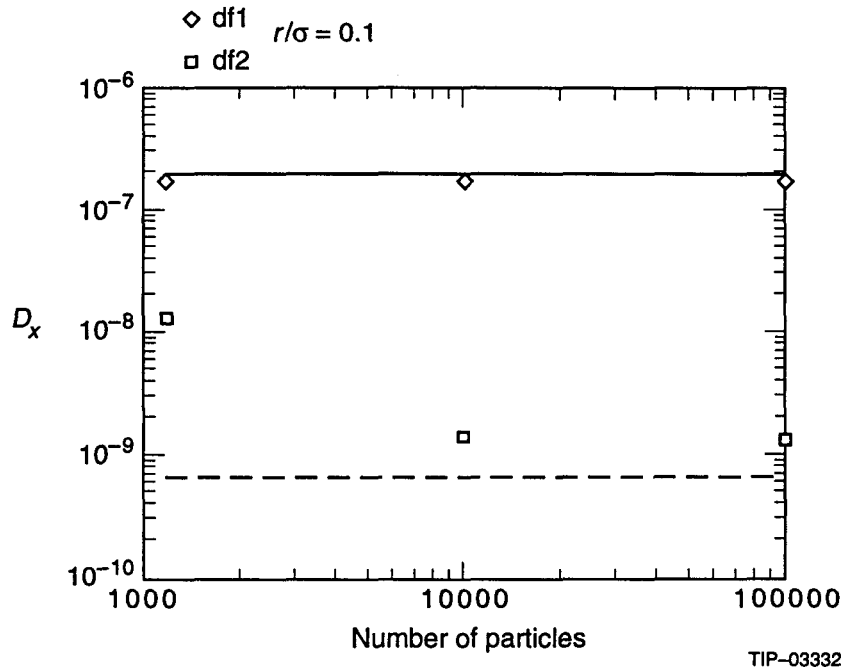

Figure 7.49. D_x Versus Particle Number for a Sample Particle at $r/\sigma = 0.1$ for $M = 1000$ Rotations. df1 and df2 have time scales of $\Delta N_1 = 10$ and $\Delta N_2 = 100$ rotations, respectively.

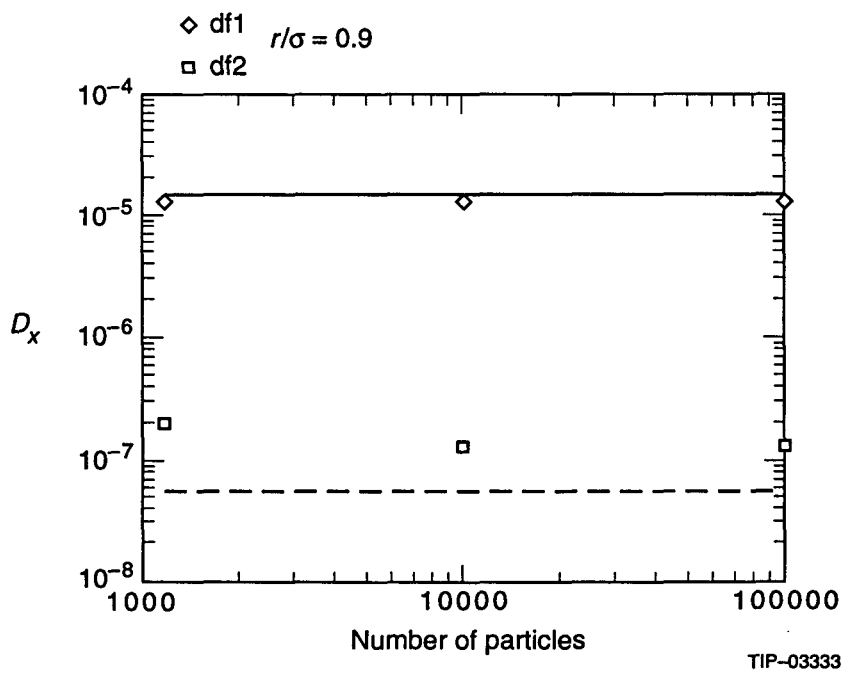

Figure 7.50. D_x Versus Particle Number for a Sample Particle at $r/\sigma = 0.9$ for $M = 1000$ Rotations. df1 and df2 have time scales of $\Delta N_1 = 10$ and $\Delta N_2 = 100$ rotations, respectively.

In order to reduce the fluctuation noise, we use the nonuniform particle initialization method described in Section 6.3.3. The simulation particles are given equal charge and are nonuniformly distributed in (x, p_x) phase space (Figure 6.7). The resulting profile in x is shown in Figure 6.8 for 10,000 simulation particles. SSC reference parameters are used, with $\nu_0 = 0.285$ and $\Delta\nu_0 = 2.1 \times 10^{-3}$. The initial positions in $(x/\sigma_x, p_x/\sigma_p)$ phase space of the 100 sample particles are shown in Figure 7.51. The nonuniform initialization of the simulation particles does make a difference in the finite particle fluctuation noise level. The Poincare map of two sample particles after 10,240 rotations is shown in Figure 7.52, where the particles are sampled once every complete rotation. Diffusion is apparent for both sample particles. However, the smearing seen for the small amplitude is much less than that observed with the nonuniform charge particle initialization (Figure 7.47).

The reduced diffusion is evident in Figure 7.53, where the variable charge and uniform charge diffusion coefficients are shown for $M = 10,240$ rotations. The uniform charge initialization is much quieter. It shows oscillatory particle motion for particles with $r/\sigma < 2$. The only particles that exhibit diffusive characteristics are those particles with $r/\sigma > 2$—that is, particles in the tails of the distribution. In comparison with the tracking code the sample particles from the uniform charge initialization show more diffusive behavior (Figure 7.54). The agreement is good between the tracking code and strong-strong code for the shorter time scale diffusion coefficient, df1, for values of $r/\sigma < 2$. However, the longer time scale diffusion coefficient for the uniform particle initialization shows higher values for all values of r/σ, especially in the tail of the distribution.

It has been shown that finite particle fluctuation noise plays a role in the diffusion of particles in the strong-strong simulations. This noise can be somewhat offset by using quieter particle initialization schemes such as the smooth charge loading scheme. However, there are still significant differences from the tracking code. Although the strong-strong code should show differences from the tracking code because of the self-consistent solution of the fields, it is difficult to determine whether the differences observed are due to particle fluctuation noise alone. In order to get a better grasp of the effects of this fluctuation noise, the noisy tracking code described in Section 6.3.4 is used. Figure 7.55 shows the results for 10,240 rotations where noise added to the tracking code is of the form described in Section 6.3.4. The noise level δ is determined by

$$\delta = \frac{1}{\sqrt{N(x)}}, \tag{7.12}$$

where $N(x) = N\mathrm{erf}(x/\sqrt{2}\sigma_x)$ and N is the particle number. Notice that the small-amplitude particles at $r/\sigma = 0.1$ are diffusive for the noisy tracking code and the PIC code. The larger-amplitude particles at $r/\sigma = 0.9$ are both oscillatory. The PIC code

is more diffusive than the noisy tracking code at $r/\sigma = 0.1$ and is less oscillatory than the noisy tracking code at $r/\sigma = 0.9$. These results indicate that some of the diffusion observed in the PIC code is from finite particle noise. The discrepancy in the diffusion coefficients between the PIC code and the noisy tracking code may be due to other types of numerical noise or collective phenomena.

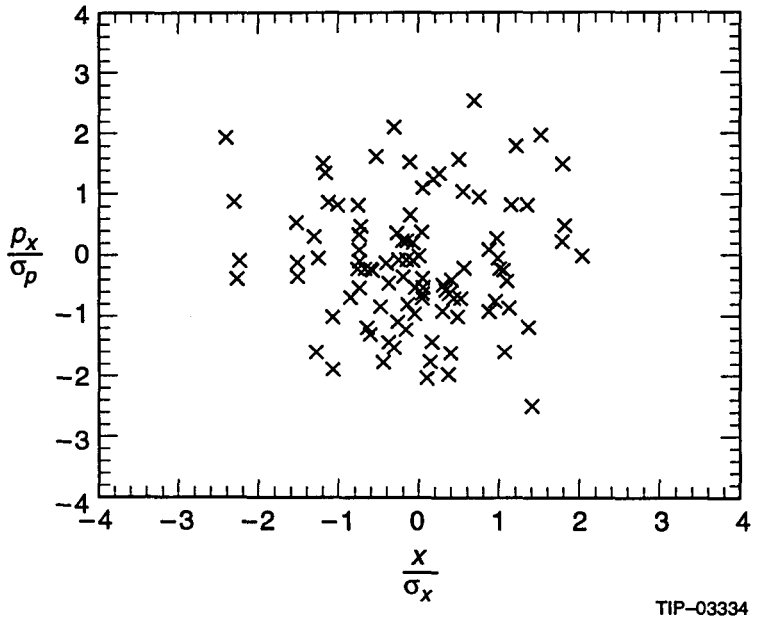

Figure 7.51. Initial Particle Positions for 100 Strong-Strong Sample Particles in $(x/\sigma_x, p_x/p)$ Phase Space.

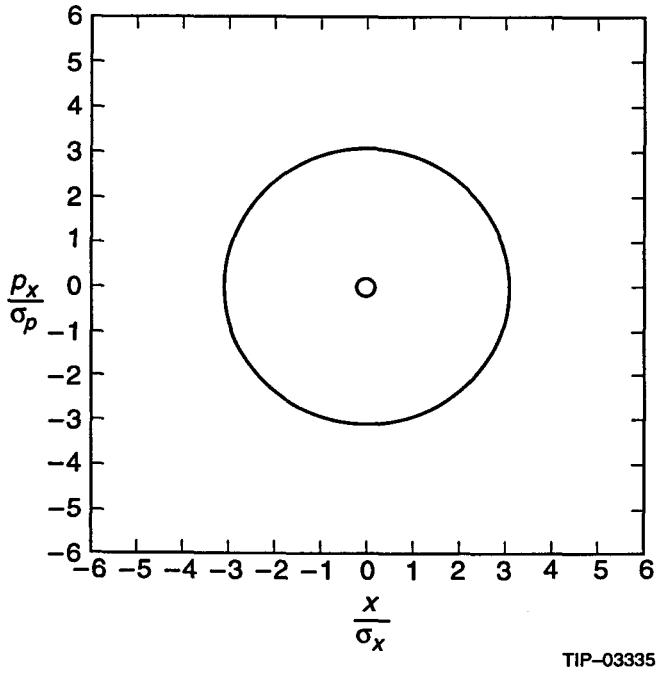

Figure 7.52. Poincare Section in $(x/\sigma_x, p_x/\sigma_p)$ Space of Small- and Large-Amplitude Strong-Strong Code Particles with Uniform Charge After $M = 10,240$ Rotations.

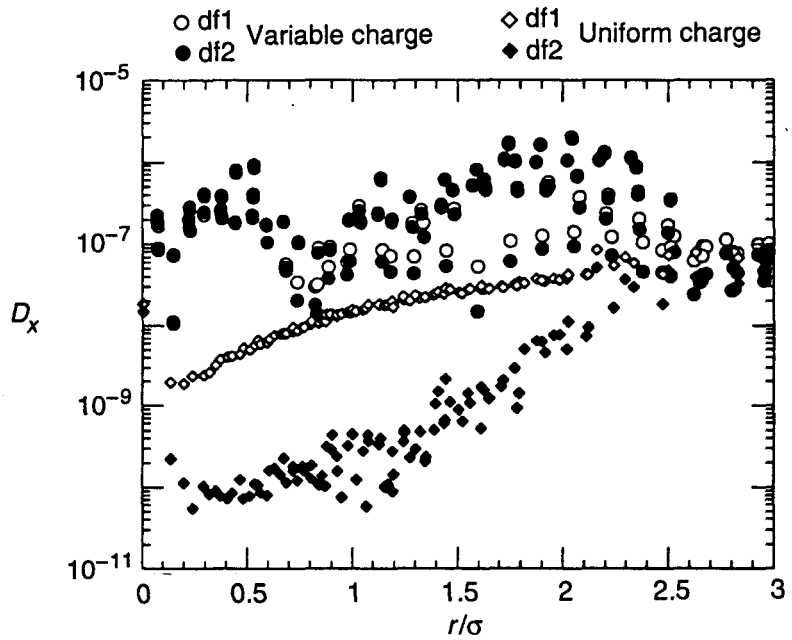

Figure 7.53. D_x from the Strong-Strong Code with the Variable Charge and Uniform Charge Particle Initialization for $M = 10,240$ Rotations. df1 and df2 have time scales of $\Delta N_1 = 102$ and $\Delta N_2 = 1024$ rotations, respectively.

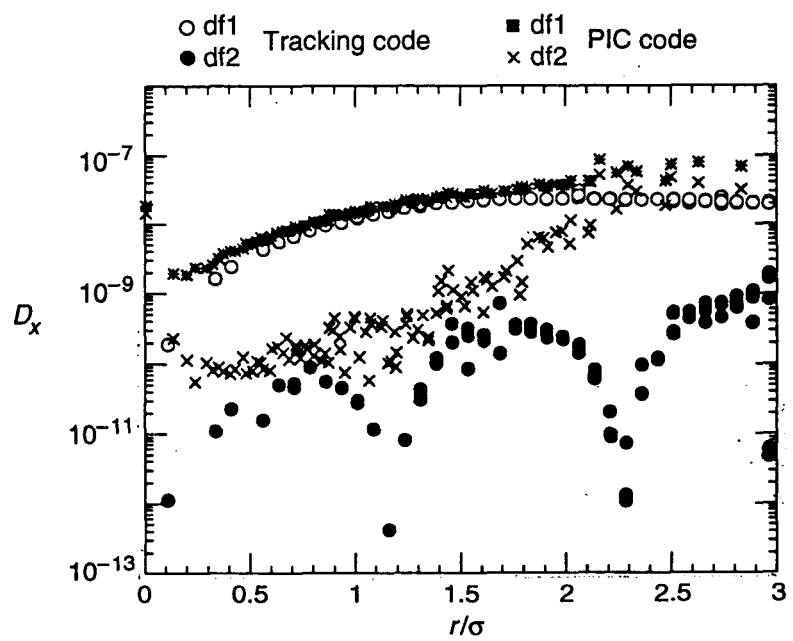

Figure 7.54. D_x from Tracking Code and the Strong-Strong Code with Uniform Charge Particle Initialization for $M = 10,240$ Rotations. df1 and df2 have time scales of $\Delta N_1 = 102$ and $\Delta N_2 = 1024$ rotations, respectively.

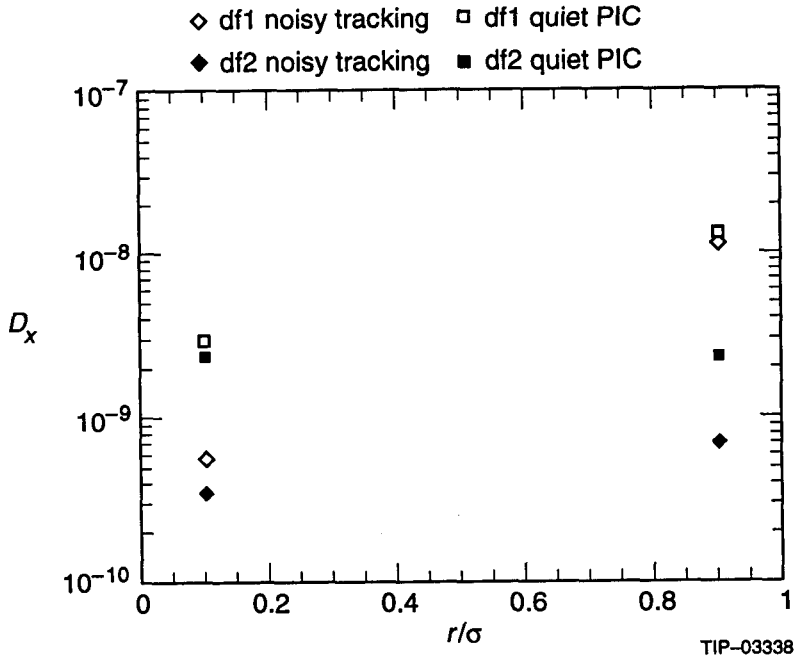

Figure 7.55. D_x from Noisy Tracking Code and PIC Code for $M = 10,240$ Rotations at $r/\sigma = 0.1$ and 0.9. df1 and df2 have time scales of $\Delta N_1 = 102$ and $\Delta N_2 = 1024$ rotations, respectively.

7.3.3 δf Simulation Results

In this section we describe particle diffusion results obtained from the δf simulation code described in Section 6.4. SSC reference parameters from Section 7.2.1 are used, with $\nu_0 = 0.285$ and $\Delta\nu_0 = 2.1\times10^{-3}$. Each beam in the simulation has 10^3 simulation particles, with the initial distribution in (x, p_x) phase space shown in Figure 6.9. The Poincare map of two sample particles after 10^5 rotations is shown in Figure 7.56. The particles are sampled once every complete rotation. Little diffusion is apparent for both sample particles. The smearing seen for the small amplitude is much less than that observed with either strong-strong code.

The diffusion coefficients are calculated for 100 sample particles after 10,240 rotations. The initial particle positions are shown in Figure 7.57. As in previous sections the diffusion coefficients, df1 and df2, are calculated using $|x|$ in Eq. (6.161). The diffusion D_x is normalized to σ_x^2/N_r, where N_r is the number of rotations. Results from the δf code and tracking code after 10,240 rotations are shown in Figure 7.58. The diffusion coefficients for the δf and tracking code nearly overlay each other. Both codes show oscillatory motion for 10,240 rotations. Thus, the noise level of the δf code is less than the strong-strong code with either the variable or uniform charge distribution.

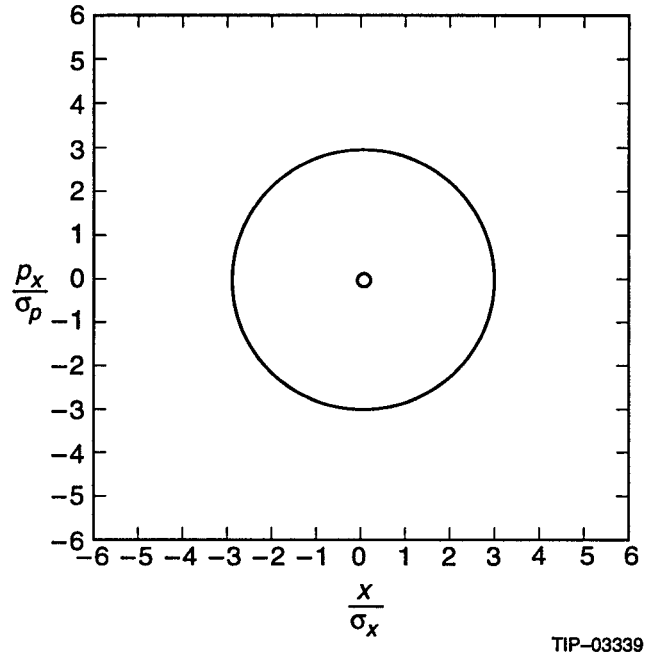

Figure 7.56. Poincare Section in $(x/\sigma_x, p_x/\sigma_p)$ Space of Small- and Large-Amplitude δf Code Particles After $M = 10,240$ Rotations.

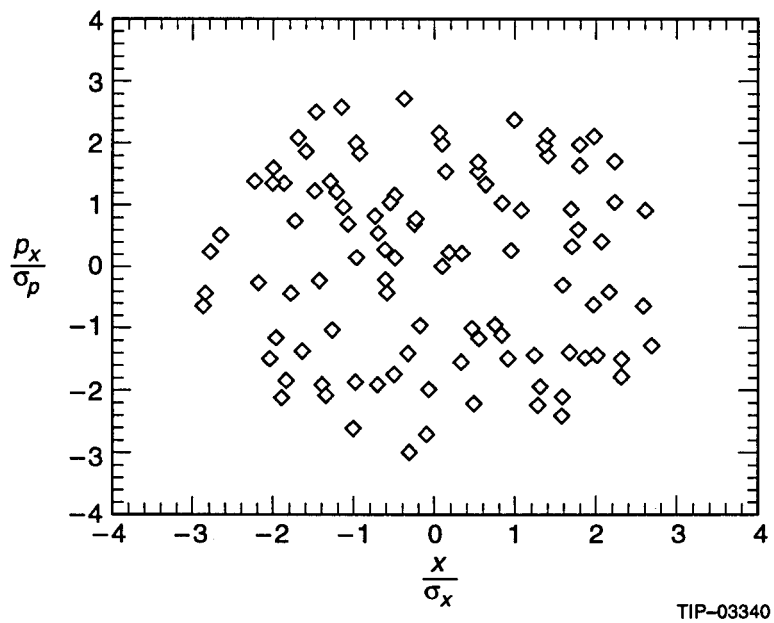

Figure 7.57. Initial Distribution in (x, p_x) Phase Space of 100 Sample Particles.

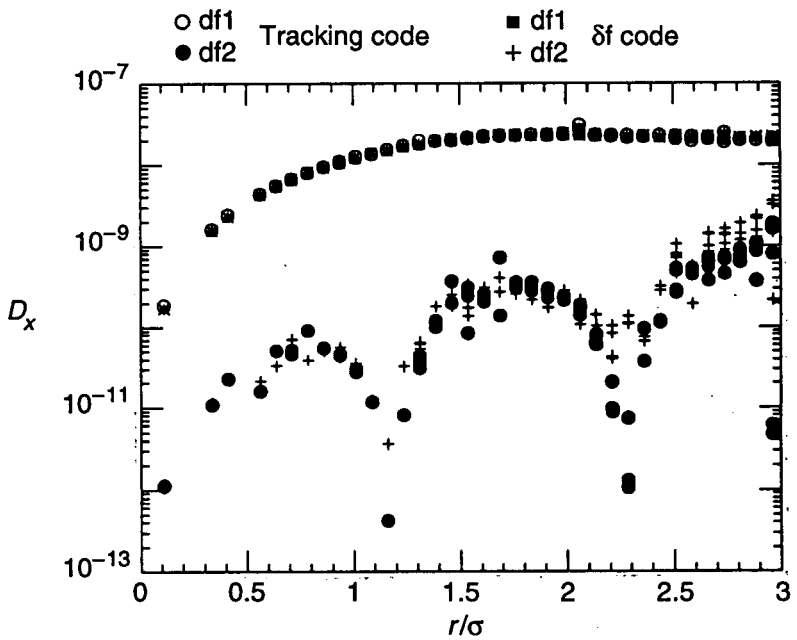

Figure 7.58. D_x from the δf Code with 1000 Simulation Particles and the Tracking Code for $M = 10,240$ Rotations. df1 and df2 have time scales of $\Delta N_1 = 102$ and $\Delta N_2 = 1024$ rotations, respectively.

Simulations with 100, 1000, and 10,000 particles show little effect on the diffusion of the particles from particle number for $M = 10,240$ rotations (Figure 7.59). For 100 simulation particles, there is some deviation for sample particles with $r/\sigma < 1$. The noise level is not as strong a function of particle number as the strong-strong code.

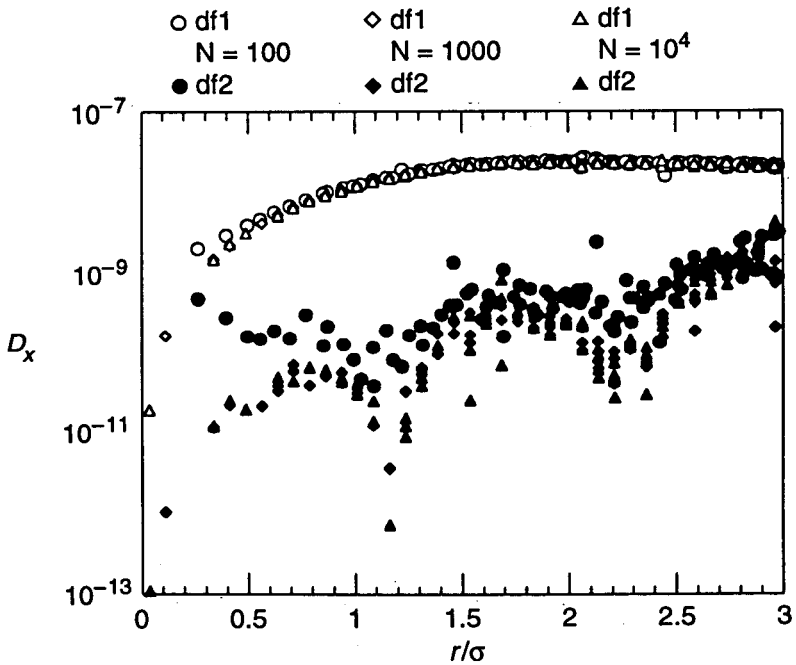

Figure 7.59. Variation of the Diffusion Coefficients with Particle Number N for $M = 10,240$ Rotations.

The sample particles begin to show diffusive behavior when the number of rotations is increased. Figure 7.60 shows the diffusion coefficients, df1 and df2, calculated for 40,960 rotations. Particles with $r/\sigma > 2$ are diffusive (df1 $\approx$ df2). This same behavior is observed for 10,240 rotations in the strong-strong code with the uniform charge distribution (Figure 7.54). The particles with $r/\sigma < 2$ are still somewhat oscillatory in nature. It appears that the particles in the tail of the distribution are most sensitive to either noise or collective motion in the beams. This diffusion in the tails is not due to finite particle noise, as is evident in Figure 7.61. The figure shows the diffusion coefficients calculated for $N = 1000$ and $N = 10^4$ simulation particles for 40,960 rotations. The results are nearly identical.

A comparison of the δf and tracking code at 40,960 rotations is shown in Figure 7.62. The tracking and δf code diffusion coefficients are nearly equal to the short time scale coefficient df1, with values of $r/\sigma < 1.5$. For the long time scale coefficient, df2, and $r/\sigma > 1.5$, the δf code shows more diffusive behavior. This indicates that the phenomenon that causes the diffusive motions for large r/σ is most evident on time scales of 409 rotations. Diffusive motion is not evident for particles with $r/\sigma < 1.5$. This indicates that the diffusion occurs on longer time scales there. This is shown in longer runs. It appears that the diffusion is largest for large r/σ and smallest for small r/σ.

In order to determine the source of the diffusion observed in the δf code, noise of the form described in Section 6.3.4 is added to the tracking code. Figure 7.63 shows the results for 40,960 rotations, where the noise level δ is determined by

$$\delta = \frac{1}{\sqrt{N(x)}}, \tag{7.13}$$

where $N(x) = N\mathrm{erf}(x/\sqrt{2}\sigma_x)$ and N is the particle number. Notice that the long time scale coefficient df2 increases for small r/σ and, therefore, df2 is more uniform in r/σ. The form of D_x as a function of r/σ is different from D_x calculated from the δf code. It is apparent that the enhanced diffusion observed in the tails of the distribution for the δf code is due to the self-consistent treatment of the beams. This enhanced diffusion in the tails was also observed in the strong-strong code with the uniform charge initialization and fewer rotations.

When the δf code is run for 10^5 rotations, all the sample particles show diffusive behavior (Figure 7.64). The diffusion D_x is an approximately exponential function of r/σ. The coefficients take nearly the same value as the long time scale diffusion coefficient, df2, calculated for 40,960 rotations (Figure 7.60). The diffusive time scale appears to be in the range of 400 to 4000 rotations.

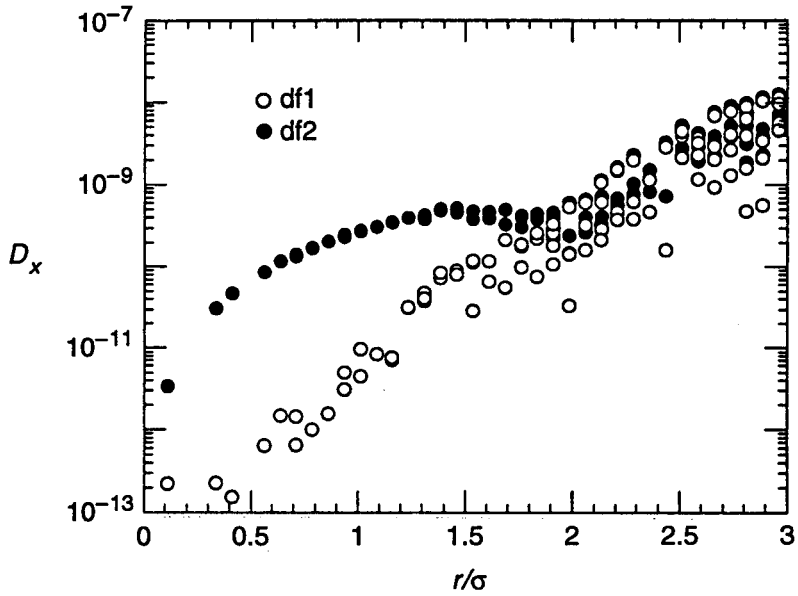

Figure 7.60. D_x from the δf Code with 1000 Simulation Particles for $M = 40,960$ Rotations. df1 and df2 have time scales of $\Delta N_1 = 409$ and $\Delta N_2 = 4096$ rotations, respectively.

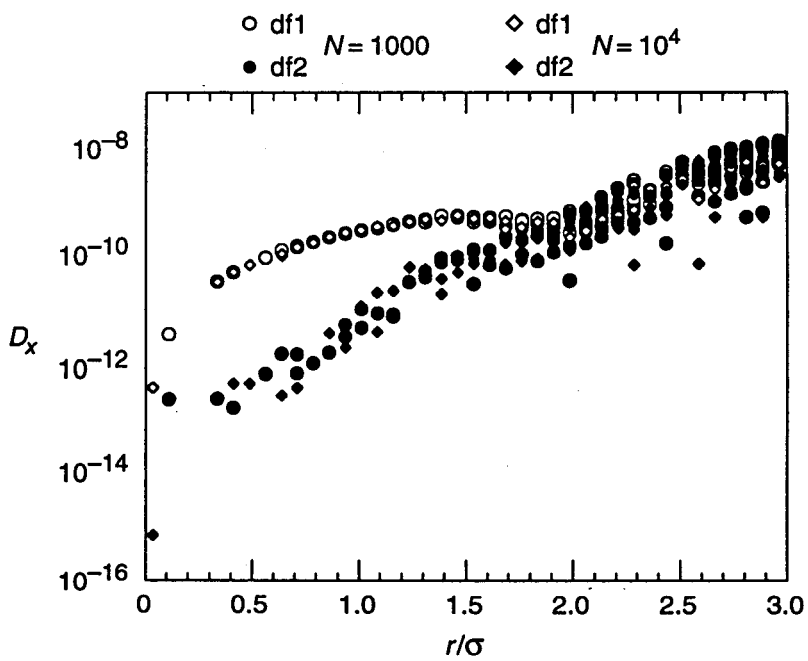

Figure 7.61. Variation of the Diffusion Coefficients with Particle Number N for $M = 40,960$ Rotations.

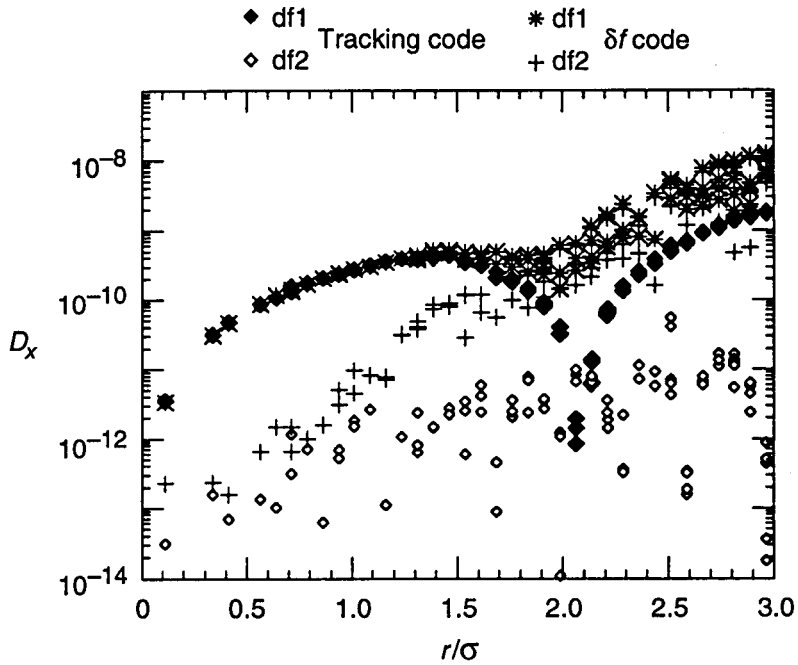

Figure 7.62. D_x from Tracking Code and the δf Code for $M = 40,960$ Rotations. df1 and df2 have time scales of $\Delta N_1 = 409$ and $\Delta N_2 = 4096$ rotations, respectively.

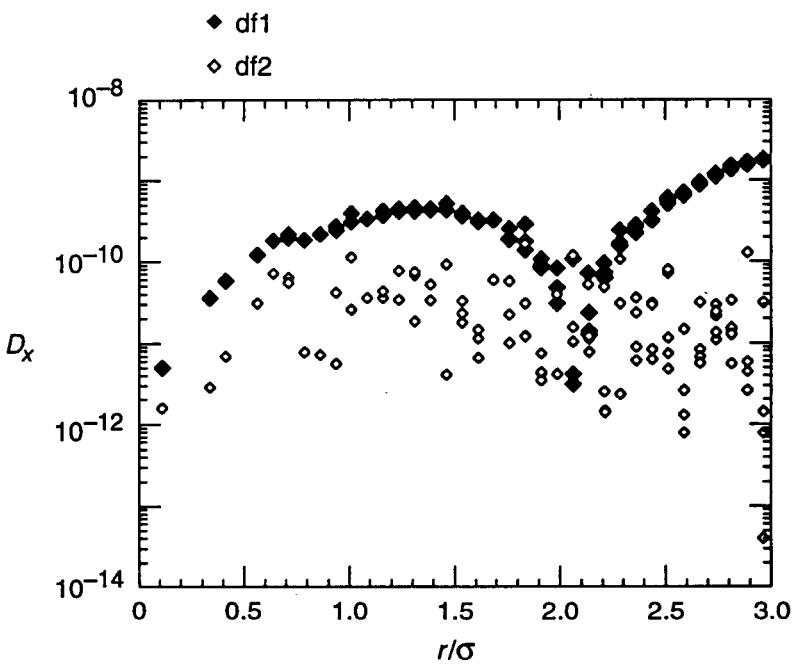

Figure 7.63. D_x from Noisy Tracking Code for $M = 40,960$ Rotations. df1 and df2 have time scales of $\Delta N_1 = 409$ and $\Delta N_2 = 4096$ rotations, respectively.

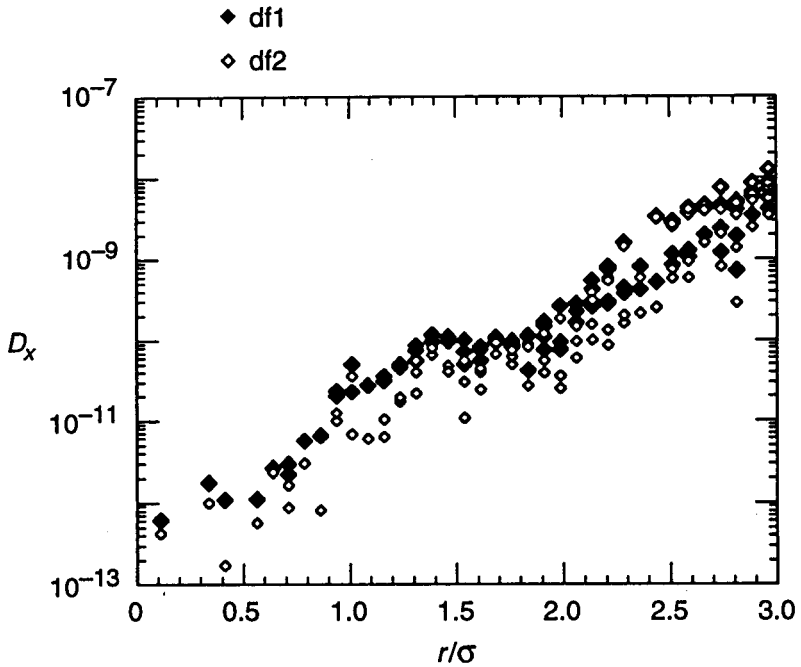

Figure 7.64. D_x from the δf Code for $M = 10^5$ Rotations. df1 and df2 have time scales of $\Delta N_1 = 1000$ and $\Delta N_2 = 10,000$ rotations, respectively.

A comparison of the δf and tracking code results at 10^5 rotations is shown in Figure 7.65. As in the run with 40,960 rotations, the diffusion coefficients obtained from the tracking and δf runs are nearly equal for the short time scale coefficient, df1, with values of $r/\sigma < 1.5$. For the long time scale coefficient, df2, and $r/\sigma > 1.5$, the δf code shows diffusive behavior and is higher in value than the coefficients from the tracking code.

Figure 7.66 shows the diffusion coefficients calculated for $N = 1000$ and $N = 10^4$ simulation particles for 10^5 rotations. The coefficients for both particle numbers overlap, indicating that the diffusion observed is not strongly dependent on the simulation particle number.

In order to get an idea of where the stochastic regions are in phase space, the simulation code is run forward and backward in time. In chaotic regions the particle motion is very sensitive to initial conditions, and the orbits bifurcate exponentially. Since the numerical integration of the code has finite accuracy, the particles that have passed through chaotic regions most likely would not return to their initial conditions when the code is run forward and then backward. Figure 7.67 shows results from running the δf code forward and backward 10^5 rotations with 1000 particles. In the figure contour, surface, and grey-scale plots of the particle, weights δf_i of one of the beams are shown. The reference parameters $\nu_0 = 0.285$ and $\Delta\nu_0 = 2.1 \times 10^{-3}$ are used. It is found that the particle positions return to their original positions within 8 decimal places. The deviation from the initial conditions

is found in the weights δf_i for each particle i. Figure 7.67 is the result of a dump of 200 consecutive rotations of particle weights. The weights from the forward time-stepping are subtracted from the corresponding weights from the backward time-stepping. The figure shows positive deviations for small-amplitude particles and negative deviations for large-amplitude particles. It may be interpreted that these particles are in stochastic regions. The positive and negative deviation regions are separated by a thin ring where there is no deviation. The lack of deviation does not automatically determine a region of non-stochasticity. However, we may imagine there lie regions of non-stochasticity in this ring area. Due to the limited resolution the ring may consist of islands separated by stochastic regions.

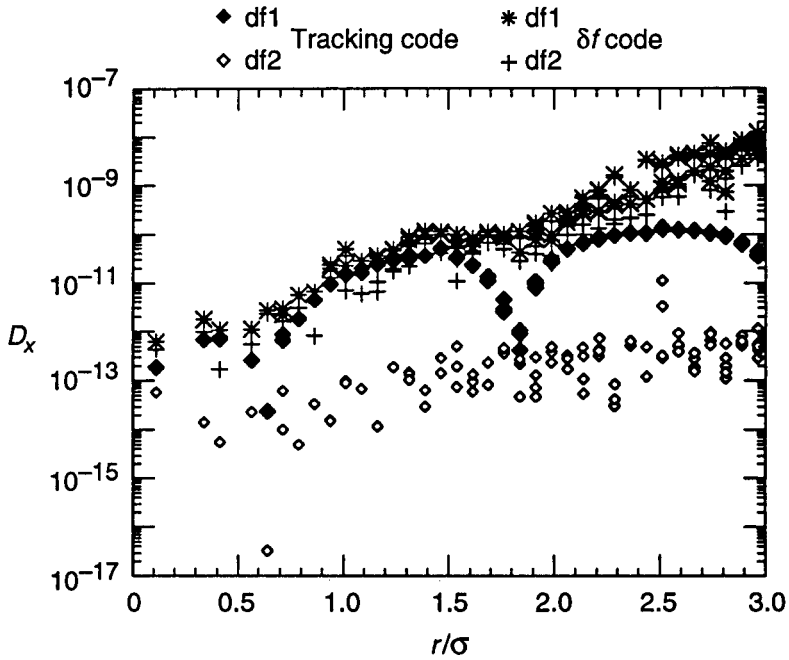

Figure 7.65. D_x from Tracking Code and the δf Code for $M = 10^5$ Rotations. df1 and df2 have time scales of $\Delta N_1 = 1000$ and $\Delta N_2 = 10,000$ rotations, respectively.

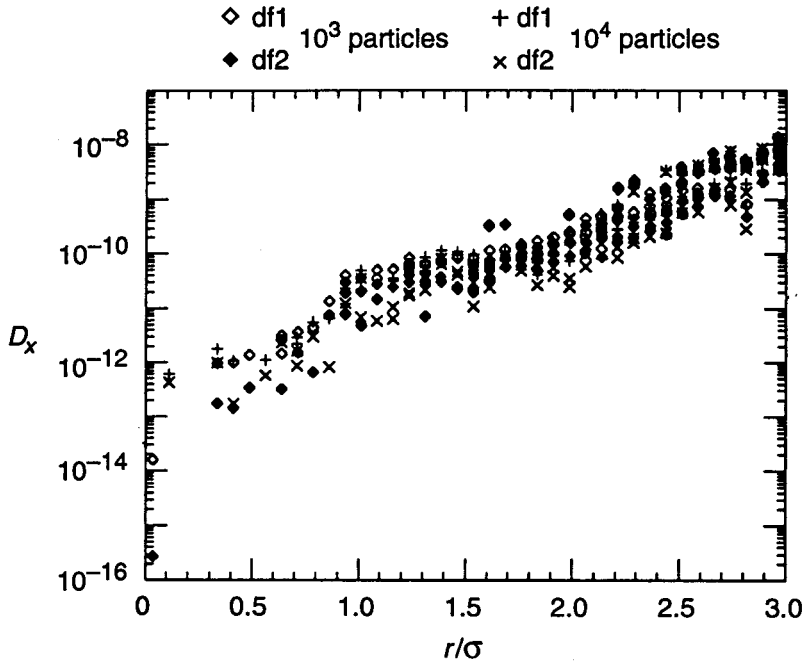

Figure 7.66. Variation of the Diffusion Coefficients with Particle Number N for $M = 10^5$ Rotations.

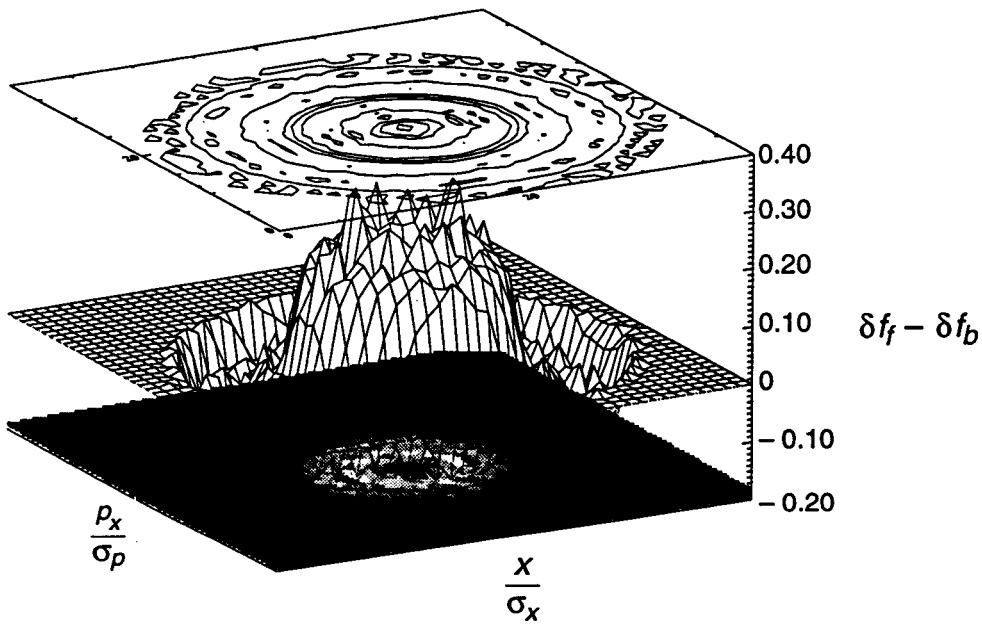

Figure 7.67. A $(x/\sigma_x, p_x/\sigma_p)$ Space Plot with Contour, Surface, and Grey-Scale Plots from the Top to the Bottom of the Figure.

7.3.4 Beam Offset Effects

In this section we examine the effects of beam offset on particle diffusion. Simulation results are compared with the theoretical predictions of Stupakov.[22] A tracking code and a δf code are used to compare with Eq. (3.76) described in the previous section. Parameters from the SSC are used to compare the analytic results with the simulation results. In this case $\nu = 0.285$ and $\Delta\nu = \xi = 2.1 \times 10^{-3}$. These numbers can be used to get an approximate number for the diffusion from Eq. (3.79). An estimate of δx can be obtained from plots of the average x position of the beam versus the number of rotations M (Figure 7.68). The estimate of $\delta x = \frac{\Delta x}{\sigma_x}$ is 0.0005. From this an approximate value of the diffusion D is

$$D \approx 10^{-13}\sigma_x^2/\text{turn}. \tag{7.14}$$

Figure 7.69 shows the total change in the action $< (\Delta J_M)^2 >$ versus the action J for various values of the beam offset ζ calculated from Eq. (3.74). The action J is normalized to $p\sigma_x^2/\beta^*$ and the beam offset is normalized to σ_x. The plot is obtained with the assumption that the beam offsets are uncorrelated, so that the $k = 0$ term in Eq. (3.76) is the only nonzero one. The offsets plotted are for $\zeta = 0.0001$, 0.001, and 0.01. Note that $< (\Delta J_M)^2 >$ increases with ζ as ζ^2, which is expected from Eq. (3.76).

Figure 7.70 shows tracking code and analytic results. The tracking code is run for $M = 10^5$ turns, with $\nu_0 = 0.285$ and $\Delta\nu_0 = 2.1 \times 10^{-3}$. The total change in the action $< (\Delta J_M)^2 > /2$ is divided by M, the number of turns, to get the change per turn. The data points represent 100 uniformly distributed tracking particles that are run for each value of the beam offset ζ (Figure 7.71). As is evident in Figure 7.68, the diffusion coefficients (df1, df2) calculated on different time scales for each particle are close to one another, indicating that all the particles show diffusive behavior. There is good agreement between the tracking code results and the analytic predictions based on the random offset model of Stupakov.[22] Both show leveling off in the diffusion with increasing values of the action J.

The δf code results over 10^5 turns are shown in Figure 7.72. The δf code is started with zero offset and is allowed to evolve self-consistently for $M = 10^5$ turns. Analytic results for 3 values of the beam offset, $\zeta = 0.01$ to $0.0001\sigma_x$, are shown in the background, while the simulation value of ζ is in the range of 0.0005 to $0.001\sigma_x$. As is evident in the figure, the values of the diffusion in the action variable J cross the range of the analytic prediction. However, the functional dependence on the action J is very different. The δf results show an exponential dependence on the action J for large values of J, whereas the Stupakov theory shows the diffusion leveling off. The approximate value for the diffusion calculated from the change in the luminosity (Eq. (7.14)) produces a value that is lower than most of the δf simulation values.

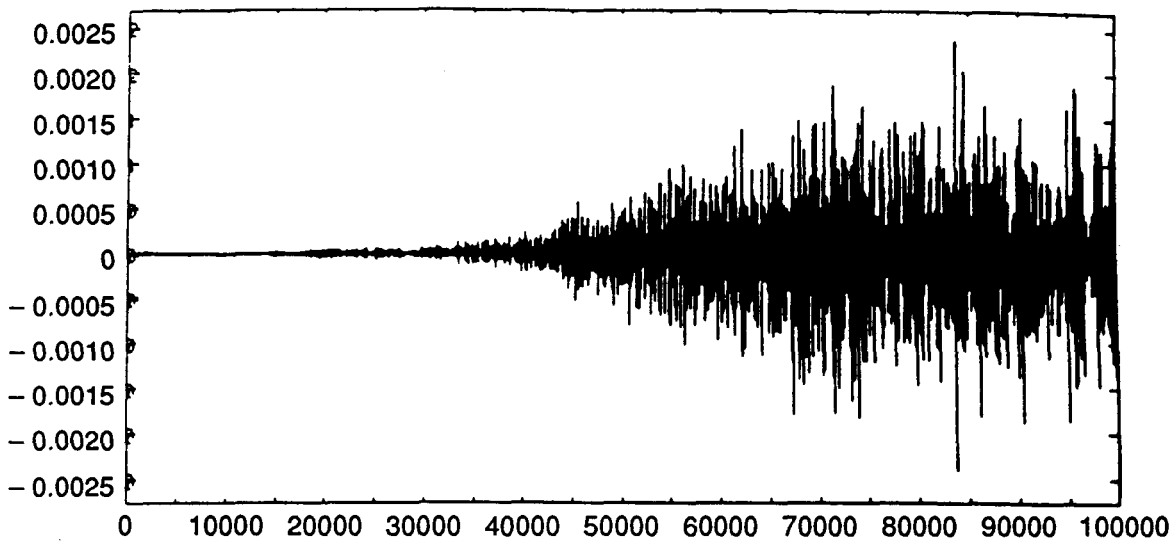

Figure 7.68. $< x > /\sigma_x$ Versus M from δf Simulation, with $\nu_0 = 0.285$ and $\Delta\nu_0 = 0.0021$.

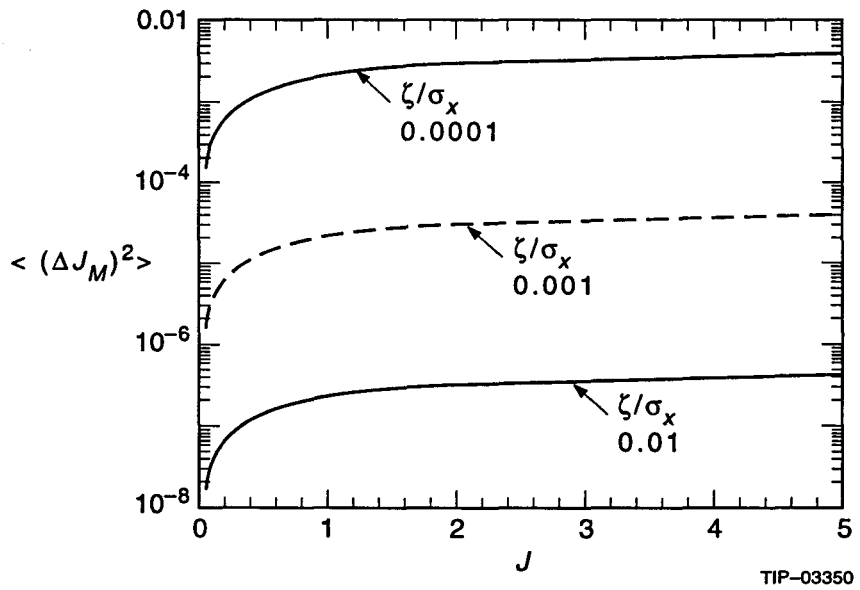

Figure 7.69. Total Change in the Action ΔJ_M Versus the Action J for Three Values of the Beam Offset ζ.

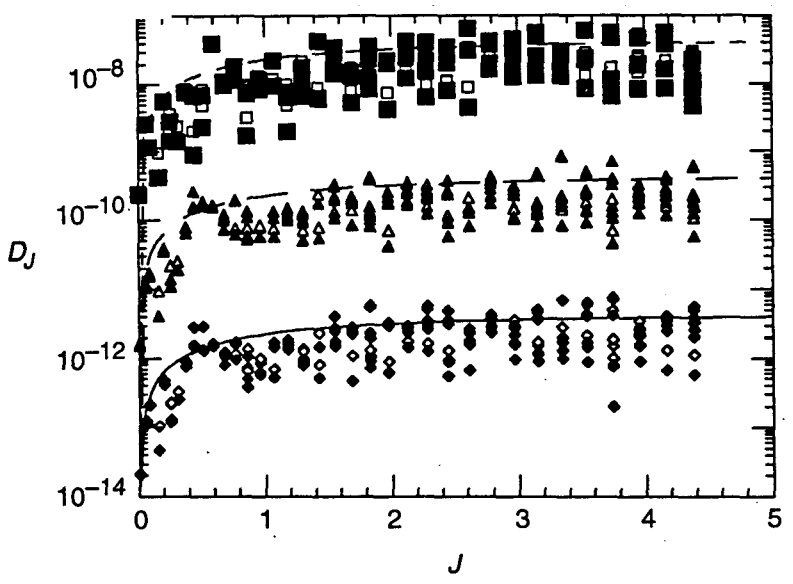

Figure 7.70. Tracking Code Results Showing the Change in $< (\Delta J_M)^2 > /2$ Per Turn Versus the Action J for Three Values of the Beam Offset ζ. The time scales over which df1 and df2 are calculated are 10^3 and 10^4 rotations, respectively.

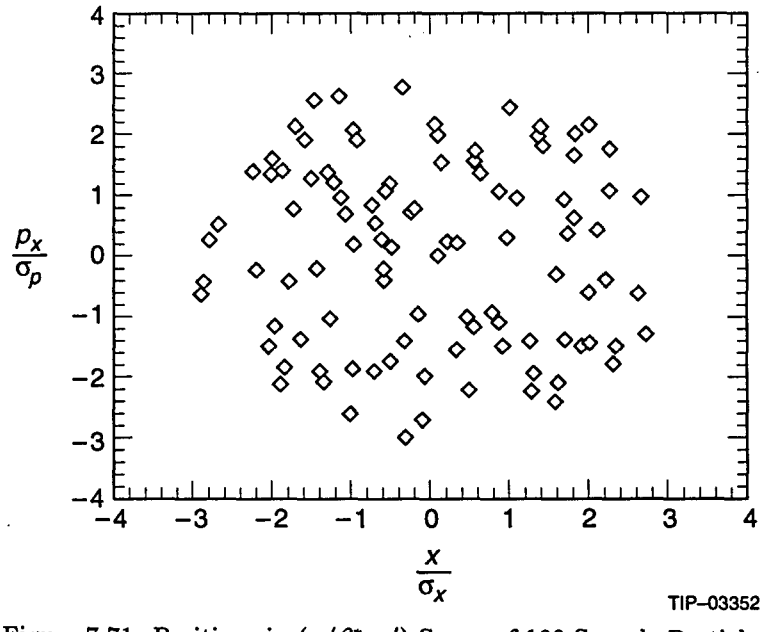

Figure 7.71. Positions in $(x/\beta^*, x')$ Space of 100 Sample Particles.

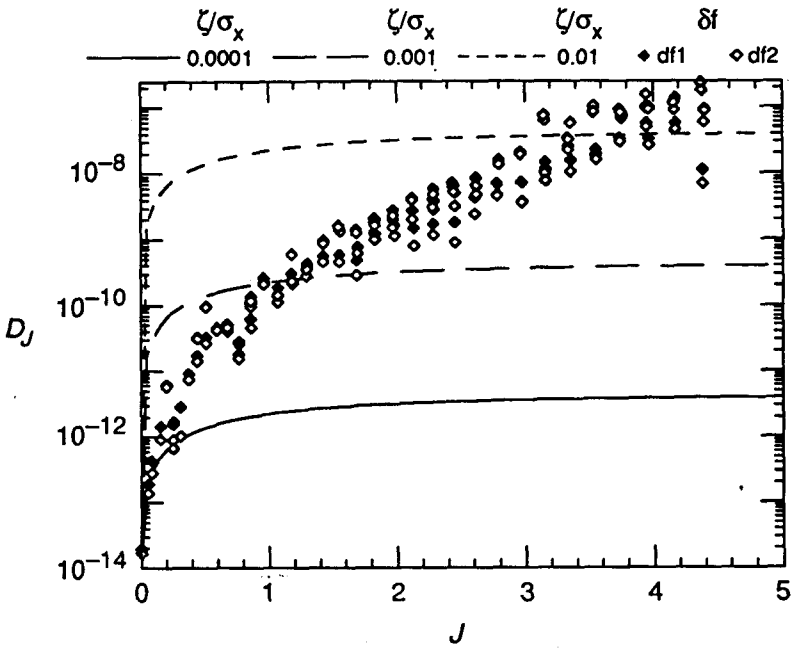

Figure 7.72. δf Code Results Showing the Change in the Action ΔJ_M Per Turn Versus the Action J for Zero Initial Beam Offset. The time scales over which df1 and df2 are calculated are 10^3 and 10^4 rotations, respectively.

Several avenues are examined in order to get an idea of the cause of the exponential dependence in the diffusion. Figure 7.73 shows the effects of adding terms of $k = 1$ and $k = 2$ to Eq. (3.76). The coefficients are chosen from peaks at the appropriate frequency in the power spectra of $< x >$ from Figure 7.68. The effect of adding the $k = 1$ and $k = 2$ terms to Eq. (3.76) is negligible. The change in the action still levels off for large J. Figure 7.74 shows the results of using the output $< x >$ from the δf code shown in Figure 7.68 in the tracking code. Analytical results are also plotted for various values of the beam offset ζ. The tracking code and analytic results show the same functional behavior with respect to J. The corresponding beam offset is in the range $\zeta = 0.001$ to 0.01. Although the diffusion from the tracking code is in the same range as the δf code results, the exponential behavior for large J is not seen (Figure 7.75). The exponential dependence can be reproduced from Eq. (3.76) when the arguments to the modified Bessel functions I_0 and I_1 are replaced with J rather than $J/2$. The reason for this agreement is still under investigation (Figure 7.76). The diffusion from Stupakov's theory[22] is dependent on the $< x >$ offset of the beam. Figure 7.77 shows the dependence of $< x >$ offset on r/σ, where r/σ is from Eq. (7.10). $\frac{<x>_1}{\Delta}$ refers to particles in the range $0 < r/\sigma < 1$. $\frac{<x>_2}{\Delta}$ refers to particles in the range $1 < r/\sigma < 2$. $\frac{<x>_3}{\Delta}$ refers to particles in the range $2 < r/\sigma < 3$. The fluctuation levels increase in magnitude with r/σ. So large amplitude particles have $< x >$ motions that are about an order of magnitude higher than those at small amplitudes.

This difference in $< x >$ with r/σ would explain the higher diffusion coefficients in the tails of the distribution. The reason for this larger beam offset is still under investigation.

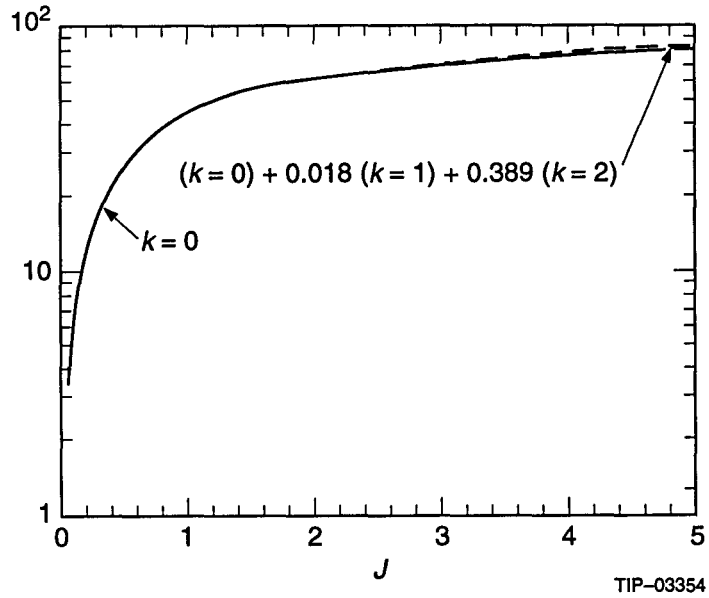

Figure 7.73. A Comparison of $k = 0$ with Terms $k = 1$ and $k = 2$.

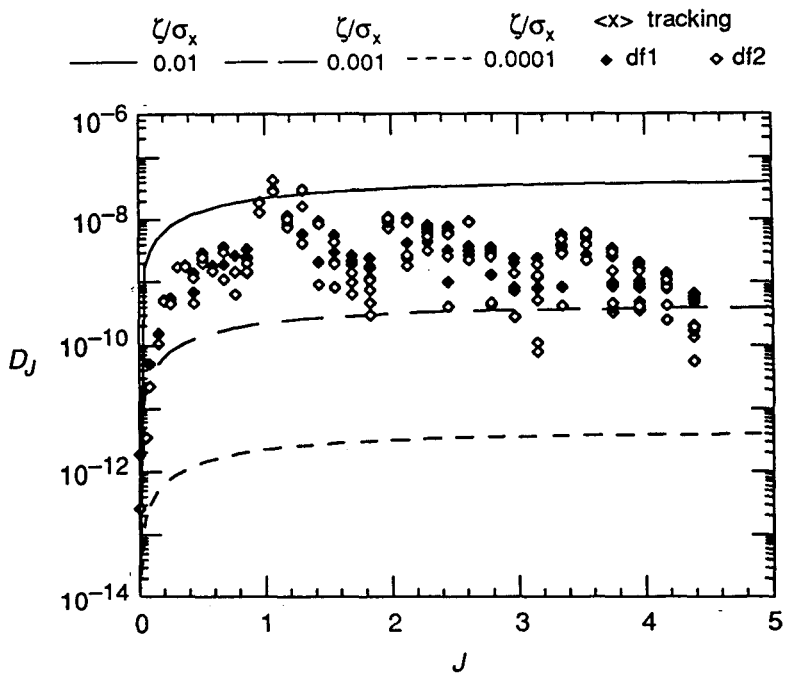

Figure 7.74. A Comparison of Tracking Code with Input $< x >$ and Theory.

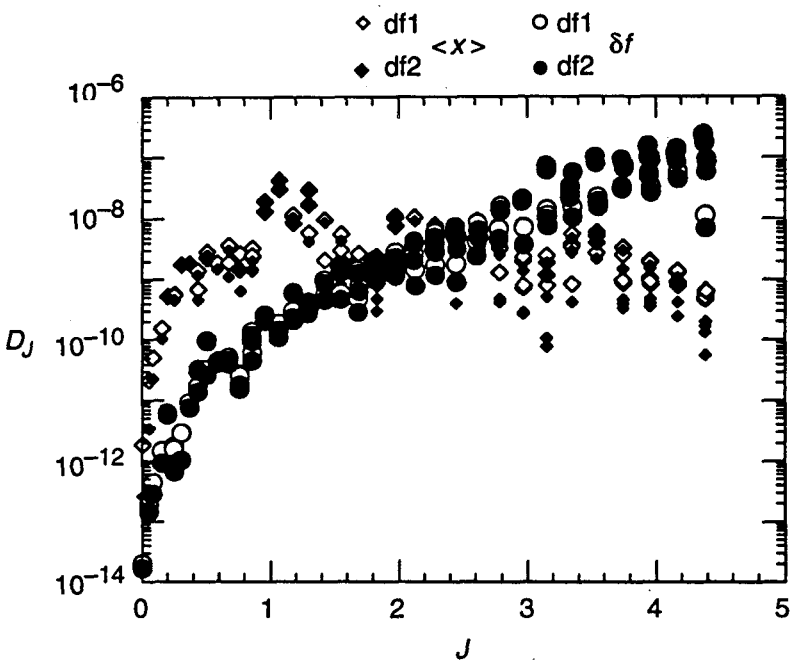

Figure 7.75. A Comparison of Tracking Code with Input $< x >$ and δf Results.

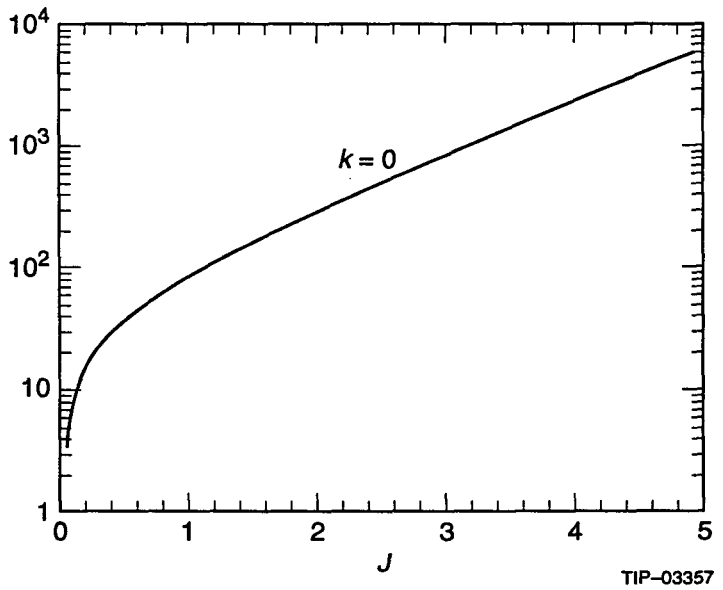

Figure 7.76. The Function Dependence of the Change in the Action with Argument J Rather Than $J/2$.

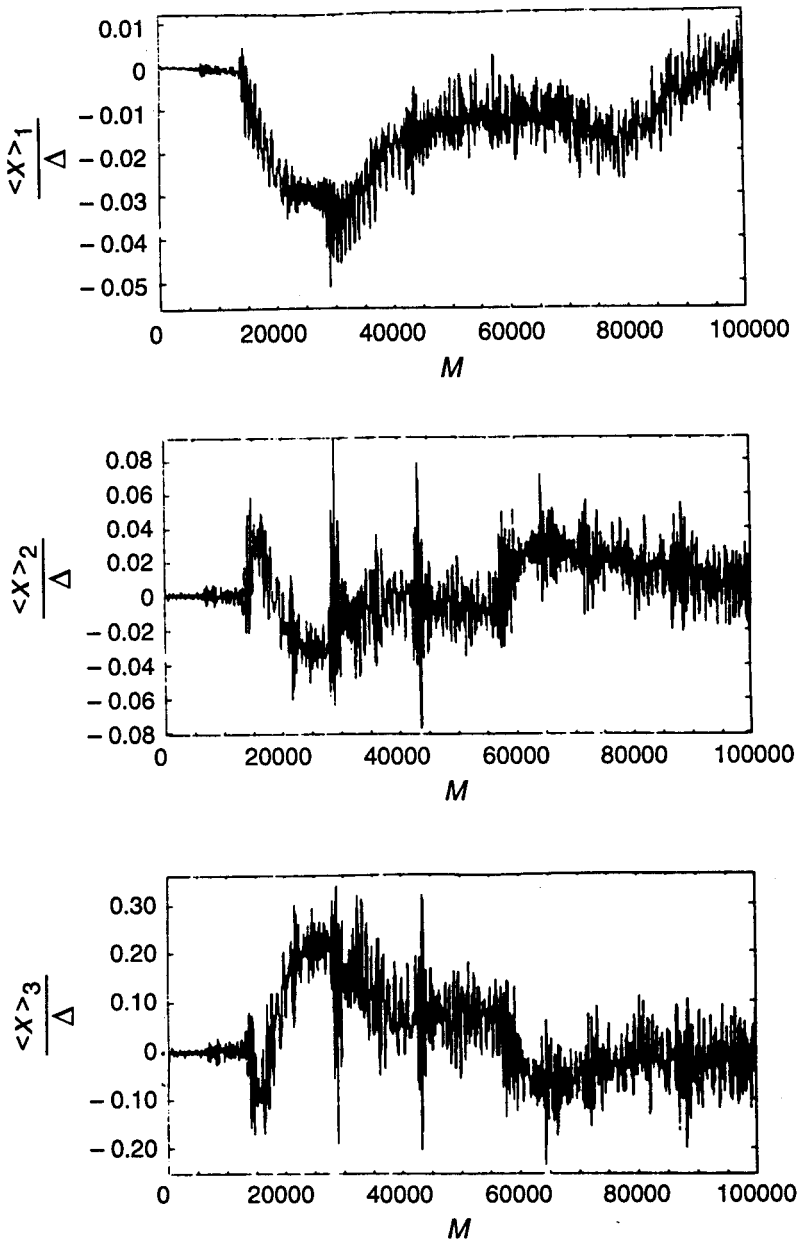

Figure 7.77. The Average Beam Offset $< x > /\Delta$ for Small, Medium, and Large r/σ Particles Down the Figure.

The leveling off in the diffusion is produced in the δf code when the beam strength is increased. When the tune shift is increased from $\Delta\nu_0 = 2.1 \times 10^{-3}$ to $\Delta\nu_0 = 8.4 \times 10^{-3}$, the resulting motion of the beam about the original beam center increases by approximately an order of magnitude (Figure 7.78). The diffusion coefficients D_x calculated for $\Delta\nu_0 = 2.1 \times 10^{-3}$ and $\Delta\nu_0 = 8.4 \times 10^{-3}$ are shown in Figure 7.79. It is evident from the figure that the diffusion increases for the small-amplitude particles ($r/\sigma < 2$) when $\Delta\nu_0$ is increased to 8.4×10^{-3}. The net effect is uniform diffusion across the beam in this case. The resulting diffusion is similar to that of beam offset diffusion.[22]

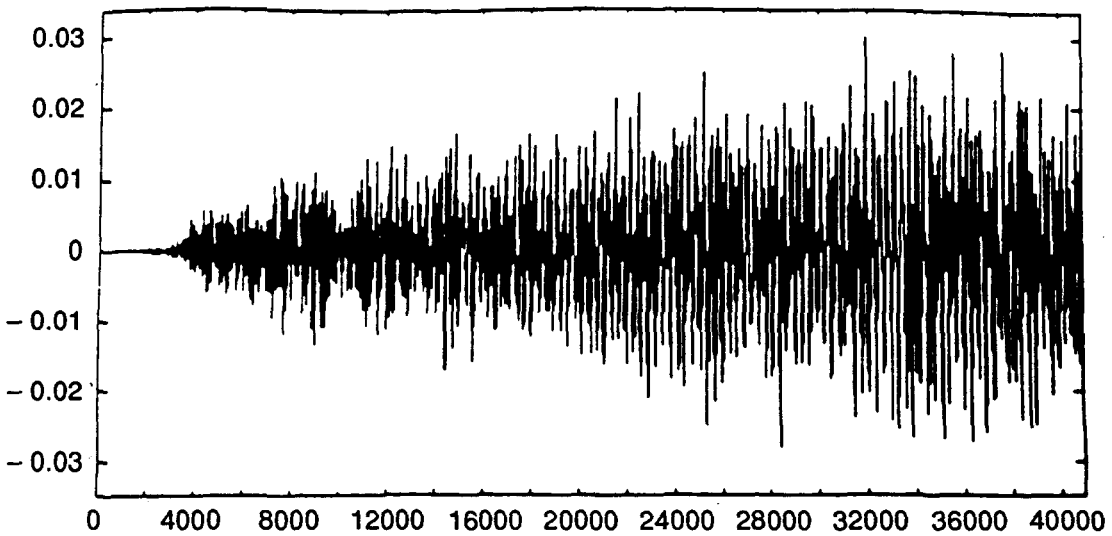

Figure 7.78. $< x >$ of the Beam with $\Delta\nu_0 = 8.4 \times 10^{-3}$.

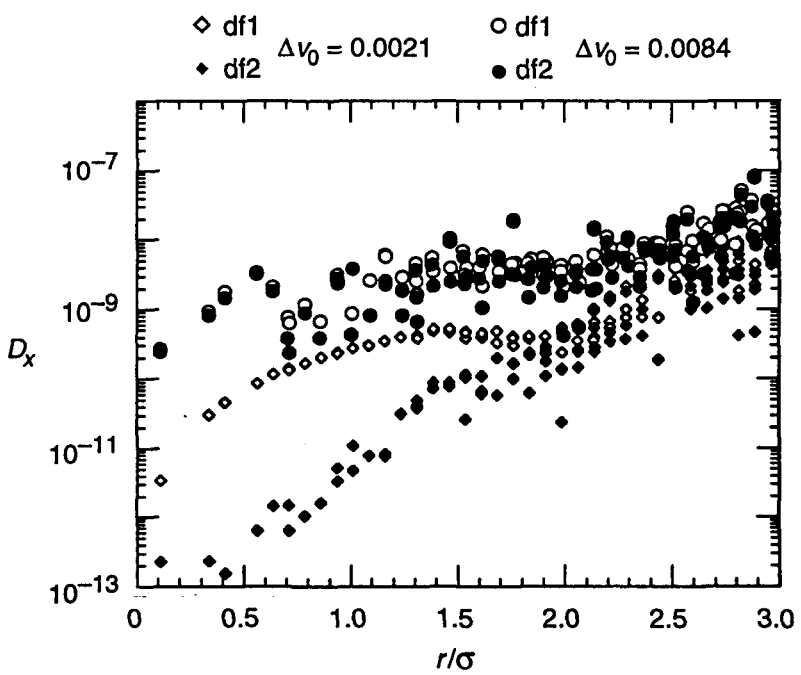

Figure 7.79. D_x of the Beam with $\Delta\nu_0 = 2.1 \times 10^{-3}$ and $\Delta\nu_0 = 8.4 \times 10^{-3}$ for $M = 40,960$ Rotations. The time scales of df1 and df2 are 409 and 4096 rotations, respectively.

This same behavior is seen in the strong-strong simulations. Figure 7.80 shows the diffusion coefficients calculated for the PIC and the δf codes. The leveling off in the diffusion is seen for the PIC code and not for the δf code. The δf code for $M = 10,240$ rotations still shows oscillatory behavior for all values of r/σ.

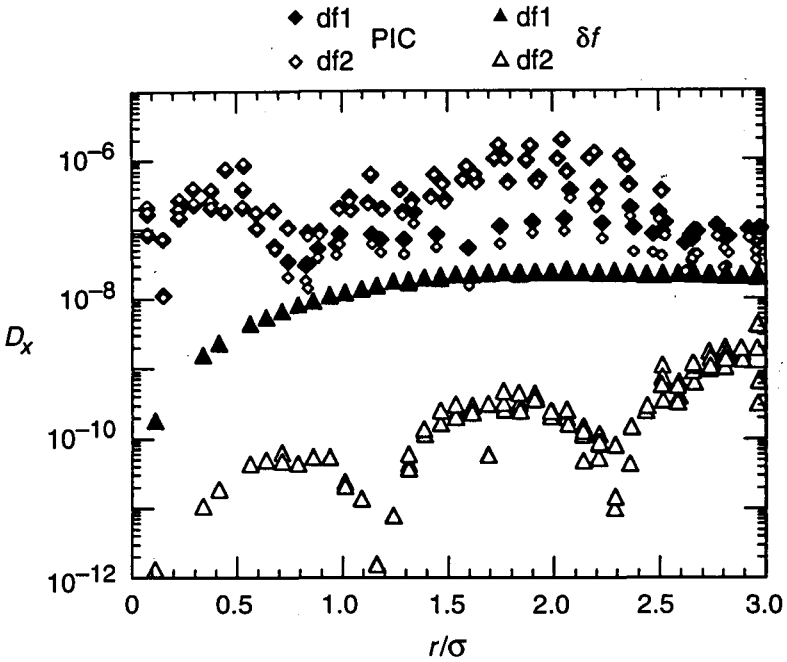

Figure 7.80. D_x from PIC and δf Codes of the Beam with $\Delta\nu_0 = 2.1 \times 10^{-3}$ for $M = 10,240$ Rotations. The time scales of df1 and df2 are 102 and 1024 rotations, respectively.

It appears as if the fluctuation level of the simulation determines whether the diffusion due to the presence of nonvanishing $< x >$ suggested by Stupakov[22] dominates the particle diffusion. In the cases where the fluctuation level is high—either from the strength of the kick $\Delta\nu_0$ or from simulation noise—the $< x >$ type of diffusion dominates. This behavior in the diffusion may be viewed as a process similar to the breakup of KAM tori.[57] For low fluctuation levels where the tune shift is small and the noise level is low, the phase space may contain many stable regions surrounded by regions of stochasticity. As the fluctuation level is increased, the stable regions disappear and the whole phase space becomes stochastic. When this occurs, the diffusion of the particles becomes nearly uniform across the phase space, as observed in the simulations with high $\Delta\nu_0$ and high noise levels.

8.0 CONCLUSIONS

In this section we discuss the results of our investigations of the beam-beam interaction and their relevance to modern circular accelerators. We also suggest future improvements that can be made to the currently developed numerical tools.

8.1 Summary of Results

We have examined the effects of collective interactions between counterstreaming proton beams via various simulation techniques. Two types of code have been developed to study the effects of the filamentation instability: an electromagnetic PIC code and a Vlasov code. Three types of code have been developed in increasing sophistication to study the beam-beam interaction : (1) a tracking code, (2) a strong-strong code, and (3) a δf code.

8.1.1 Filamentation Instability

Fair agreement is found between linear theory of the filamentation instability[23] and the electromagnetic PIC code for beams with width w_b greater than λ_c the collisionless skin depth. The filament sizes correspond approximately to a collisionless skin depth λ_c, and the measured growth rate is close the maximum growth rate. It is found that the filamentation instability is not suppressed by having the counterstreaming beams small in width in comparison with the collisionless skin depth of the beam λ_c.

In the Vlasov code two counterstreaming electron beams are also found unstable to the filamentation instability. The maximum growth rate $\Gamma_{max}/\omega_b \approx 0.4$ is close to the theoretical maximum filamentation growth rate. As the beam evolves, it begins to spread in x. The filament sizes are between approximately $0.5\lambda_c$ and λ_c. The code is timed for various problem sizes, and performance is about 2.3 times faster than the Cray YMP. However, the distribution function becomes negative from truncation error. This an inherent drawback with the Vlasov simulation technique.

From these results it is apparent that the filamentation instability will have much more of an effect on electron-electron or electron-positron synchrotrons. The fraction of the growth time is higher on such machines than it is on hadron machines such as the SSC.

8.1.2 Collective Beam-Beam Effects

Among the codes developed, the strong-strong and δf codes are best suited for studying beam-beam collective effects. The electromagnetic PIC code requires too many time steps to cover one interaction time, and the tracking code does not show beam collective motions. The strong-strong code's main drawback is the amount of fluctuation noise produced by the finite number of particles used. This noise may be reduced by initializing the particles using the quiet start.[36] Also, although the δf code is much quieter than the strong-strong code, it is better suited for studying the beam-beam interaction away from resonances.

Using the reference parameters of the SSC, oscillations in $\Delta\nu$ are observed in the strong-strong simulations. The oscillations indicate expansion and contraction of the beams. The beam expansion and contraction varies with different particle positions. The small-amplitude portion of the beam is increasing in oscillation amplitude while the entire

beam is decreasing in oscillation amplitude. The odd moments of the beam, $< x >$ and $< (x- < x >)^3 >$, are increasing in oscillation amplitude with rotation number. The amplitudes of the even moments, $< (x- < x >)^2 >$ and $< (x- < x >)^4 >$, both decrease with the number of rotations. The phenomena of the "flip-flop" effect,[7] where one beam is decreasing in phase space area and the other beam is increasing, is observed in our simulations. It is found to be sensitive to the initial conditions.

Differences between the nonuniform charge and uniform charge initializations are found. The beam distribution from the uniform charge initialization is smoother than the distribution from the nonuniform charge distribution at the beginning and end of the simulation. The oscillations in $\Delta\nu$ indicate that the expansion and contraction of the beam with uniform charge initialization is smaller than the nonuniform charge initialization. Overall the fluctuation levels in the uniform charge initialization are smaller than in the nonuniform charge initialization.

The simulations based on the δf algorithm show the lowest fluctuation levels of all the codes except the tracking code. However, the tracking code does not include internal dynamics of the beam. After 10^5 rotations the two main approximations of the δf code are still valid. The deviation from the initial Gaussian distribution is still small. The maximum perturbations to the Gaussian background are only 0.1% of the background distribution. Also, the constant phase space density assumption remains a good approximation. After 10^5 rotations in the δf code the simulation particles are no longer uniformly distributed in $(x/\sigma_x, p_x/\sigma_p)$ space. However, clumping of particles is not significant. In the simulations using the reference SSC parameters, the amplitude of the variation in $\Delta\nu$ for small-amplitude particles is approximately $\pm 3\%$ of $\Delta\nu_0$ throughout the run. As observed in the strong-strong simulations, the beams are expanding and contracting differently at different particle positions. The small-amplitude portion of the beam is constant oscillation amplitude, while the entire beam is increasing in oscillation amplitude. The odd moments, $< x >$ and $< (x- < x >)^3 >$, are both increasing in oscillation amplitude with rotation number. This increase in the odd moments is also observed in the strong-strong simulations.

8.1.3 Stability in the Tune Versus Tune Shift Space

Scans in parameters tune and tune shift, ν_0 and $\Delta\nu_0$, show regions of stability and instability against the beam blowup. These regions correspond closely to the regions predicted by the linear theory of Chao and Ruth.[18] For small values of the tune shift $\Delta\nu_0$, the beams are unstable just above a resonance. For beams with values of ν_0 just below a resonance, the beams are stable. Strong resonant beam blowup is observed just above $\nu_0 = 1/2$ and $\nu_0 = 1/4$ for values of $\Delta\nu_0 = 2.1 \times 10^{-3}$. Just below these tune values

the beams are stable, as expected. However, each of the beams shows dominant modes distorting the beams in $(x/\sigma_x, p_x/\sigma_p)$ space. For $\nu_0 = 1/2 - \Delta\nu_0$ mode 2 dominates, and for $\nu_0 = 1/4 - \Delta\nu_0$ mode 4 dominates. It is also found that the rate of beam blowup above the resonance drops with the order of the resonance. With $\nu_0 = 1/2 + \Delta\nu_0$ the beams blow up very quickly within a few hundred rotations. The beams blow up more slowly for $\nu_0 = 1/4 + \Delta\nu_0$. The slowest beam blowup is observed for $\nu = \nu_0 + \Delta\nu_0$, where in the case of two beams $\nu_0 = 2/6$ and $\Delta\nu_0 = 4 \times 10^{-3}$. In this case mode 6 dominates the distribution.

8.1.4 Particle Diffusion

In studying particle diffusion away from resonances, it is found that the tracking code shows no diffusion of particles from the beam-beam interaction over 10^5 rotations. The strong-strong codes are too noisy to study the process of diffusion of beam particles due to the beam-beam interaction. With variable charge initialization all particles show diffusive behavior after 10,240 rotations. The diffusion differs substantially from the tracking code. The diffusion coefficient D_x is uniform across the beam radius and is nearly an order of magnitude higher. With uniform charge initialization where the fluctuation noise is lower, only particles with large r/σ, where $r/\sigma = \sqrt{(x/\sigma_x)^2 + (p_x/\sigma_p)^2}$, are diffusive after 10,240 rotations. Results from noisy tracking codes modelling the finite particle fluctuation noise indicate that some of the diffusion can be attributed to this noise. This noise can be somewhat offset by using quieter particle initialization schemes such as the uniform charge scheme. However, there are still significant differences from the tracking code. Although the strong-strong code should show differences from the tracking code because of the self-consistent solution of the fields, it is difficult to determine whether the differences observed are due to particle fluctuation noise alone. However, it is apparent that the enhanced diffusion observed in the tails of the distribution for the strong-strong code is due to the self-consistent treatment of the beam dynamics.

The δf code with the lowest fluctuation level shows no particle diffusion up to 10,240 rotations, agreeing with the tracking code. The noise level of the δf code is less than the strong-strong code with either the variable or uniform charge distribution. However, particle diffusion is observed after 40,960 rotations for particles with large values of $r/\sigma > 2$. It appears that the particles in the tail of the distribution are most sensitive to either noise or collective motion in the beams. Variation of the δf particle number indicates that this diffusion in the tails is not due to particle noise. All particles are diffusive after 10^5 rotations. The magnitude of the diffusion is found to increase exponentially with the action J, where $J = (x/\sigma_x)^2 + (p_x/\sigma_p)^2$. This exponential dependence is found to be independent

of the number of particles used in the δf simulations. It appears, therefore, that collective beam effects are responsible.

Stochastic regions in phase space are found using the δf code by running the code forward and backward in time. They are found for particles with r/σ small and r/σ large. Between the two regions there is a thin ring where the particles may not be chaotic. Due to limited resolution the ring may consist of islands separated by stochastic regions.

8.1.5 Beam Offset Effects

In examining the effects of beam offset on diffusion, good agreement is found between analytic theory[22] and the tracking code. This is expected, since the tracking code is based on the "weak-strong" assumption, as is the theory. Results from the δf simulations show general agreement with the range of values for the diffusion. The δf code is started with 0 offset and is allowed to evolve self-consistently for $M = 10^5$ turns. The values of the diffusion in action are within the range of the analytic prediction. However, the δf results show an exponential dependence on the action J for large values of J, whereas the theory shows the diffusion leveling off. The approximate value for the diffusion from the change in luminosity is lower than the diffusion for most of the sample particles in the δf code. Tracking code results with $< x >$ input from the δf also do not show the same functional dependence on J as the δf code. The values for the diffusion, however, are within the same range. The exponential dependence on the action J is still under investigation. Analysis of the variation of the beam offset with increasing r/σ or equivalently $\sqrt{J}$ shows that the offset $< x >$ increases. It is apparent that because of the non-rigid character of the beam, particles at large J have much larger offsets than particles at small J. This variation of the offset with J explains the variation of the diffusion coefficients with J. The behavior is most likely due to the self-consistent effects included in the δf code, which are still under investigation. The leveling off in the diffusion is observed in the δf simulation when the beam strength $\Delta\nu_0$ is increased. The increase in $\Delta\nu_0$ leads to the increased beam offset $< x >$. It appears that when this beam offset is large enough, the resulting diffusion is dominated by beam offset diffusion.[22] This leveling-off in the diffusion is also seen for the strong-strong code. It appears as if the fluctuation level of the simulation determines whether the diffusion due to the presence of $< x >$ offset suggested by Stupakov[22] dominates the process of particle diffusion. This behavior in the diffusion is similar to the breakup of KAM tori.[57] For low fluctuation levels where the tune shift is small and the noise level is low, the phase space may contain many stable regions surrounded by regions of stochasticity. As the fluctuation level is increased, the stable regions disappear and the whole phase space may become stochastic. When this

occurs, the diffusion of particles is nearly uniform across the phase space, as observed in the simulations with high $\Delta\nu_0$ and high noise levels.

8.2 Future Improvements

In this section we discuss possible future improvements that can be made to the codes and future areas of study.

One obvious improvement to the code is extension to $x - y$ and $x - y - z$ dimensions. This extension is straightforward.

Improvements can be made to the simple storage ring model we employed. Some of the effects that can be included in the lattice traversal are:[29]

- betatron damping
- synchrotron motion
- non-zero chromaticity
- longitudinal displacement
- β^* variation along the length of the interaction point
- energy loss and phase change between interaction points
- quantum excitation.

As shown earlier, the perturbation equation for the δf advance was linear in δf (Eq. (6.108)). The term that is neglected is Eq. (6.109):

$$\delta F(x,s)\frac{\partial \delta f}{\partial x'}, \tag{8.1}$$

which was assumed to be small. This term, however, can be incorporated in the δf advance by placing it in the stationary Eq. (6.100):

$$\frac{\partial f_0}{\partial s} + x'\frac{\partial f_0}{\partial x} - \big(K(s) - F_0(s)\big)x\frac{\partial f_0}{\partial x'} = 0 \tag{8.2}$$

in the following manner:

$$\frac{\partial f_0}{\partial s} + x'\frac{\partial f_0}{\partial x} - \big(K(s) - F_0(s)\big)x\frac{\partial f_0}{\partial x'} =< \delta F(x,s)\frac{\partial \delta f}{\partial x'} >, \tag{8.3}$$

where $<>$ refers to time average. The incorporation of this term in the stationary Eq. (6.100) forces the numerical advance now of $f_0(x,x',s)$. However, $f_0(x,x',s)$ is slowly varying as long as it is away from resonances, so that the equation would need to be advanced only every few thousand rotations. The term in Eq. (8.1) is similar to the quasi-linear term used in plasma physics.[58]

Another improvement that can be made includes a higher-order method of integration of the particle positions. Higher-order integration may be accomplished using the method of symplectic integration algorithms[59] or Lie algebraic techniques.[60]

Also a possibility exists of applying the technique of differential algebra[61] to the δf algorithm. In this technique the δf method could be treated as a mapping function that could be applied to any points in phase space.

Another approach to the δf method would involve using the Vlasov approach (Eulerian method). The main problem with the Vlasov technique has been that the distribution functions go negative due to truncation errors. However, in the δf technique the main part of the distribution is already determined, and the perturbation can go negative without causing problems.

One of the topics of future study for the beam-beam interaction would be the determination of the mechanism for the exponential dependence in action J observed in the diffusion of the particles. A theory which includes self-consistent treatment of the interaction would be a next step. Other areas of investigation include investigation of betatron resonance, applications to other machines such as HERA or LHC, and the effects of collision angle on beam dynamics.

ACKNOWLEDGEMENTS

I would like thank my professor Toshi Tajima for the many years of guidance and collaboration which have led me to this point. I would also like to thank all my committee members—Wendell Horton, Rich Steinolfson, Barry Newberger, Chin Lin, and Lothar Koschmieder—for their guidance and encouragement. I especially thank Chin for the suggestion of reentering graduate school and seeking this elusive doctorate. I would also like the thank Alex Chao for the in-depth discussions on accelerator physics and the beam-beam interaction.

I am thankful to the Superconducting Super Collider Laboratory (SSCL) for partial support of this work, along with the Texas National Research Laboratory Commission (TNRLC). Also I acknowledge the support of this work by the U.S. Department of Energy and the National Science Foundation.

I thank all those people at Southwest Research Institute for continually goading me to carry on with my studies. Among the many are Kit Wong, Chris Gurgiolo, Jill Marshall, Joe Barfield, Shiro Konno, Doug Menietti, Walter Huebner, and Dan Boice. Without their persistent nudges I never would have finished. There are so many others I have not mentioned.

I would like to thank all the gang at First Presbyterian Church in San Antonio for putting up with me for all these years. I know it seems as if my promises of "graduation in a few months" went on like a repeating phonograph record.

I would also like to thank all my fellow and past graduate student comrades for their lively discussions and empathy. Among the many are R. Acevedo, D. Curran, D. Fisher, H. Ling, R. Kinney, S. Oliviera, M. Prahovic, X.N. Su, S. Tanquary, and H. Xiao. I know I've forgotten at least a few others. I would like to give an especially warm thanks to Sam Cable who had the gall to call me a "stupid pinhead" in his acknowledgements.[62] All I can say is it takes one to know one.

I would like to thank my family for their love and support through the long years. They have always been there for me, through good times and bad. Finally, I would like to thank God. Without him none of this would have been possible.

REFERENCES

1. D. A. Edwards and M. J. Syphers, "An Introduction to the Physics of Particle Accelerators," in *Physics of Particle Accelerators* (Fermilab Summer School 1987), M. Month and M. Dienes, eds., *AIP Conference Proceedings 184*, AIP, New York, 1989.
2. T. Bountis and S. Tompaidis, "Strong and weak instabilities in a 4-D mapping model of accelerator dynamics," Institute for Fusion Studies, Report no. 434, 1990.
3. B. V. Chirikov, J. Ford, and F. Vivaldi, in "Nonlinear Dynamics and the Beam-Beam Interaction", *A. I. P. Conf. Proc.* Vol. **57**, M. Month and J. C. Herrera, eds., p. 323, A. I. P., New York (1979).
4. SSC Central Design Group, Conceptual Design of the Superconducting Super Collider, ed. J. D. Jackson, March 1986, Report No. SSC-SR-2020.
5. E. D. Courant and H. S. Synder, "Theory of the Alternating-Gradient Synchrotron," *Annals of Physics*, **3**, p. 1–48, 1958.
6. S. G. Peggs and R. M. Talman, "Nonlinear problems in accelerator physics," *Ann. Rev. Nucl. Part. Sci.*, **36**, p. 287–325, 1986.
7. S. Kheifets, "Experimental observations and theoretical models for beam-beam phenomena," in *Long-Time Prediction in Dynamics*, C. W. Horton, L. E. Reichl, and V. G. Szebehely, eds., John Wiley and Sons, New York, p. 397, 1983.
8. A. W. Chao, "Coherent Beam-Beam Effects," SSCL-346, 1991.
9. A. G. Ruggiero, "Comparison between Theoretical Predictions and Tracking," *Particle Accelerators*, **19**, 157–179, 1986.
10. F. Amman and D. Ritson, "Space-Charge Effects in Electron-Electron and Positron-Electron Colliding or Crossing Beam Rings," *Intern. Conf. on High Energy Accel.*, Brookhaven, 471 (1961).
11. K. Hirata, "Coherent Betatron Oscillation Modes Due to Beam-beam Interaction," *Nucl. Instr. Meth. Phys. Res.* **A269**, 7 (1989).
12. I. M. Kapchinskiy, *Theory of Resonance Linear Accelerators*, Harwood Academic Publishers, Chur, 1970.
13. A. W. Chao and E. Keil, "Coherent Beam-Beam Effect," CERN/ISR-TH/79-31.
14. E. Keil, "Theoretical Aspects of the Beam-beam Interaction," *Proc. 11th Int. Conf. High Energy Accel.*, CERN, 759 (1980).
15. A. Piwinski, "Coherent Beam Break-Up Due to Space Charge," *Proc. 8th Int. Conf. High Energy Accel.*, CERN, 357 (1971).

16. R. Talman, "Multiparticle Phenomena and Landau Damping," *AIP Proc. 153*, Accelerator Summer School, SLAC and Fermilab, 789 (1987).
17. A. Piwinski, "Observation of Beam-beam Effects in PETRA", *IEEE Trans. Nucl. Sci.*, **NS-26**, 4268 (1979).
18. A. W. Chao and R. D. Ruth, "Coherent Beam-Beam Instability in Colliding-Beam Storage Rings," *Particle Accelerators* **16**, 1985, p. 201.
19. N. N. Chau and D. Potaux, "Stabilite des Oscillations Transverses dans un Anneau a Charge D'Espace Compensee, I. Methode de Calcul," Orsay Tech. Report 5-74 (1974).
20. N. N. Chau and D. Potaux, "Stabilite des Oscillations Transverses dans un Anneau a Charge D'Espace Compensee, II. Application au Choix d'un Point de Fonctionnement," Orsay Tech. Report 2-75 (1975).
21. Ya. S. Derbenev, *Proc. III All Union Part. Accel. Conf.*, Moscow, 382 (1973).
22. G. Stupakov, "Luminosity Dilution Due to Random Offset Beam-Beam Interaction," SSCL-560, 1991.
23. H. S. Uhm and C. S. Liu, "Filamentation instability of electron and positron colliding beam in storage ring," *Phys. Rev. Lett.*, **43**, 914, 1979.
24. R. Lee and M. Lampe, "Electromagnetic Instabilities, Filamentation, and Focusing of Relativistic Electron Beams," *Phys. Rev. Lett.*, **31**, pp. 1390–1393, 1973.
25. T. Tajima, "Stability theory of relativistic electron beam-plasma system with finite geometries," *Phys. Fluids*, **22**(6), p. 1157–1170, 1979.
26. R. H. Siemann, "Simulations of electron-positron storage rings," CESR note **CBN 89-4** (1989).
27. D. Neuffer, A. Riddiford, and A. Ruggiero, "A theoretical model and computer simulations to describe diffusion enhancement by the beam-beam interaction," *IEEE Trans. on Nuclear Sci.*, **NS-30**, 2430, 1983.
28. G. Jackson and R. H. Siemann, *Nucl. Inst. and Methods*, **286**, 17, 1990.
29. S. Myers, "Simulation of the beam-beam effect for e^+e^- storage rings," *Nucl. Inst. and Methods*, **211**, 263, 1983.
30. D. R. Douglas, "Tracking Codes in Accelerators: Types and Limitations," *Particle Accelerators*, **19**, pp. 119–123, 1986.
31. M. Bassetti and G. Erskine, CERN-ISR-TH/80-06 (CERN, 1980).
32. A. Piwinski, *IEEE Trans. Nucl. Sci.*, **NS-30**, 2378 (1983).
33. A. Hutton, PIP-NOTE-375, Stanford Linear Accelerator Center, 1982.
34. S. V. Milton and R. M. Littauer, CLNS 89/899 (Cornell, 1989).

35. S. Krishnagopal and R. Siemann, "Coherent Beam-beam Interactions in Electron-Positron Colliders," *Phys. Rev. Lett.*, **67**, 2461, 1991.

36. C. K. Birdsall and A. B. Langdon, *Plasma Physics via Computer Simulation*, McGraw-Hill, 1985.

37. T. Tajima, *Computational Plasma Physics*, Addison-Wesley, Redwood City, 1989.

38. T. P. Armstrong, R. C. Harding, G. Knorr, and D. Montgomery, "Solution of Vlasov's Equation by Transform Methods" in *Methods in Computational Physics*, Volume **9**, B. Alder, ed. (Academic Press, 1970), p. 29.

39. J. A. Byers and J. Killeen, "Collisionless Plasma Models" in *Methods in Computational Physics*, Volume **9**, B. Alder, ed. (Academic Press, 1970), p. 259.

40. P. M. Campbell and S. A. von Laven, "Vlasov-Maxwell Algorithm for Electromagnetic Plasma Simulation on Distributed Architectures," submitted to *Fourteenth International Conference on the Numerical Simulation of Plasmas*, September 3–6, 1991.

41. P. M. Campbell, private communication.

42. J. C. Herrera, M. Month, and R. F. Peirels, "Simple computer model for the nonlinear beam-beam interaction in Isabelle," in AIP Conference Proceedings No. 57, *Nonlinear Dynamics and the Beam-Beam Interaction*, M. Month and J. C. Herrera, eds., 1979, New York, p. 203.

43. J. D. Jackson, *Classical Electrodynamics*, John Wiley and Sons, Inc., 1975.

44. H. Okuda and C. Z. Cheng, *Comp. Phys. Comm.*, **14**, 169 (1978).

45. V. K. Decyk and J. M. Dawson, "Computer Model for Bounded Plasma," *J. Comput. Phys.* **30**, 407 (1979).

46. G. DiPeso, E. C. Morse, and R. W. Ziolkowski, "δf and Particle Simulations of Parametric Instabilities," *J. Comput. Phys.* **96**, 325 (1991).

47. M. Kotschenreuther, *Bull. Am. Phys. Soc.*, **33**, 2109 (1988).

48. D. Fisher, private communication.

49. T. Tajima and F. W. Perkins, *Proc. 1983 Sherwood Theory Meeting*, (University of Maryland, Arlington, VA, 1983) 2P9.

50. Y. L. Klimontovich, *The Statistical Theory of Non-Equilibrium Processes in a Plasma*, MIT Press, Cambridge, MA (1967).

51. B. Richter, *Proc. Int. Symp. Electron and Positron Storage Rings*, Saclay, 1966, p. I-1-1.

52. M. Sands, "The Physics of Storage Rings: An Introduction," SLAC-121 UC-28 (ACC), 1970.

53. M. B. Priestly, *Spectral Analysis and Time Series*, Vol. 1 (Academic Press, London, 1981).

54. T. Kamimura, T. Wagner, and J. M. Dawson, *Phys. Fluid*, **21**, 1151 (1978).

55. E. Parzen, *Technometrics*, **3**, 167 (1961).

56. R. Kubo, "Generalized Cumulant Expansion Method," *J. Phys. Soc. Japan* **17**, 1100 (1962).

57. M. Tabor, *Chaos and Integrability in Nonlinear Dynamics: an Introduction*, John Wiley and Sons, New York, 1989.

58. S. Ichimaru, *Basic Principles of Plasma Physics*, Benjamin/Cummings, Inc., Reading, MA (1973).

59. R. Ruth, "A canonical integration technique," *IEEE Trans. Nucl. Sci.*, **NS-30**, 2669–2671, 1983.

60. A. J. Dragt, F. Neri, G. Rangarajan, D. R. Douglas, L. M. Healy, and R. D. Ryne, "Lie algebraic treatment of linear and nonlinear beam dynamics," *Ann. Rev. Nucl. Part. Sci.*, **38**, pp. 455–496, 1988.

61. M. Berz, "Differential algebraic description of beam dynamics to very high orders," *Part. Accel.*, **24**, 109, 1989.

62. S. Cable, Ph. D. dissertation, University of Texas at Austin, 1992.